$^{22}\mathrm{Ne}(p,\gamma)^{23}\mathrm{Na}$, $^{23}\mathrm{Na}(p,\gamma)^{24}\mathrm{Mg}$, and Globular Cluster Abundance Anomalies

by

Stephen E. Hale Jr.

A dissertation submitted to the faculty of the University of North Carolina at Chapel Hill in partial fulfillment of the requirements for the degree of Doctor of Philosophy in the Department of Physics & Astronomy.

Chapel Hill

1999

Approved:

A. E. Champagne, Advisor

C. Iliadis, Reader

B. W. Carney, Reader

ABSTRACT

STEPHEN E. HALE JR.: ^{22}Ne$(p,\gamma)^{23}$Na, ^{23}Na$(p,\gamma)^{24}$Mg, and Globular Cluster Abundance Anomalies

(Under the Direction of A. E. Champagne)

Anticorrelations between sodium and oxygen have been observed in red giant stars in globular clusters, contrary to expectations from the standard theory of stellar evolution. It has been proposed that the ^{23}Na is being produced through the NeNa cycle operating in layers above the main hydrogen-burning shell. The (p,γ) reactions that produce and destroy sodium have large uncertainties because of the possible influence of several resonances. We have carried out measurements of the $(^3\mathrm{He},d)$ proton-stripping reaction on ^{22}Ne and ^{23}Na in order to study these resonances. The upper limits on the resonance strengths of two possible resonances at $\mathrm{E_{cm}} = 68$ and 100 keV, that account for most of the uncertainty in ^{22}Ne$(p,\gamma)^{23}$Na, have been reduced by factors of 10 and 4, respectively. The reaction rate of ^{23}Na$(p,\gamma)^{24}$Mg has been increased dramatically with the observation of the resonance at $\mathrm{E_{cm}} = 136$ keV with an increased strength from 10 to 6300 times stronger than the previously used value. The effect of these changes is to establish the nuclear reactions that can produce sodium in the red giant hydrogen-burning shell. The production of sodium is seen to coincide with the destruction of oxygen, through the NeNa and the CNO cycle respectively.

ACKNOWLEDGMENTS

I would like to thank my thesis advisor Art Champagne for his guidance and assistance in all manners experimental and theoretical. His perseverance in the face of difficulty made the work fruitful and enjoyable. Christian Iliadis has been an endless source of advice, and an excellent scientist to work with.

A very special thanks to Denise Powell who suffered with me through detector development and seemingly endless problem-causing runs. For sticking through the experiments after days of ripping the detector apart and putting it back together. For listening.

I am very grateful for all of the people who have supported my endeavors at the lab, from working on the experiment to discussing the results of the same. Peter Bertone, Jeff Blackmon, Carl Brune, Bill Geist, Vera Hansper, Becky Surman, and Kevin Veal have all been wonderful people to work with.

Paul Carter, Richard O'Quinn, John Dunham, Sidney Edwards, and Pat Mulkey have all kept things working with the endless details of TUNL. Robert Timberlake and the whole shop crew both machined the detector from the original design, and then suffered the numerous changes that experience dictated.

Thanks to my parents, for never letting me forget the light at the end of the tunnel.

An enormous debt of gratitude to Carrie Rowland. It cannot be quantified.

Stephen E. Hale Jr.

March 1999

To Carrie

many thanks indeed

CONTENTS

LIST OF FIGURES

LIST OF TABLES

Chapter 1

Introduction

Globular clusters contain 10^5 to 10^6 stars, gravitationally bound into a region of 10-30 parsecs in diameter. They form spherical shapes known for both their beauty and their usefulness to astronomy and astrophysics. The oldest clusters formed early in the history of the universe and thus contain some of the oldest stars known.

The globular cluster system that surrounds the Milky Way galaxy provides information about the formation mechanism and the size and structure of the galaxy. There are an estimated 180 globular clusters in and around our galaxy, some 150 of them visible while the rest are obscured by the galactic bulge [Ash98].

Individual globular clusters provide testing grounds for models of stellar evolution and the study of their properties has contributed to the development of our current understanding of the changes stars undergo over time. The various parameters of stars, including age, mass, color, temperature, and chemical composition, are all important considerations in the application of stellar models to the properties of globular clusters. It is important to understand how these different characteristics are determined by comparison with observations of globular cluster stars.

1.1 The Study of Globular Clusters

The main reason that globular clusters are useful in testing theories of stellar evolution is that the stars in a particular cluster are considered to be coeval and monometallic. While the cluster metallicities around the Milky Way range in [Fe/H][1] from solar (≈ 0.0) to about -2.5, within a given cluster the spread from star to star is ≤ 0.1 dex [Sun93, Ste93]. One cluster, ω Cen, stands apart from the rest in this aspect in that it shows a spread in [Fe/H] of 0.30 dex or more [Nor80, Muk92].

In order to apply the theories of stellar evolution to the stars in a given cluster, it is necessary to understand how mass, age, and chemical composition place a star on the color-magnitude diagram, such as the one shown in Figure 1.1 for M15 [Dur93]. The luminosity and temperature of a star depend on all of these characteristics.

The stars spend the majority of their lives on the main sequence (MS), fusing H into He in their cores. The fact that the MS of globular clusters is typically narrow indicates a small spread in chemical composition from star to star. If this were not the case, the spread in [Fe/H] would lead to a variation in opacity. This is because the large number of electrons in the heavier elements influence the propagation of light through the stars' envelopes. This would in turn cause variations in magnitude for a given color.

As time passes, the mass of the core increases as hydrogen is converted into helium. The central temperature of the star then increases under gravitational contraction and the CN burning becomes more important as a source of energy and also as an instigator in changing chemical composition [Cas80]. The effect of the CN cycle is to convert C into N, since the $^{14}\mathrm{N}(p,\gamma)^{15}\mathrm{O}$ reaction is the slowest one involved. Once the star has exhausted the innermost 10-20% of

[1]Here the standard spectroscopic notation is used: $[\mathrm{X/Fe}] = \log(\mathrm{X/Fe})_{\mathrm{star}} - \log(\mathrm{X/Fe})_{\odot}$.

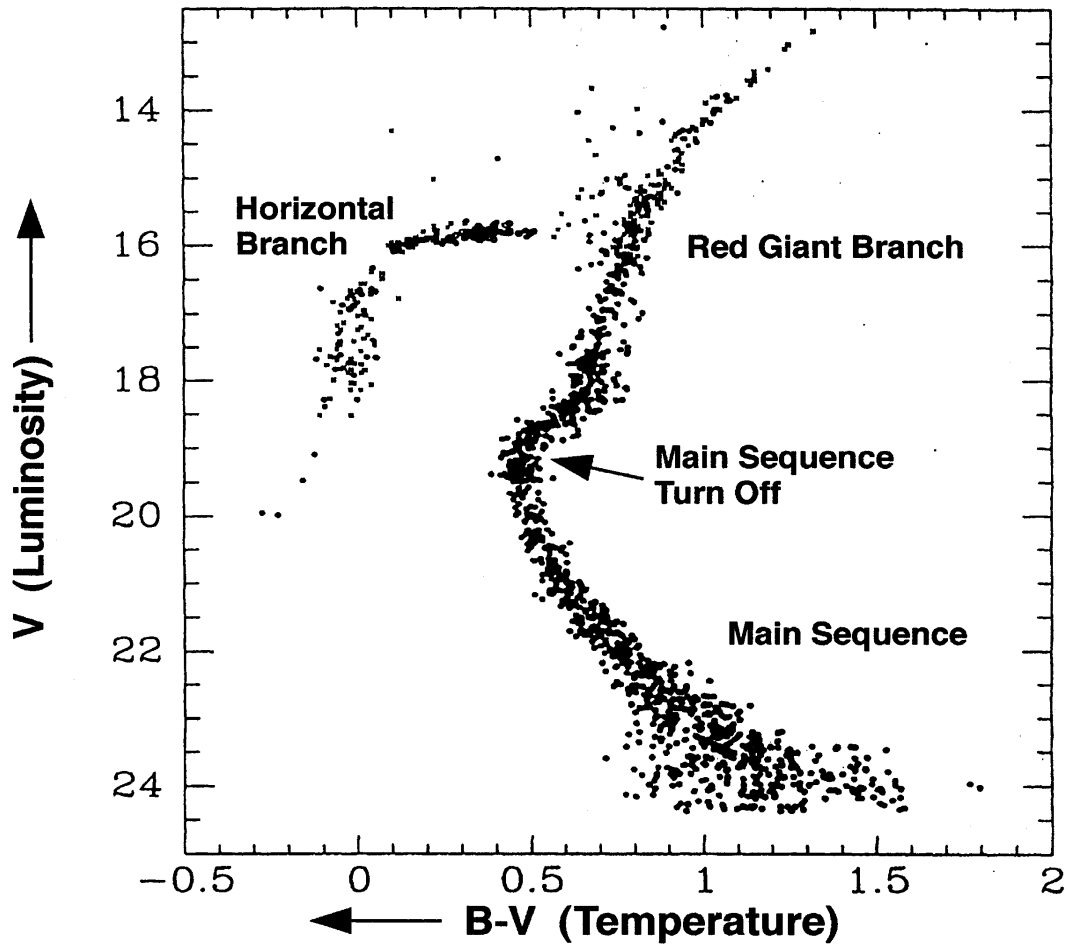

Figure 1.1: Color-magnitude diagram of M15 [Dur93].

the hydrogen in the core, it evolves off the MS and begins to ascend the Red Giant Branch (RGB), burning hydrogen in a shell surrounding the inert helium core [Cla83]. In response, the envelope of the star swells to giant proportions and simultaneously develops deep convection. The star undergoes the first dredge-up at this stage, which produces minor variations in the surface abundance of C and N. The base of the convective envelope reaches the mass within which ^{12}C has been processed into ^{14}N in the late main sequence phase and produces ^{14}N enhancements and ^{12}C depletions on the surface. This changing composition lasts only until the newly formed H-burning shell, moving outward in mass, encounters the base of the inward moving convective envelope and drives the base back out

again [Ibe80]. Thus, convection fails to penetrate the region of CN-burning of hydrogen while on the RGB. Consequently one would expect little change in the surface abundances from the base of the Red Giant Branch up to the tip, where the helium core ignites.

A point to note here is that the sharp turnoff of the MS indicates a small age spread from star to star, and hence supports the assumption of the coeval nature of the globular cluster. This is because for a large age spread, stars of widely different masses, and thus temperature and color, would be leaving the MS at the same time. For example, Stetson has found that the main sequence turn off in M92 limits the star to star age spread to about 0.4 Gyr [Ste93].

The star ascends the RGB while the burning hydrogen shell continues to deposit its helium ash onto the core. As the star evolves, the H-shell moves out in mass until the He core becomes hot enough to ignite the triple-α process (the helium flash) thus moving the star onto the Horizontal Branch.

1.2 Abundance Anomalies in Globular Cluster Red Giants

In contrast to the *expectations* of constant surface abundances while on the RGB, *observations* of surface abundances within a given globular cluster can show large variations. The best known are those of C and N, seen in wide variations of the strengths of CH, CN, and NH molecular bands. There are also wide variations in the $^{12}C/^{13}C$ abundance ratio, reaching values far below that predicted by standard stellar evolution calculations [Swe79]. Observations of these variations show some correspondance with evolutionary stage along the RGB.

In addition, variations in O and Na have been observed in globular clusters. Kraft *et al.* have determined that a global anticorrelation exists between [Na/Fe] and [O/Fe] among bright giants in five globular clusters and a collection of field

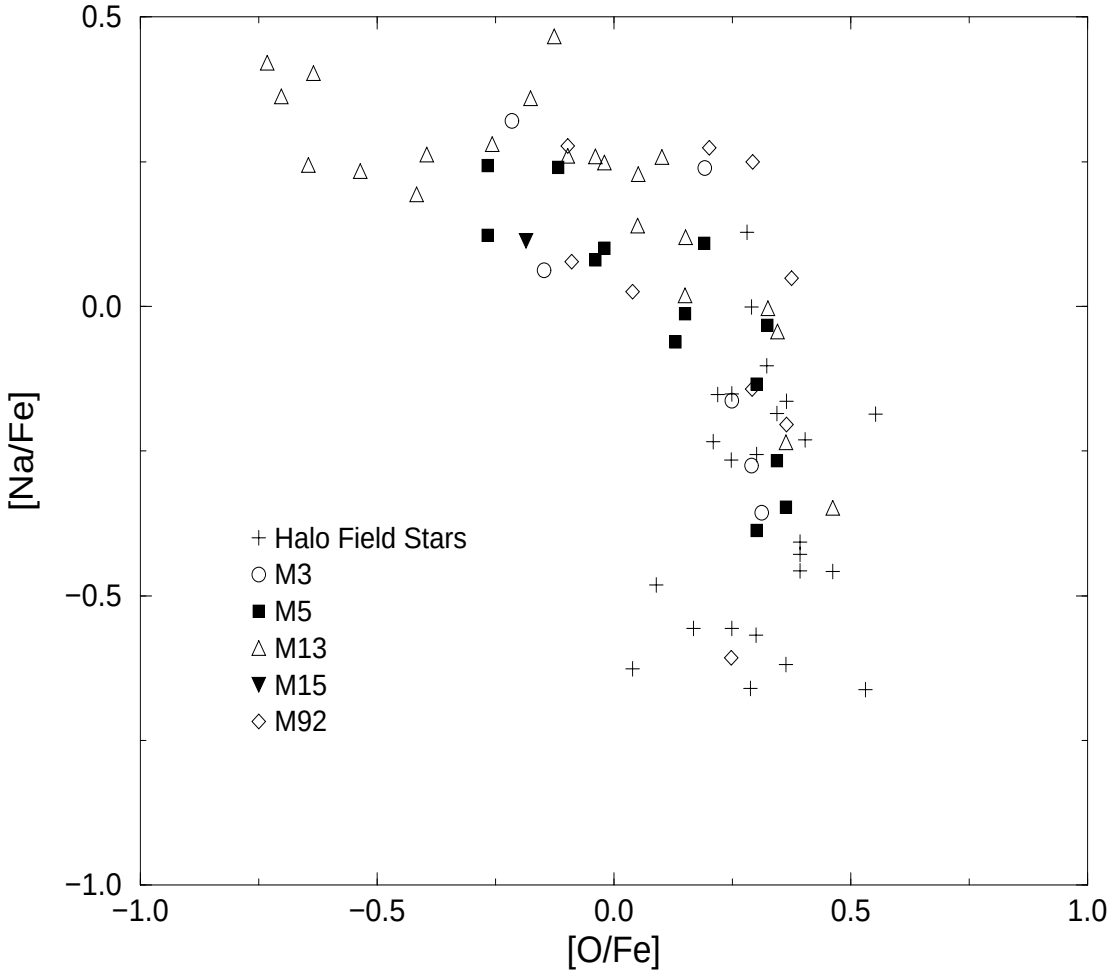

Figure 1.2: Global anti-correlation of [Na/Fe] vs. [O/Fe] [Kra93].

giant stars [Kra93]. These results are shown in Figure 1.2. The question that arises is whether these variations are due to primordial differences in the material that formed the cluster or from extra physics beyond the standard theory of stellar evolution. Enhanced mixing scenarios are one possibility of this new physics.

In order to mix any material from regions of nuclear processing to the surface, one must move beyond the classical stellar evolution which ignores, among other things, the effects of rotation [Ibe84]. Sweigart and Mengel [Swe79] suggested that internal rotation would cause meridional circulation to develop, which might bring CNO-processed material into the envelopes of red giant stars. They argued

that this sort of circulation must be a normal characteristic of a rotating star, caused by its deviation from spherical symmetry. This would prevent hydrostatic and thermal equilibrium from being fulfilled everywhere on an equipotential surface, thus forcing circulation currents to develop in order to compensate for a non-zero divergence of the radiation flux.

The mixing scenario would take material from the envelope into two regions above the H-shell. The outermost region is one in which the CN cycle processes material. Closer to the H-shell, the ON cycle can take place. This leads to three distinct points where, moving into the center of the star, one first reaches the radius where the carbon falls to half of its original value, then the radius where oxygen reaches half of its original value, and finally the center of the hydrogen shell where the H abundance has dropped to one-half of its original value. The temperatures quoted in Sweigart and Mengel at which these stages are reached are shown in Table 1.1 (in units of billions of degrees Kelvin, T_9). Figure 1.3 shows Sweigart & Mengel's abundance profile for a red giant model with a mass of 0.90 $M_\odot$, a helium abundance of 0.20, a metal (all elements heavier than helium) abundance of 0.0001, and a luminosity of log L = 2.31. This shows the shells of depleted carbon and oxygen above the hydrogen shell. For this low metallicity model, the mean molecular weight (μ) gradient is negligible across the carbon shell and small across the oxygen shell. (The hydrogen abundance is depleted by only 0.0004 from the envelope value.) The μ gradient, which tends to inhibit meridional circulation, thus does not prevent CN- and ON-processed material from being reached by the mixing.

Stochastic variations in the rotation rate from star to star would then lead to different mixing depths and hence different amounts of processed material being brought to the surface. One difficulty with the mixing scenario that should be pointed out is that CN variations have been found in main sequence stars in 47 Tuc and NGC 6752 [Ash98]. No mixing theory is able to produce these variations while the stars are still on the main sequence.

Burning Cycle	Temperature (T_9)
CN	0.022
ON	0.034
p-p	0.048

Table 1.1: Temperatures reached in the various burning shells of Sweigart & Mengel's model.

1.3 The NeNa Cycle in RGB Stars

Originally it was thought that ^{23}Na observed in low mass stars would be formed by neutron capture on ^{22}Ne followed by β-decay in a previous environment. The Na enriched material would then have been incorporated into the globular cluster stars as they formed. This primordial argument was necessary because the neutron producing reactions thought to be responsible, $^{13}C(\alpha, n)^{16}O$ and $^{22}Ne(\alpha, n)^{25}Mg$, should not be occurring in stars on the Main Sequence or the Red Giant Branch.

Denisenkov and Denisenkova [Den90] proposed that the sodium is actually produced in the proton-capture reaction on ^{22}Ne, part of the NeNa cycle that is shown in Figure 1.4, which would take place in the same region where O is depleted above the H-burning shell. The sodium thus produced would be transported to the surface by meridional circulation.

Langer *et al.* [Lan93], used the $^{16}O(p, \gamma)^{17}F$ and $^{22}Ne(p, \gamma)^{23}Na$ rates as tabulated by Caughlan & Fowler [Cau88] to determine the processing of nuclei in the region above the H-burning shell. For a metal-poor star, [Fe/H] ≈ -2.2, about 1.3 magnitudes below the Red Giant Branch tip, they found that ^{23}Na could be produced if ^{22}Ne exists in the oxygen shell, mixed there from the envelope along with the oxygen to be converted into nitrogen. Langer's nuclear reaction network mixed material to a constant temperature of $T_9 = 0.04$ and a constant density of $\rho = 44.7$ g cm^{-3}. When the hydrogen had dropped by 5% they found that the oxygen abundance had decreased by a factor of 40, nitrogen had increased

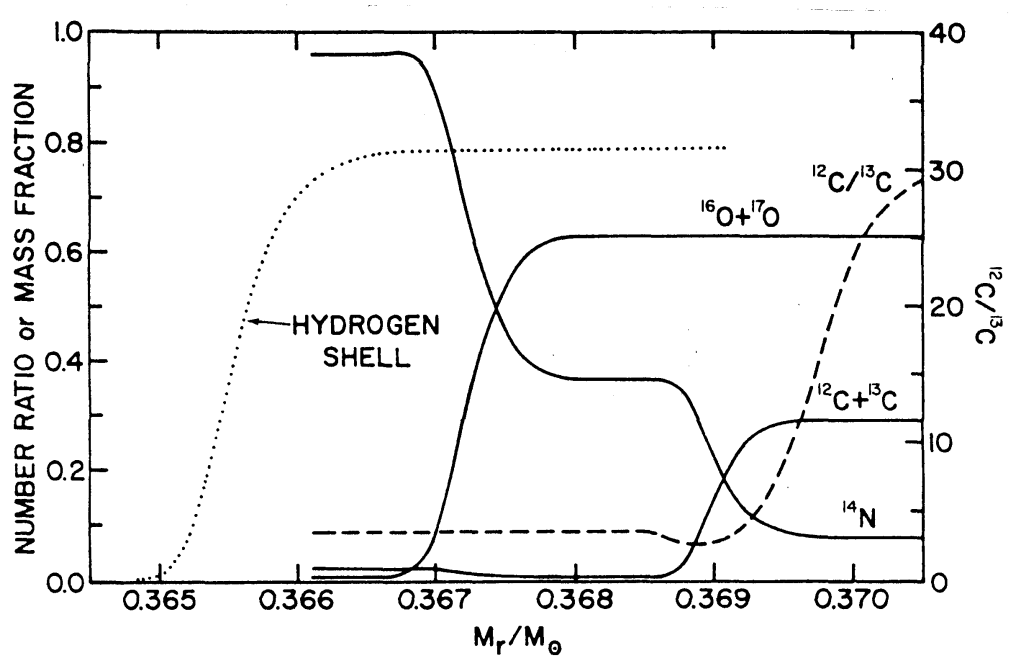

Figure 1.3: CNO element distribution above the H-shell of a red giant model. The three solid curves use the left vertical scale to plot the abundance by number as a fraction of the total number of CNO nuclei. The dotted curve shows the hydrogen abundance X. The dashed curve shows the ratio between ^{12}C and ^{13}C using the right vertical scale. [Swe79]

to more than 40 times its original value and the sodium abundance had risen by a factor of 25. This large increase in sodium required the NeNa cycle to process material from ^{20}Ne up to ^{23}Na.

In an attempt to more realistically study the influence of the reaction rates and model the stellar environment, Cavallo *et al.* [Cav98], combined a large nuclear reaction network with four stellar evolutionary sequences of different metallicities. This allowed them to take into account the changing T and ρ profiles around the H-shell as the stars change with age and [Fe/H].

For the higher metallicity sequences they modeled, the primary source of ^{23}Na is from the ^{22}Ne(p,γ) reaction. For the lower metallicities, where the temperatures are hotter above the hydrogen-burning shell, the ^{23}Na(p,γ) and ^{23}Na(p,α) reactions act to siphon away the nucleus of observational interest. Their isotope distribution as a function of the parameter ΔS is shown in Figure 1.5 for two of

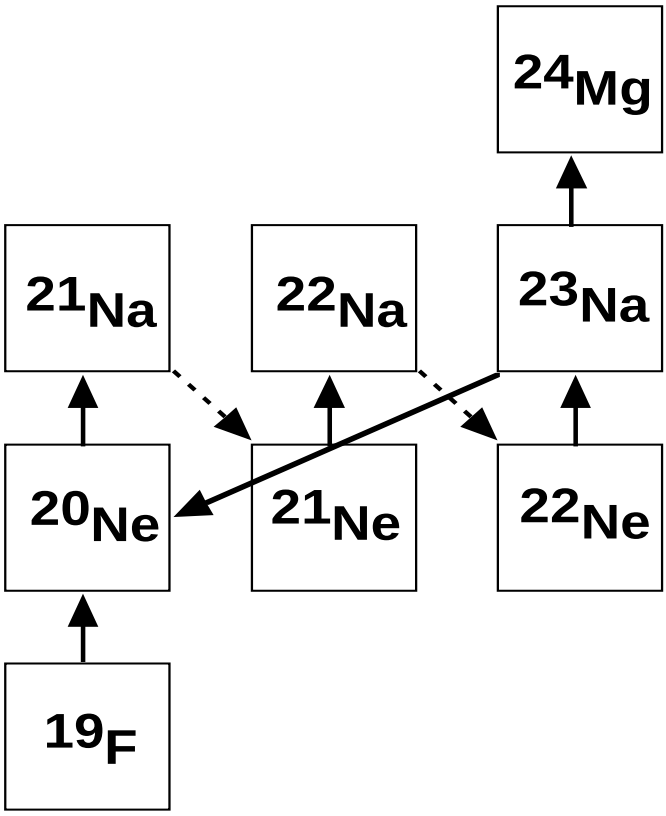

Figure 1.4: The NeNa cycle which transforms 4 protons into an α particle upon completion of the ^{23}Na$(p,\alpha)^{20}$Ne reaction. Beta-decays in the cycle are indicated by dashed arrows.

the metallicities in which these effects occur. The parameter ΔS is defined as the mass difference, ΔM_r, between any point and the center of the H-shell, divided by the H-shell thickness, ΔM_H. Thus $\Delta S = 0$ defines the middle of the H-shell where the H abundance has fallen by 50%. The arrow indicates the center of the O-shell, where the ^{16}O abundance is half of the envelope value.

The isotopic abundances are sensitive to the sequence metallicity and luminosity. However in both sequences shown, the sodium is produced from ^{22}Ne in a plateau above the hydrogen-burning layer. In the sequences, the oxygen shell (indicated by the arrow) is located in the region of sodium production at the start of mixing. Thus, large sodium enhancements should be accompanied by oxygen depletions, as observed.

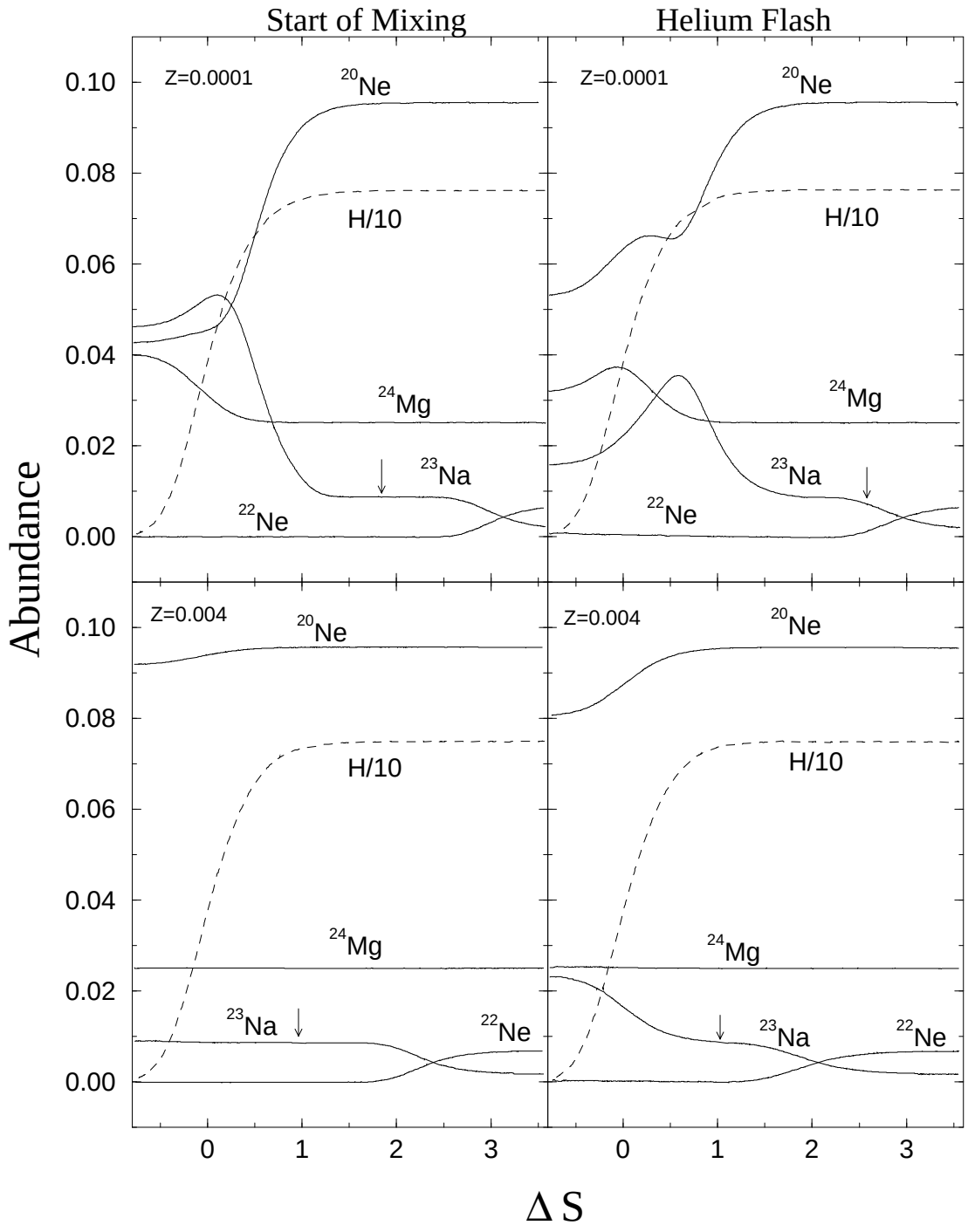

Figure 1.5: The NeNa cycle isotopes at the presumed start of mixing and at the tip of the RGB for two sequences modelled by Cavallo *et al.* The top portion shows the distribution for the Z=0.0001 sequence while the bottom portion shows the distribution for the Z=0.004 sequence. See text for discussion of the implications of current nuclear reaction rates on these results.

The depth in the star where nuclear reactions take place is determined by the reaction rate, which is energy (and thus temperature) dependent. The two reactions ^{22}Ne$(p,\gamma)^{23}$Na and ^{23}Na$(p,\gamma)^{24}$Mg are central to predictions of sodium production at both high and low metallicities, respectively. The latest compilation of reaction rates in the NeNa cycle by El Eid & Champagne [EEC95] (hereafter referred to as EEC95) showed that these reaction rates are quite uncertain because of the possible influence of several resonances. Cavallo's work showed that the ^{22}Ne$(p,\gamma)^{23}$Na uncertainty alone can cause the Na plateau to extend by a factor of 2 further above the O-depleted region, thus leading to large Na enhancements without affecting the O abundance.

The purpose of this work is to study the resonances of interest in both the ^{22}Ne$(p,\gamma)^{23}$Na and ^{23}Na$(p,\gamma)^{24}$Mg reactions in order to remove the current uncertainties in the respective reaction rates. This will lead to more definitive constraints on the mixing scenarios by allowing the accurate prediction of the extent of sodium production and destruction above the H-burning shell in red giant stars.

Chapter 2

Astrophysics Formalism and Direct Reaction Information

2.1 Resonance-Reaction Formalism

The development of the reaction rate formalism provided here follows the treatment given in *Cauldrons in the Cosmos* [Rol88]. The nuclear reactions that occur in stars take place in a gas of nuclei. The individual particles have velocities that vary over a wide range of values, characterized by a distribution $\phi(\mathrm{v})$, where $\phi(\mathrm{v})\mathrm{dv}$ is the probability that the velocity is between v and v + dv. The cross sections of the nuclear reactions are energy, and thus velocity, dependent. Therefore the cross section must be folded with the velocity distribution, resulting in

$$\langle \sigma \mathrm{v} \rangle = \int_0^\infty \phi(\mathrm{v}) \mathrm{v} \sigma(\mathrm{v}) d\mathrm{v}. \tag{2.1}$$

This quantity is called the reaction rate per particle pair, where v is the relative velocity between the two particles.

If the two nuclear species of interest, x and y, have number densities given by $\mathrm{N_x}$ and $\mathrm{N_y}$ respectively, then the number of reactions per second per unit volume is called the stellar reaction rate and is written as

$$\mathrm{r} = \mathrm{N_x}\,\mathrm{N_y}\ \langle \sigma \mathrm{v} \rangle\ (1 + \delta_{\mathrm{xy}})^{-1}. \tag{2.2}$$

The term $(1 + \delta_{xy})$ is included to take into account the possibility of identical particles in the entrance channel. The mean lifetime of nuclei in a stellar environment is usually more useful, which for nuclei x with respect to destruction by nuclei y, is given by

$$\tau_y(x) = \frac{1}{N_y \langle \sigma v \rangle}. \tag{2.3}$$

Since stellar model calculations usually deal with matter densities, ρ (g cm^{-3}), and mass fractions X_i or mole fractions Y_i of a general nuclear species i, the number densities are related to these values by

$$N_i = \rho N_A \frac{N_i}{A_i} = \rho N_A Y_i, \tag{2.4}$$

where A_i is the atomic mass of nucleus i in amu units. The lifetime of nucleus x against destruction by nucleus y is then

$$\tau_y(x) = \frac{1}{\rho Y_y} \frac{1}{N_A \langle \sigma v \rangle}. \tag{2.5}$$

The quantity $N_A \langle \sigma v \rangle$, which has units of cm$^3 \cdot$ mole$^{-1} \cdot$ s^{-1}, is what is normally tabulated as the reaction rate.

Stars on the Main Sequence and Red Giant Branch have material burning in a gas that is nondegenerate, non-relativistic and in thermal equilibrium. The velocities of the particles are therefore described by a Maxwell-Boltzmann distribution. In terms of the center of mass kinetic energy, E, of the interacting nuclei this is

$$\phi(E) \propto E \exp\left(-\frac{E}{kT}\right), \tag{2.6}$$

where T is the temperature of the environment and k is Boltzmann's constant.

The reaction rate per particle pair is given by

$$\langle \sigma v \rangle = \left(\frac{8}{\pi \mu}\right)^{1/2} \frac{1}{(kT)^{3/2}} \int_0^\infty \sigma(E)\, E \exp\left(-\frac{E}{kT}\right)\, dE \tag{2.7}$$

where $\mu = m_x m_y/(m_x + m_y)$ is the reduced mass. The cross section $\sigma(E)$ depends on the mechanism by which the reaction proceeds. One possible method is for the incident particle to be captured directly into a final bound state via

the electromagnetic interaction. This contribution to the cross section, called direct capture, has a smooth energy dependence governed primarily by barrier penetrability. Thus, it drops precipitously with decreasing energy.

In contrast, a resonant capture can take place when the energy of the entrance channel, given by the Q-value plus the projectile energy, $\mathrm{Q} + \mathrm{E_R}$, matches the energy of an excited state in the compound nucleus, $\mathrm{E_x}$,

$$\mathrm{E_R} = \mathrm{E_x} - \mathrm{Q}. \tag{2.8}$$

For narrow, isolated resonances, the cross section is given by the Breit-Wigner formula

$$\sigma_{\mathrm{BW}}(\mathrm{E}) = \pi \left(\frac{\lambda}{2\pi}\right)^2 \omega \, \frac{\Gamma_\mathrm{a}\Gamma_\mathrm{b}}{(\mathrm{E}-\mathrm{E_R})^2 + (\Gamma/2)^2}. \tag{2.9}$$

Here λ is the de Broglie wavelength of the entrance channel, Γ_a and Γ_b are the (energy dependent) partial widths for the formation and decay of the compound nucleus, respectively, and $\Gamma = \sum_i \Gamma_i$ is the total width. The statistical factor ω is given by the expression

$$\omega = \frac{2\mathrm{J}+1}{(2\mathrm{J_x}+1)(2\mathrm{J_y}+1)} \, (1 + \delta_{\mathrm{xy}}) \tag{2.10}$$

in which J is the spin of the compound nucleus state formed, and $\mathrm{J_x}$ and $\mathrm{J_y}$ are the spins of the target and projectile nucleus, respectively. A narrow resonance is defined as one in which the width Γ is much smaller than the resonance energy, $\Gamma \ll \mathrm{E_R}$.

For such a resonance, the Maxwell-Boltzmann distribution $\phi(\mathrm{E})$ changes very little across the width of the resonance, so its value at the resonance energy can be pulled outside of the integral in Equation 2.7 to yield

$$\langle \sigma \mathrm{v} \rangle = \left(\frac{8}{\pi\mu}\right)^{1/2} \frac{1}{(\mathrm{kT})^{3/2}} \, \mathrm{E_R} \exp\left(-\frac{\mathrm{E_R}}{\mathrm{kT}}\right) \int_0^\infty \sigma_{\mathrm{BW}}(\mathrm{E}) \, \mathrm{dE}. \tag{2.11}$$

Assuming that the de Broglie wavelength and the partial and total widths are roughly constant over an energy range $\Delta\mathrm{E} \approx \Gamma$, the integral above reduces to

the following expression

$$\begin{aligned}\int_0^\infty \sigma_{\rm BW}({\rm E})\,{\rm dE} &= \pi\left(\frac{\lambda_{\rm R}}{2\pi}\right)^2 \omega\,\Gamma_{\rm a}\,\Gamma_{\rm b}\int_0^\infty \frac{1}{({\rm E}-{\rm E_r})^2+(\Gamma/2)^2}\,{\rm dE} \\ &= \frac{1}{2}\,\lambda_{\rm R}^2\,\omega\,\frac{\Gamma_{\rm a}\Gamma_{\rm b}}{\Gamma}. \end{aligned} \tag{2.12}$$

The width ratio is generally written as

$$\gamma = \frac{\Gamma_{\rm a}\Gamma_{\rm b}}{\Gamma} \tag{2.13}$$

and the strength of the resonance is referred to as the combination

$$\omega\,\gamma = \omega\frac{\Gamma_{\rm a}\Gamma_{\rm b}}{\Gamma}. \tag{2.14}$$

Putting together equations 2.7, 2.12, and 2.14, the narrow resonance reaction rate per particle pair is given by

$$\langle\sigma{\rm v}\rangle = \left(\frac{2\pi}{\mu{\rm kT}}\right)^{3/2}\hbar^2(\omega\gamma)_{\rm r}\exp\left(-\frac{\rm E_r}{\rm kT}\right). \tag{2.15}$$

When several isolated, narrow resonances exist (as is the case in this work), their contribution is summed to give

$$\langle\sigma{\rm v}\rangle = \left(\frac{2\pi}{\mu{\rm kT}}\right)^{3/2}\hbar^2\sum_{\rm r}(\omega\gamma)_{\rm r}\exp\left(-\frac{\rm E_r}{\rm kT}\right). \tag{2.16}$$

To determine which resonances could be important for a given astrophysical environment, the most effective burning energies must be found for particles at a particular temperature. This is given by

$${\rm E_0} = 1.22\,({\rm Z_1^2\,Z_2^2\,\mu\,T_6^2})^{1/3}\,{\rm keV} \tag{2.17}$$

with a $1/e$ width of

$$\Delta = 0.749({\rm Z_1^2\,Z_2^2\,\mu\,T_6^5})^{1/6}\,{\rm keV}, \tag{2.18}$$

where $\rm Z_1$ and $\rm Z_2$ are the charges of the two nuclei, μ is the reduced mass, and $\rm T_6$ is the temperature in units of 10^6 K. For the temperature in the H-burning shell in RGB stars, the values of $\rm E_0$ are given in Table 2.1 for the two reactions

T_6	^{22}Ne + p E_0 (keV)	^{23}Na + p E_0 (keV)
20	41 ± 10	44 ± 10
30	54 ± 14	57 ± 14
40	65 ± 18	70 ± 18
50	76 ± 21	81 ± 22
60	86 ± 25	91 ± 25
70	95 ± 28	101 ± 29

Table 2.1: Effective burning energies for ^{22}Ne + p and ^{23}Na + p at red giant H-burning shell temperatures.

of interest. In comparison, the Coulomb barriers for the ^{22}Ne + p and ^{23}Na + p reactions are 3.3 and 3.6 MeV, respectively.

The γ-ray partial width Γ_γ is roughly on the order of 1 eV and is fairly constant (to within a factor of ≈ 100) over a large range of excitation energies in the compound nucleus formed. However, the magnitude of the proton partial width, $\Gamma_{\rm p}$, is very energy dependent, again because of Coulomb penetrability, and can decrease to very small values at low proton energies, $E_{\rm p} \leq 150$ keV. Thus at the low energies of interest for Red Giant H-shell burning,

$$\Gamma_{\rm p} \ll \Gamma_\gamma. \tag{2.19}$$

If these are the only two channels open then $\Gamma \approx \Gamma_\gamma$ and the strength of the resonance can be written as

$$\omega\gamma = \omega\frac{\Gamma_{\rm p}\Gamma_\gamma}{\Gamma} \approx \omega\Gamma_{\rm p}. \tag{2.20}$$

This holds for ^{22}Ne(p,γ), but for ^{23}Na + p the (p,α) channel is also open leading to the reaction ^{23}Na$(p,\alpha)^{20}$Ne. Thus, in the latter case, the total width is given by

$$\Gamma = \Gamma_{\rm p} + \Gamma_\gamma + \Gamma_\alpha \tag{2.21}$$

and the evaluation of $\omega\gamma$ becomes more complicated.

2.2 Indirect Determination of Γ_p

The resonance strength $\omega\gamma$ can be measured directly through (p,γ) reactions at the energy of the resonance. The cross section for these reactions at proton energies below ≈ 150 keV can become prohibitively small for target nuclei with large Z, so indirect methods must be employed. One possibility is to use the direct capture process at a higher proton beam energy into the lower-lying state one wishes to measure. Another method is to form the state via a proton-stripping reaction such as (d,n) or $(^3\mathrm{He},d)$, in which an incident particle drops a proton onto the target, making the same state as in a (p,γ) reaction. In this work, the $(^3\mathrm{He},d)$ reaction, shown schematically in Figure 2.1, is chosen to populate the states of interest because of the superior resolution that can be obtained for charged particles (as opposed to neutrons).

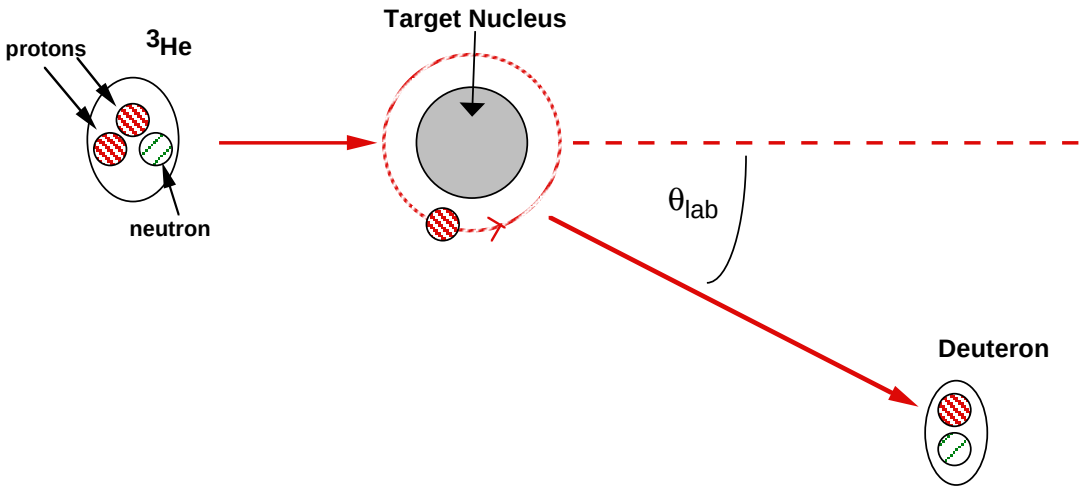

Figure 2.1: Schematic of the $(^3\mathrm{He},d)$ mechanism showing the formation of the final nucleus after the one-step proton-stripping reaction.

The true proton partial width can be written in terms of a theoretical single-particle proton partial width, Γ_{sp}, using the spectroscopic factor S and an isospin Clebsch-Gordan coefficient C [Sch63]

$$\Gamma_p = C^2 S\, \Gamma_{sp}. \tag{2.22}$$

Thus, the combination of C^2S can be viewed as measuring to what degree the real state resembles a fictitious state composed of the target nucleus and a proton in a shell-model single-particle orbital. By measuring the value of C^2S for the states of interest with a proton-stripping reaction and calculating the single-particle proton partial width, Γ_p can be estimated for states that cannot be measured directly in a (p, γ) reaction.

2.2.1 The Distorted Wave Born Approximation (DWBA)

To obtain information about the single-particle character of the states of interest in the final nucleus, the reaction that is used to populate those states must be a direct, single-step reaction. That is, it should not proceed via the interaction of the incident particle with the entire nucleus through a compound nucleus formation. The direct reaction will be sensitive to the overlap between the initial and final states, from which details about the reaction of astrophysical interest can be determined.

One important factor to consider in choosing an experimental method to use is the energy of the incident beam [End77]. The contribution to the cross section from compound nucleus formation is large at relatively low energies (below E $\approx$ 5 MeV). At high energies, above $\approx$ 50 MeV, there is considerable penetration of the incident particle into the nucleus. This increases the likelihood that the particle interacts with the majority of the nucleons in the target, via a compound nucleus formation. The beam of incident particles that was chosen for this study was ^{3}He at an energy of 20 MeV.

The general reaction A(a,b)B is referred to as a stripping reaction if a = b + x and B = A + x, so that x is the stripped particle. The assumption that the process of transferring the particle x from a to A is weak compared to elastic scattering leads to the distorted-wave Born approximation (DWBA). This subject has previously been discussed in great detail [Sat64, Gle75, Mac75, Gle83, Sat83] so only a general overview will be presented here.

The DWBA cross section is given in terms of the transition amplitude, T, from the entrance channel i to the exit channel f as

$$\frac{\mathrm{d}\sigma}{\mathrm{d}\Omega} = \frac{\mu_i \mu_f}{(2\pi\hbar^2)^2} \frac{\mathrm{k}_f}{\mathrm{k}_i} \frac{1}{(2\mathrm{J_A}+1)(2\mathrm{j_a}+1)} \sum_{\mathrm{M_A,m_a,M_B,m_b}} |\mathrm{T}|^2 \tag{2.23}$$

in which μ and k are the reduced mass and wave numbers for the appropriate channel, and $\mathrm{J_A}$ and $\mathrm{j_a}$ are the spins of the target and projectile, respectively. This formula holds true for unpolarized target nuclei and unpolarized projectiles. The sum is performed over all spin projections. Isospin coupling between the inital and the final isospin will be accounted for with the Clebsch-Gordan coefficient, C, in comparing the experimental cross section with the DWBA value.

The transition amplitude is

$$\mathrm{T} = \int \mathrm{d}\vec{\mathrm{r}}_\mathrm{a} \int \mathrm{d}\vec{\mathrm{r}}_\mathrm{b} \chi_\mathrm{b}^{(-)*}(\vec{\mathrm{k}}_\mathrm{b}, \vec{\mathrm{r}}_\mathrm{b}) \left\langle \mathrm{B, b} \left| \mathrm{V}_{eff} \right| \mathrm{A, a} \right\rangle \chi_\mathrm{a}^{(+)}(\vec{\mathrm{k}}_\mathrm{a}, \vec{\mathrm{r}}_\mathrm{a}). \tag{2.24}$$

The relative coordinates of a(b) with respect to A(B) are given by $\vec{\mathrm{r}}_\mathrm{a}(\vec{\mathrm{r}}_\mathrm{b})$. The χ_a and χ_b are the distorted waves of the entrance and exit channel. The operator V_{eff} acts to transform the entrance channel into the exit channel, and the matrix element has been evaluated to remove the dependence on all variables except for $\vec{\mathrm{r}}_\mathrm{a}$ and $\vec{\mathrm{r}}_\mathrm{b}$. This expression for T results in a six-dimensional integral after the matrix element is evaluated. Some assumptions are generally made to simplify the problem.

The potential V_{eff} can be expressed in two ways as

$$\mathrm{V}_{eff} = \begin{cases} \mathrm{V}_i - \mathrm{U}_i & \text{prior to reaction} \\ \mathrm{V}_f - \mathrm{U}_f & \text{post reaction} \end{cases} \tag{2.25}$$

where $\mathrm{V}_{i,f}$ is the interaction potential and $\mathrm{U}_{i,f}$ is an auxillary potential describing the elastic scattering. Using the post-reaction expression, the potential becomes

$$\mathrm{V}_{eff} = \mathrm{V_{bx}} + \mathrm{V_{bA}} - \mathrm{U}_f \tag{2.26}$$

in which $\mathrm{V_{bx}}$ describes the interaction between the transferred particle and the remainder of the projectile, $\mathrm{V_{bA}}$ describes the interaction between the exiting

particle and the remaining A nucleons, and U_f is the distorting potential which describes the elastic scattering in the exit channel of b + B = b + (A + x).

The cancellation approximation, $V_{bA} - U_f = 0$, is used and the only remaining interaction is $V_{eff} = V_{bx}$. Thus the matrix element can be written as

$$\langle B, b \left| V_{eff} \right| A, a \rangle = \langle B|A\rangle \langle b \left| V_{bx} \right| a \rangle . \tag{2.27}$$

The break-up of the projectile is further simplified by the zero-range approximation, which argues that the particle b is emitted at the same point that the particle x is absorbed. The resulting matrix element has been evaluated for the $(^3\mathrm{He}, d)$ stripping reaction by Bassel [Bas66]. The effects of a true finite-range interaction can be approximately incorporated into a zero-range calculation with a reaction-dependent correction factor.

The final part of the matrix element consists of the overlap integral

$$\langle B|A\rangle = \langle \Phi_B(A+1)|\Phi_A(A)\rangle . \tag{2.28}$$

The wave function of B is expanded in terms of wave functions of the target nucleus combined with a set of wave functions for the transferred particle $\psi_{nlj}(\vec{r}_x)$. This single-particle wave function is an optical-model wave function using a Woods-Saxon potential. The depth of the potential is generally varied to reproduce the binding energy of the state formed by A + x. Thus far, the assumption has been that the final states are pure single-particle (target-nucleus core plus a valence nucleon) states. An actual state will have a variety of configurations including some fraction of the allowed single-particle strength. To account for the possibility of this mixed parentage, a correction factor is introduced into the expansion of $\Phi_B(A+1)$ so that

$$\Phi_B(A+1) = \sum_{A'} \sum_{nlj} \beta_{nlj}(A', B)[\Phi_{A'}(A)\psi_{nlj}(\vec{r}_x)]_{J_B} \tag{2.29}$$

where A′ are the various states of the target nucleus and β_{nlj} is the parentage coefficient for the shell-model orbital with quantum numbers n, l, and j.

The spectroscopic factor is related to the square of the parentage coefficient

$$\mathrm{S}_{nlj}(\mathrm{A},\mathrm{B}) = \beta^2_{nlj}(\mathrm{A},\mathrm{B}) \tag{2.30}$$

which effectively measures the probability that the state B produced in the (a,b) reaction is formed by the ground state of A with the stripped particle x in the shell-model state with quantum numbers nlj.

2.2.2 Distorted Waves and the Optical Model Potential

In the expression for the transition amplitude, the $\chi_{\mathrm{a,b}}$ are distorted waves for the entrance and exit channel. They are found by assuming that the elastic scattering of A + a and B + b can be described as scattering off an optical model potential, rather than by solving the many-body problem of the nucleons in a(b) interacting with the nucleons in A(B). They are solutions of the time-independent Schrödinger equation

$$\left(-\frac{\hbar^2}{2\mu}\nabla^2 + \mathrm{U}(\vec{r}) - \mathrm{E}\right)\chi(\mathrm{k},\mathrm{r}) = 0 \tag{2.31}$$

in which U is the appropriate optical model potential, consisting of nuclear and Coulomb contributions.

The form chosen to represent the nuclear potential shape is a Woods-Saxon expression

$$f(r, r_x, a_x) = \frac{1}{1 + \exp[(r - r_x \mathrm{A}^{1/3})/a_x]} \tag{2.32}$$

which has a range of $\mathrm{R} = r_x \mathrm{A}^{1/3}$ and a surface diffuseness of a_x.

In addition to a real component of the potential, other contributions are added to account for physical observations. Because particles are lost from the elastic scattering channel to reaction channels, an imaginary potential component is introduced. This is in analogy to the scattering and absorption of light in a semi-transparent medium. Because the absorption of nucleons should preferentially occur on the surface of the nucleus where shell-model orbitals are not completely filled, a surface-peaked imaginary component is usually employed.

The nucleons moving in the nuclear field have spins that can interact with their orbital angular momentum and so a Thomas spin-orbit type potential is also included. This spin-orbit potential is also surface peaked because a nucleon moving through the interior of a nucleus will have no preferred point of reference about which to measure the orbital angular momentum.

The form of the Coulomb potential is

$$\mathrm{V}_C(r) = \begin{cases} \frac{\mathrm{Z}_1\mathrm{Z}_2e^2}{r} & r > R_c \\ \frac{\mathrm{Z}_1\mathrm{Z}_2e^2}{2R_c}\left(3 - \frac{r^2}{R_c^2}\right) & r \leq R_c \end{cases} \tag{2.33}$$

where Z_1 and Z_2 are the charges of the interacting particles and the potential radius is of the form $\mathrm{R}_c = \mathrm{r}_c\mathrm{A}^{1/3}$.

Combining all of these different contributions into one expression gives the total potential as

$$\begin{aligned} \mathrm{V}(\vec{r}) \;=\; & -\mathrm{V}_\mathrm{r} f(r, r_\mathrm{r}, a_\mathrm{r}) - i\mathrm{W}_i f(r, r_i, a_i) - i\mathrm{W}_D \frac{d}{dr} f(r, r_D, a_D) \\ & + \mathrm{V}_\mathrm{so}\left(\frac{\hbar}{m_\pi c}\right)^2 (\vec{L}\cdot\vec{S}) \frac{1}{r}\frac{d}{dr} f(r, r_\mathrm{so}, a_\mathrm{so}) \\ & + \mathrm{V}_C(r). \end{aligned} \tag{2.34}$$

The first derivative of the Woods-Saxon form factor is peaked at the surface, and is thus included in part of the imaginary contribution and the spin-orbit portion. The factor of $(\hbar/m_\pi c)^2$ is the square of the pion Compton wavelength ($= 2.0$ fm^2) and is a standard normalization of the spin-orbit term. The various parameters in each term (strength V or W, radius r, and diffuseness a) are all varied to fit elastic scattering data. As such, the entire optical model potential is phenomenological in its attempt to describe the numerous nucleon-nucleon interactions involved with complex nuclei scattering off one another.

The elastic scattering of A + a and B + b is described with appropriate optical model parameters, but the potential form is local, meaning that at the point $\vec{r}$ the particle feels the potential only at that same point [Gle75]. In reality the wave function of the particle can depend on the conditions everywhere within the

range of the nonlocal potential. Non-locality corrections are available to modify the distorted wave calculations to take this into account.

2.2.3 DWBA, DWUCK4 and Proton Partial Widths

The DWBA cross section is found by calculating the distorted waves $\chi_{a,b}$ and the overlap between the initial and final nuclei $\langle \Phi_B(A+1)|\Phi_A(A)\rangle$. This overlap is calculated using specific quantum numbers for the angular momentum transferred to the target nucleus, based on initial and final spin assignments. The DWBA cross section should then have the correct shape, though perhaps an incorrect normalization. This is because the Φ_B wave function was calculated for the target nucleus A and a single-particle addition, i.e., a pure single-particle state. The amount the DWBA cross sections must be changed in order to agree with experimental proton-stripping angular distribution data will provide the value of the spectroscopic factor, using the relation

$$\left(\frac{d\sigma}{d\Omega}\right)_{exp} = N \frac{(2J_B+1)}{(2J_A+1)(2j+1)} C^2S \left(\frac{d\sigma}{d\Omega}\right)_{DWBA}. \tag{2.35}$$

The factor of N is dependent on the overlap between the projectile and the ejectile of the reaction, for (^{3}He, d) its value is 4.42 [Bas66]. The values J_A, J_B, and j are the initial, final, and transferred angular momenta, respectively.

The levels of interest for nuclear astrophysics correspond to proton-unbound states in the B = A + 1 nucleus. This creates a problem in evaluating the overlap between B and A, since the product wave function does not die away exponentially outside the nuclear radius, but instead oscillates with constant amplitude. The integral over this wave function thus converges very slowly, causing numerical difficulties.

Vincent and Fortune [Vin70, Vin73] have developed a method of contour integration in the complex radius plane in order to evaluate the slowly converging integrals. This method is incorporated into the zero-range DWBA code DWUCK4 of P. D. Kunz by J. R. Comfort [Kun]. The single-particle proton partial width,

$\Gamma_{\rm sp}$, is calculated in this program using the relation [Ili97]

$$\frac{2}{\Gamma_{\rm sp}} = \left(\frac{d\delta}{dE}\right)_{\delta=\pi/2} \approx \frac{2\mu}{\hbar^2 k}\left[\int_0^{R_{max}} |u(r)|^2 dr + \frac{G^2}{2k}\frac{d}{dk}\left(\frac{G'}{G}\right)\right], \tag{2.36}$$

where δ is the phase shift, μ and k are the reduced mass and the wave number of the A + x system, R_{max} is a cutoff radius at which the nuclear potential can be set to zero, G is the irregular Coulomb function evaluated at R_{max}, and $G' = (dG(r)/dr)_{r=R_{max}}$. The function $u(r)$ is the radial wave function calculated from the overlap of A and B in the theoretical A(a,b)B cross section.

The parameter $\Gamma_{\rm p}$ can then be found by forming the state of interest via a $(^3\mathrm{He}, d)$ reaction. Comparing the experimental angular distribution to the DWBA calculated distribution provides a value of C^2S, and the DWBA code simultaneously calculates the single-particle proton partial width.

2.3 Previous Studies of $^{22}\mathrm{Ne}(p,\gamma)$ and $^{23}\mathrm{Na}(p,\gamma)$

Numerous studies of the reactions in the NeNa cycle have been performed since it was first described by Marion and Fowler [Mar57]. A re-evaluation of the existing data was presented in EEC95, which will be used as a guide to the current understanding of the two reactions under study here.

2.3.1 $^{22}\mathrm{Ne}(p,\gamma)^{23}\mathrm{Na}$

The energy level diagram for the $^{22}\mathrm{Ne}(p,\gamma)^{23}\mathrm{Na}$ reaction is shown in Figure 2.2. The excitation energies are taken from Endt [End90a]. The Q-value (8794.1 $\pm$ 0.3 keV) and the resonance energies have been recalculated using the 1995 update on mass evaluations [Aud95]. Updated excitation energies are presented in Chapter 5, using the results of the present study and a re-evaluation of previous data taking the Audi & Wapstra 1995 masses into account. The J^π of the ground state of ^{22}Ne is 0^+.

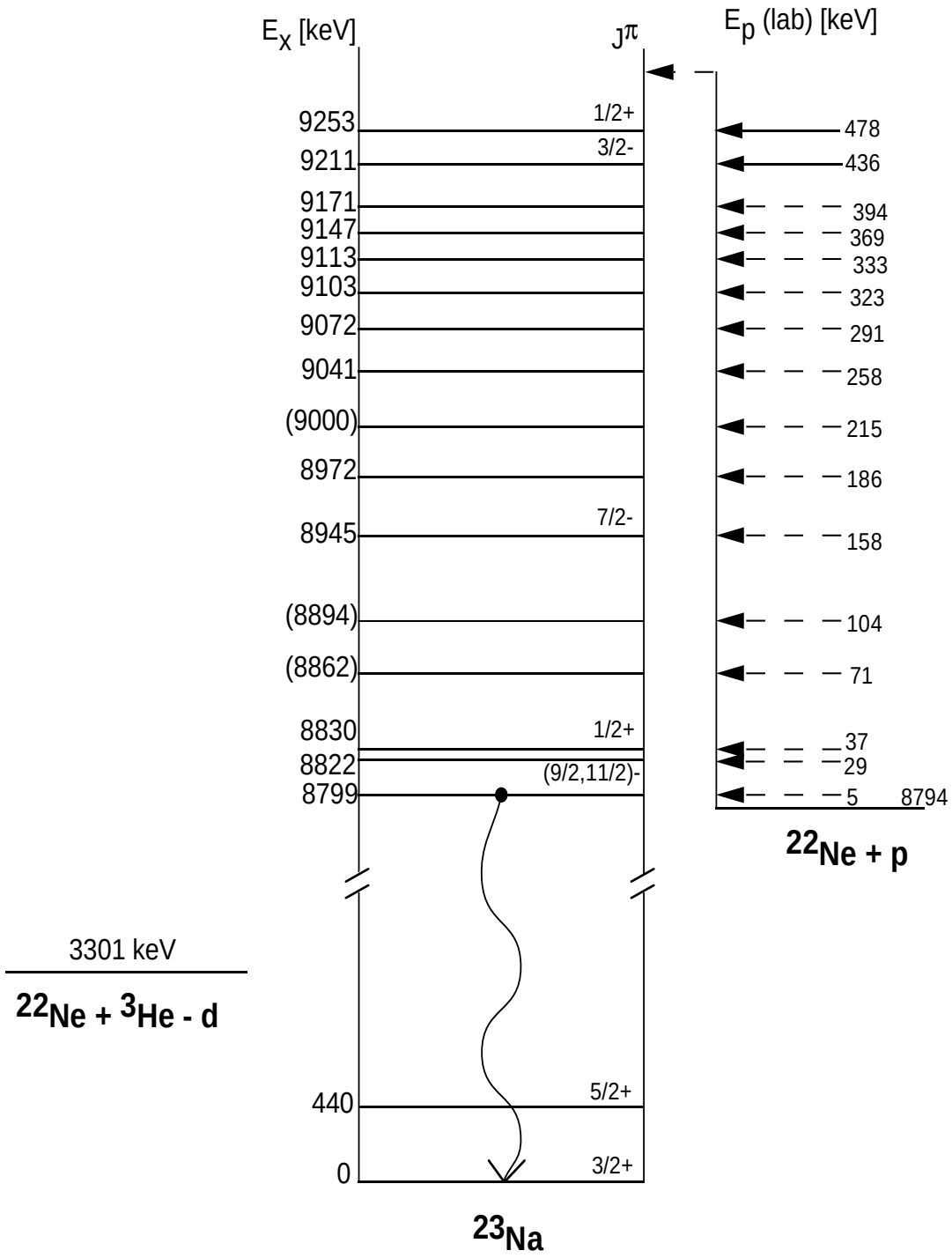

Figure 2.2: Energy level diagram for the $^{22}\mathrm{Ne}(p,\gamma)^{23}\mathrm{Na}$ reaction. Excitation energies and quantum numbers are taken from [End90a]. Resonance energies are calculated using the new Q-value [Aud95].

With the numerous resonances above the (p,γ) threshhold of 8794 keV, the dominant contribution to the reaction rate in the temperature region of interest for red giants is from resonant capture. The contribution from direct capture has been measured by Rolfs *et al.* [Rol75] and by Görres *et al.* [Gör83]. The contribution from the high-energy tail of a subthreshold $J^\pi = \frac{1}{2}^+$ state at E_x = 8664 keV (E_{cm} = -130 keV) has been shown to be negligible by Görres *et al.* [Gör83].

Resonances have been searched for via a direct measurement [Gör82] and by direct capture into the unbound states [Gör83] below the lowest measured resonance at E_{lab} = 436 keV. Of the 14 states thought to lie below this energy, none were observed. Three of these states have been seen in the proton-stripping reactions $(^3\mathrm{He}, d)$ [Pow71] and (d, n) [Chi73] which correspond to the states at 8830 keV, 8945 keV, and 8972 keV. The state at 8822 keV has been observed via $^{19}\mathrm{F}(^6\mathrm{Li}, d)^{23}\mathrm{Na}$ [For95] with an angular momentum transfer of 5, resulting in a J^π assignment that makes the state unimportant in the stellar reaction rate. The state at 8799 keV is too low in energy to make any contribution.

Upper limits on the resonance strengths and proton spectroscopic factors are reported in Görres *et al.* (1982, 1983) which leave only the possible states at 8862 and 8894 keV as significant contributors to the reaction rate. These two states, along with the 9000-keV state, were reported by Powers *et al.* [Pow71], as being weakly populated, so weak in fact that their existence should be considered tentative. Unfortunately, if they exist as resonances at E_{lab} = 71 and 104 keV they can contribute greatly to the reaction rate.

The re-evaluation by EEC95 examined all published spectroscopic factors and used a Woods-Saxon potential to describe the single-particle states in order to compute proton partial widths, which determine resonance contributions to the reaction rate. The direct capture contribution was adopted from Görres *et al.* The individual contributions from states above the lowest observed resonance at E_{lab} = 436 keV were summed together and fit. Their resulting reaction rate is

given by

$$\begin{aligned} N_A \langle \sigma v \rangle &= 1.05 \times 10^9 T_9{}^{-2/3} \exp(-19.431/T_9{}^{1/3}) \\ &+ 1.24 \times 10^{-9}\, T_9{}^{-3/2} \exp(-0.414/T_9) \\ &+ 0.029\, T_9{}^{-3/2} \exp(-1.752/T_9) \\ &+ 9.30 \times 10^4\, T_9{}^{-1.174} \exp(-5.100/T_9) \\ &+ 5.71 \times 10^5\, T_9{}^{-0.249} \exp(-7.117/T_9) \\ &+ [0-1] 3.25 \times 10^{-4}\, T_9{}^{-3/2} \exp(-0.789/T_9) \\ &+ [0-1] 0.10\, T_9{}^{-3/2} \exp(-1.161/T_9) \\ &\text{cm}^3 \text{ mole}^{-1} \text{ sec}^{-1}. \end{aligned} \tag{2.37}$$

The first three terms in this expression represent direct capture, the 37-keV resonance, and the 158-keV resonance. The next two terms cover the contribution of resonances for $E_{lab} \geq 436$ keV. The last two terms, with the [0−1] factors, describe the possible resonances at 71 and 104 keV. The reaction rate is shown in Figure 2.3. The contribution from the two tentative resonances results in large uncertainties, from a factor of 2 at $T_9 = 0.030$ to a factor of 3400 at $T_9 = 0.080$.

The reaction ^{22}Ne(^{3}He, d)^{23}Na is studied in this work in the hope that improved spectroscopic information will lead to reduced uncertainties.

2.3.2 ^{23}Na$(p,\gamma)^{24}$Mg

The situation for ^{23}Na$(p,\gamma)^{24}$Mg is slightly more complicated because of the open (p,α) channel. The energy level diagram is shown in Figure 2.4 for the region within 400 keV of the proton threshhold. The excitation energies are taken from Endt [End90a] while the Q-value (11692.9 ± 0.3 keV) and resonance energies are calculated using Audi & Wapstra's 1995 mass excess values. Updated excitation energies are presented in Chapter 6, using the results of the present study and a re-evaluation of previous data taking the Audi & Wapstra 1995 masses into account. The J^π value of the ^{23}Na ground state is $\frac{3}{2}^+$.

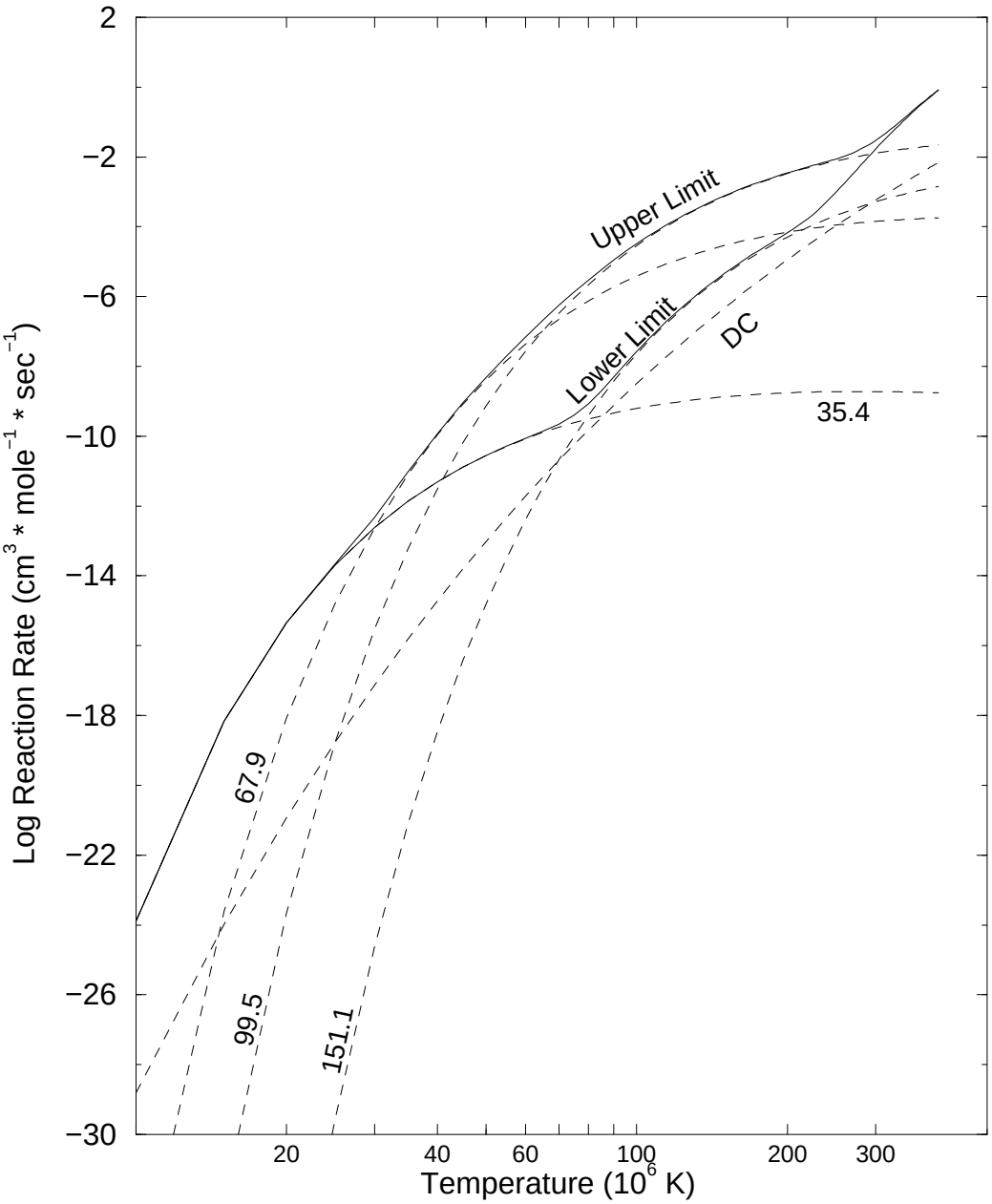

Figure 2.3: ^{22}Ne$(p,\gamma)^{23}$Na reaction rate from EEC95 [EEC95]. The dashed lines represent individual contributions from resonances or direct capture as labelled, in center-of-mass energies.

Zyskind *et al.* [Zys81] studied the (p,α) reaction while Görres *et al.* [Gör89] investigated both the (p,γ) and the (p,α) reaction. The lowest observed resonance is located at 179 keV. The J^π of the level 4 keV below this prevents it from being astrophysically important. The state located at 11695 keV is only a 2 keV

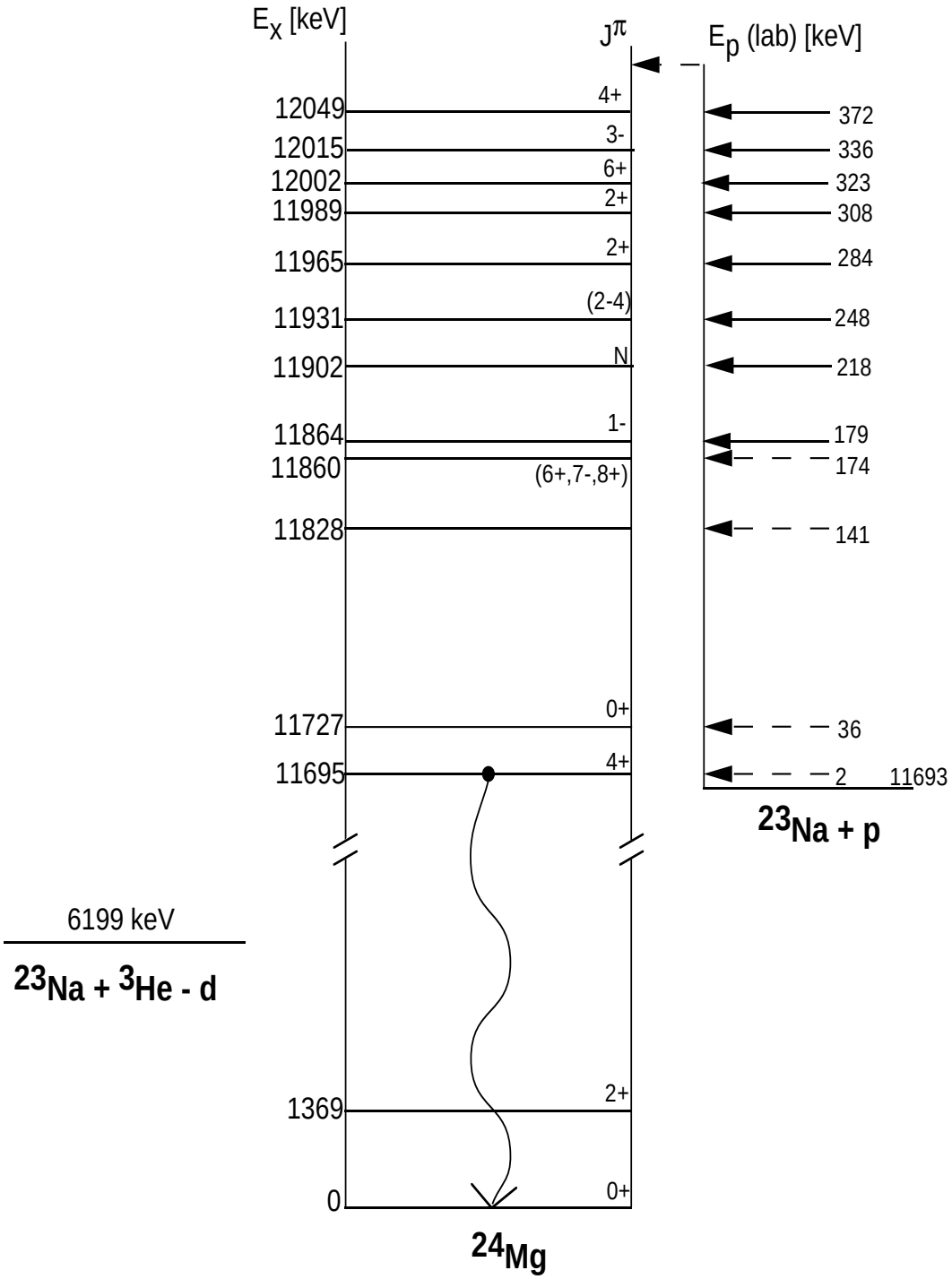

Figure 2.4: Energy level diagram for the ^{23}Na(p,γ)^{24}Mg reaction. Excitation energies and quantum numbers are taken from [End90a] (N = natural parity). Resonance energies are calculated using the new Q-value [Aud95].

resonance in the (p,γ) reaction, and is astrophysically unimportant because of its small width.

After reviewing the existing data on widths and spectroscopic factors, EEC95 obtained the following rate for the ^{23}Na$(p,\gamma)^{24}$Mg reaction

$$\begin{aligned} \mathrm{N_A}\langle\sigma \mathrm{v}\rangle &= 2.47\times10^{9}\,{\mathrm{T_9}}^{-2/3}\,\exp(-20.758/{\mathrm{T_9}}^{1/3}) \\ &\quad + 91.9\,{\mathrm{T_9}}^{-3/2}\,\exp(-2.789/\mathrm{T_9}) \\ &\quad + 1.72\times10^{4}\,{\mathrm{T_9}}^{-3/2}\,\exp(-3.433/\mathrm{T_9}) \\ &\quad + 3.44\times10^{4}\,{\mathrm{T_9}}^{0.323}\,\exp(-5.219/\mathrm{T_9}) \\ &\quad + [0-1]2.34\times10^{-4}\,{\mathrm{T_9}}^{-3/2}\,\exp(-1.590/\mathrm{T_9}) \\ &\quad \mathrm{cm^3\ mole^{-1}\ sec^{-1}} \end{aligned} \tag{2.38}$$

The first three terms are direct capture, the 248-keV resonance and the 308-keV resonance. The fourth term describes higher energy resonances, and the last term is the upper limit on the 141-keV resonance.

The DC capture contribution was estimated using tabulated spectroscopic factors and the model of Rolfs [Rol73]. The 36-keV resonance does not contribute strongly to the reaction rate because of the limit on the resonance strength of $\omega\gamma \leq 2.3\times10^{-23}$ eV. A value of $\mathrm{C^2S} \leq 0.1$ was estimated for the 141-keV resonance, however there is no width information available for this state. To obtain the upper limit, EEC95 assumed that $\Gamma_\gamma/\Gamma \approx 1$. Combining this with $\Gamma_\mathrm{p} \leq 2.3\times10^{-9}$ eV from their diffuse nuclear potential calculations and a maximum spin of J = 2, they arrived at $\omega\gamma \leq 1.4\times10^{-9}$ eV. The reaction rate, with the individual contributions, is shown in Figure 2.5. It is uncertain by about a factor of 2 near $\mathrm{T_9} = 0.080$.

The reaction ^{23}Na$(^3\mathrm{He},d)^{24}$Mg is investigated in this work to obtain spectroscopic factors and Γ_p values for the region of interest.

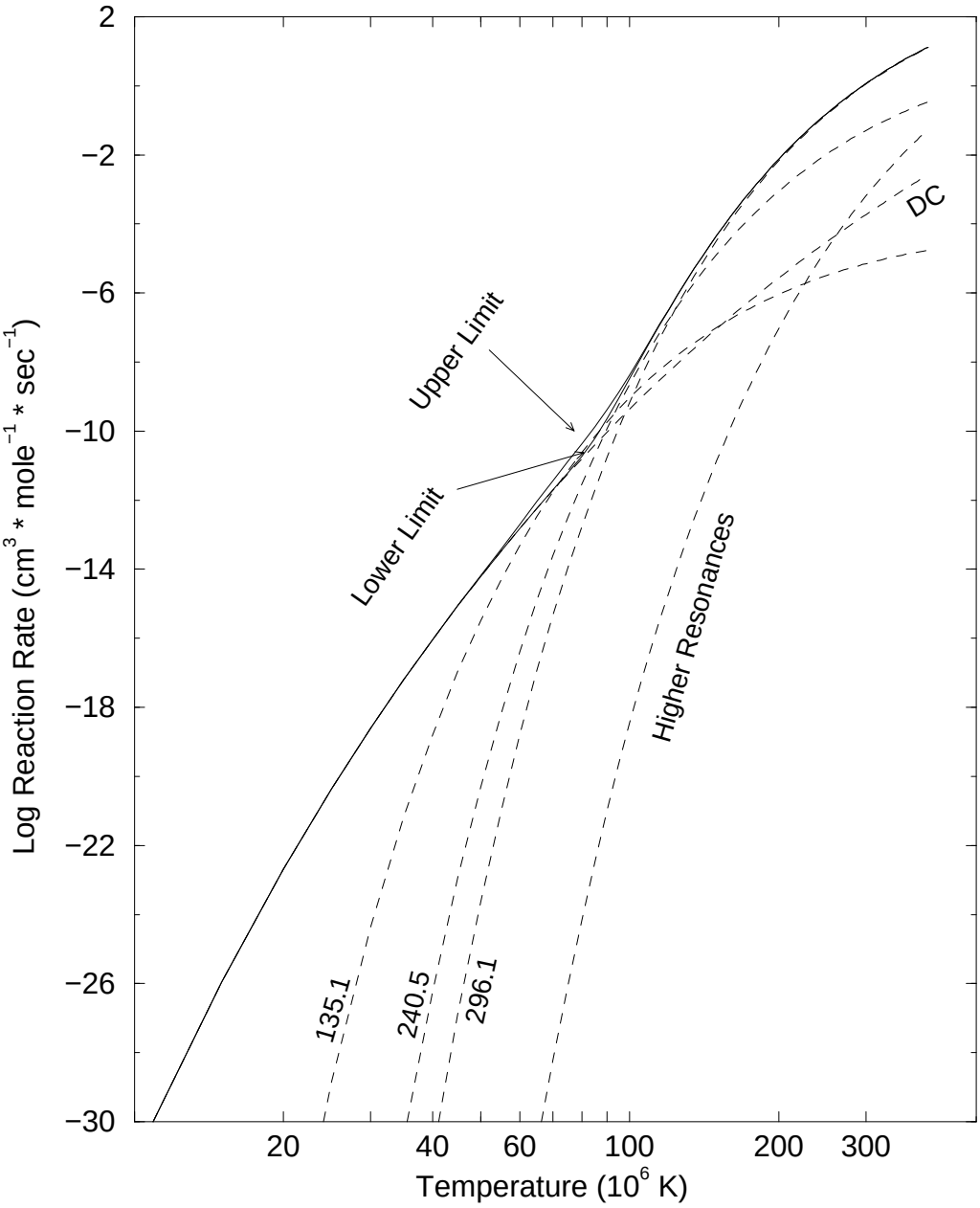

Figure 2.5: ^{23}Na(p,γ)^{24}Mg reaction rate from EEC95 [EEC95]. The dashed lines represent individual contributions from resonances or direct capture as labelled, in center-of-mass energies.

Chapter 3

Detector and Electronics

3.1 Requirements of Enge Focal Plane Detector

In order to study the proton-stripping reactions of interest, the TUNL Enge Split-Pole Spectrometer was chosen. The magnetic spectrometer is designed to focus outgoing particles from nuclear reactions onto a focal plane, while changing the spread in energy into a spread in position. The requirements that the Enge places on a detector are related to the design characteristics of the spectrometer system.

The factors that determine the image size on the focal plane are the magnification, M, of the object size (beam spot on target) and optical aberrations that influence the particle trajectories as they pass through the magnetic field. The magnification of the Enge in the horizontal (dispersing) plane is 0.33 [Spe67], so a 1 mm beam spot on target will produce a nominal 0.33 mm wide peak on the focal plane. The beam-spot size required for the experiment is determined by the dispersion of the Enge. This dispersion is a measure of how much the energy range of the particles are spread out in position. For the Split-Pole the value is $\mathrm{D} = 1.75\,\mathrm{MeV}\,\frac{\mathrm{mm}}{\mathrm{keV}}$. For a beam spot size of S, the resolving power is given by

$$\mathrm{RP} = \frac{\mathrm{E}}{\Delta\mathrm{E}} = \frac{1}{2\mathrm{S}}\frac{\mathrm{D}}{\mathrm{M}}, \tag{3.1}$$

where for the Split-Pole values of D and M this becomes

$$\mathrm{RP} = \frac{1}{\mathrm{S}}\, 2651.5\,\mathrm{mm}. \tag{3.2}$$

The energy ranges of the deuterons of interest for the two proton-stripping reactions being measured is roughly 12 MeV to 15 MeV. For a typical deuteron energy of 14 MeV, a 1 mm beam spot will lead to an energy resolution of 5.3 keV, with the resolving power given in Equation 3.2. Thus, the detector that is to be used with the Enge needs to have sub-millimeter position resolution in order to fully take advantage of the beam-spectrometer combination.

The aberrations that can lead to loss of position resolution can be characterized as

$$\mathrm{x} = \mathrm{x}_0 + \left(\frac{\mathrm{dx}}{\mathrm{d}\theta}\right)\mathrm{d}\theta + \frac{1}{2}\left(\frac{\mathrm{d}^2\mathrm{x}}{\mathrm{d}\theta^2}\right)\mathrm{d}\theta^2 + \frac{1}{2}\left(\frac{\mathrm{d}^2\mathrm{x}}{\mathrm{d}\phi^2}\right)\mathrm{d}\phi^2 + \ldots \tag{3.3}$$

where x is the measured position on the focal plane, x_0 is the nominal position assuming a perfect magnetic field in the Enge, and the derivatives of x with respect to θ and ϕ come from the effects of extended fringing fields. In order to minimize the aberrations, the Enge consists of a dipole magnet with the typical single pole tip split in two, but left enclosed in the same current carrying coil. The shapes of the pole edges can be machined to correct for the aberrations; for the Split-Pole this is done to second order. The particles pass through multiple magnetic fringe fields that have a vertical focusing effect, thus focussing the particles such that they avoid hitting the Enge magnet pole tips and allowing for a larger vertical acceptance. The result is a practical, resolution-limited, maximum acceptance of $\pm$ 70 mr (horizontal) and $\pm$ 40 mr (vertical). This leads to an overall solid angle of 2.8 msr. Increasing the horizontal acceptance of the aperture leads to a loss of resolution, as the particles from the edges of the aperture are focussed away from the focal plane.

Initially, a position sensitive Si telescope produced by Micron was going to be used. This detector consisted of a front silicon detector which would provide position and energy loss information, and a backing silicon detector which would

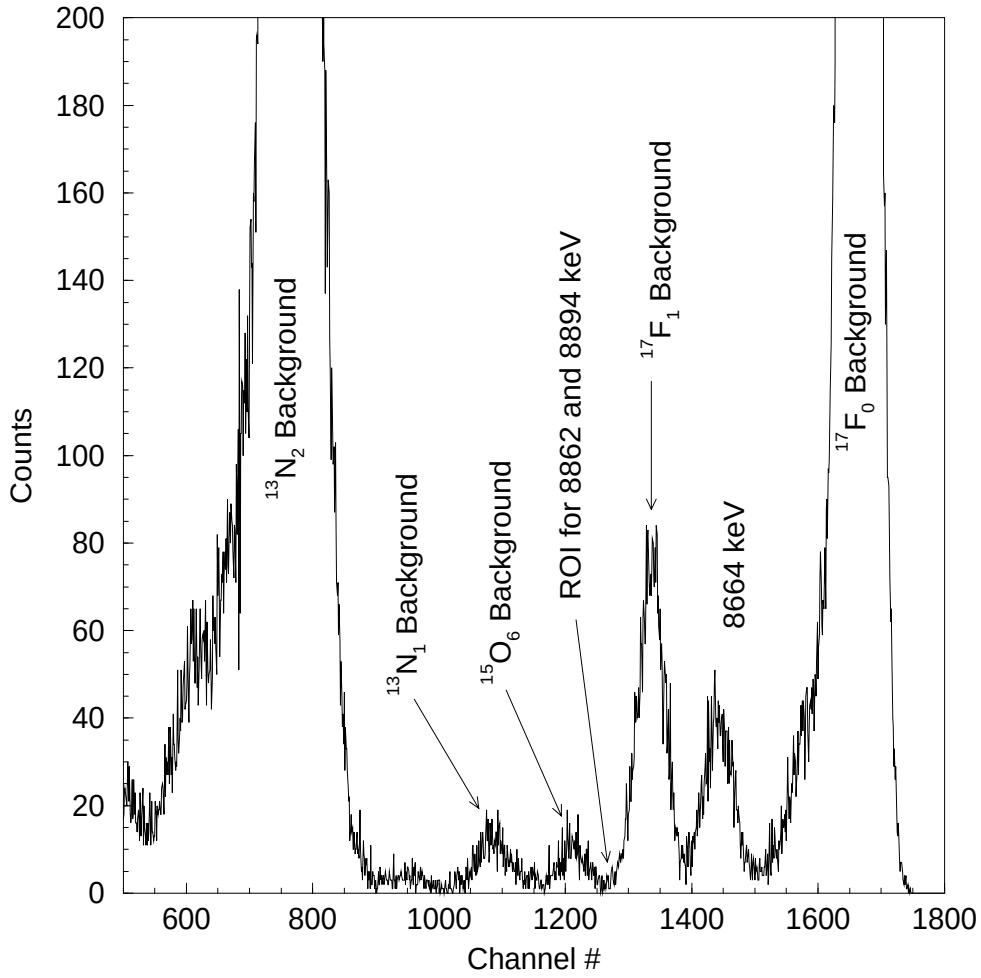

Figure 3.1: Spectrum from silicon position sensitive detector for ^{22}Ne(^{3}He,d)^{23}Na at 10°.

provide a total energy signal. The system was tested in April, 1995, and was found to have insufficient energy resolution for our purposes. A sample spectrum is shown in Figure 3.1 for the reaction $^{22}\mathrm{Ne}(^3\mathrm{He}, d)^{23}\mathrm{Na}$ at 10°. The region of interest for the 8862- and 8894-keV states is indicated and it can be seen that the usefulness of the data is compromised by the resolution, which was approximately 50 keV. For this reason, it was decided in the summer of 1995 to design and construct a new focal plane detector based on a different measurement technique.

3.2 Overview of Detector Requirements

The new focal plane detector was designed to be able to measure the position of the particles on the focal plane, a differential energy loss, a total energy, and the incident angle of the particles on the focal plane. The energy loss and total energy signals would allow particle identification. The purpose of measuring the angle is to reconstruct the trajectories of the particles so that the portion of the entrance aperture from which the particles came could be determined, and larger solid angles could be used in data collection. At the same time, the loss of resolution that would result if the position measurement were made away from the focal plane could be corrected. These corrections would be carried out offline. Another bonus of the angle measurement is the possibility of using a multiple-angle aperture and thus collecting data at several angles simultaneously.

With these requirements, a transmission device was chosen in which the particles would interact with four separate sections before stopping completely. To achieve this, gas-filled sections were chosen for the first three portions of the detector and a stopping detector for the final portion. The detector consists of two position measuring sections, separated by an energy loss section and backed by a plastic scintillator. A side view of the full detector is shown in Figure 3.2.

The front three sections utilize high-voltage wires in an ionization gas, currently isobutane, to create avalanches of electrons as particles pass through the gas. These bursts of charge are measured in different ways in the position sections and the energy loss section. Descriptions of both the fabrication and operation of the individual sections will be given in Section 3.3. The gas in the detector is isolated from the vacuum system of the spectrometer with a 25 μm-thick Kapton window. The energy loss section is the support piece for the detector, with the other three sections mounting onto it. The four sections are independently assembled before being attached to the ΔE section. Mounts for attaching the detector to the spectrometer focal plane table are attached to the bottom of

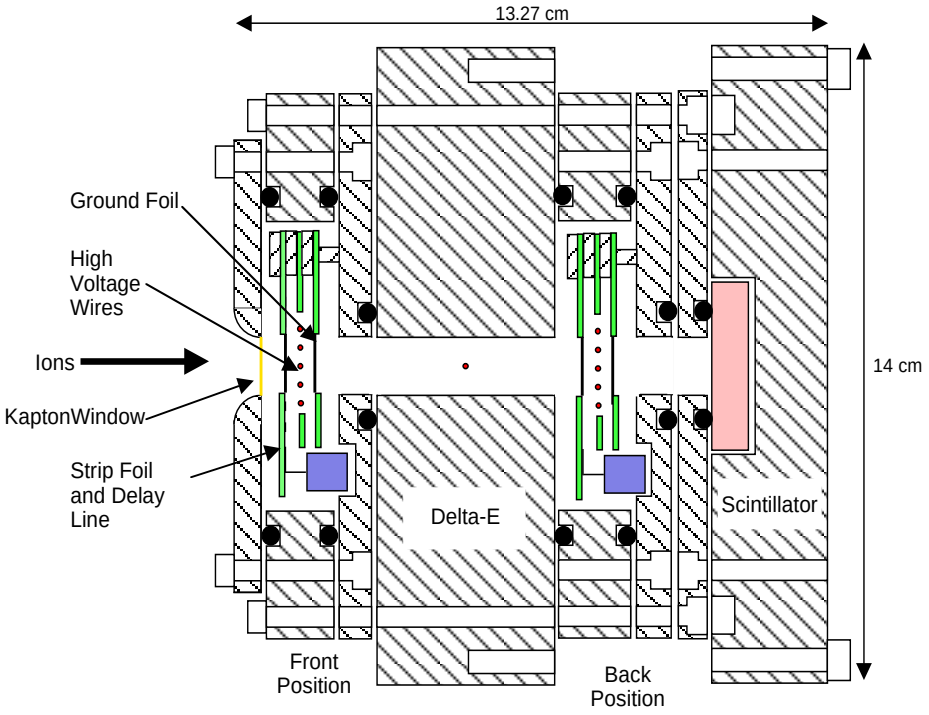

Figure 3.2: Sideview of the TUNL Enge Split-Pole Spectrometer focal plane detector.

the ΔE section. The dimensions of the overall system, with preamplifiers and supports attached, are 140 cm long, 30 cm high and 18 cm deep. The fully assembled detector weighs $\approx$ 32 kg. The weight is a slight problem while working on the detector, but not so much as to prevent single-person maintenance during a midnight shift of the experiment.

3.3 Fabrication and Operation

3.3.1 Position measuring sections

The position is derived over a depth of 6 mm. The active region is bounded by a plain ground plane and an image-charge pickup plane, grounded through a delay line. The high-voltage wires are stretched horizontally through the middle

of the two planes, transverse to the particle trajectory, and are mounted on a separate board. The three boards that make up the system are 5.1 cm high by 61 cm long with a 1.27 cm by 54.6 cm gap milled completely through for particles to pass.

The wire board is made of insulated G-10 with four 25 μm Au-plated Tungsten wires (California Fine Wire Company) stretched tight lengthwise across the gap and soldered into holes covered with copper tape. A short wire is also soldered onto the copper tape to electrically connect the wires to an SHV feedthrough in the detector frame for applying high voltage. The wires are typically biased to $\geq$ 2000 V. Movement of the wires under bias could produce non-uniform electric fields and undesirable sparking. Therefore the wires are tensioned to 0.98 N while being soldered in place (the breaking tension was measured to be 1.18 N). The solder joints on each end of the board are coated with TV-corona dope (GC Electronics) in order to prevent sparking. In order to avoid damaging the delay lines used in the measuring process, the HV wires are biased through a protection circuit shown in Figure 3.3, as adopted from a detector once used at MSU [Mar75]. The diode decouples the anode from the 120 pF capacitor during a spark to limit the peak voltage on the delay line. The high voltage is applied using current-limited power supplies that are set to trip off in the event of uncontrolled sparking.

Separated from the wire plane by 3 mm on either side, are the two boards forming ground planes. The plain ground board is formed from an Al frame of the same height and width as the wire board with a similar gap machined through the center. Aluminized mylar (0.3 μm thick) is stretched taut across the gap and attached with double-sided tape. Since the tape forms an insulated contact, the mylar is stretched across the top of the aluminum frame and partially down the other side to make electrical contact along the top edge. The mylar is attached to the back side again with double-sided tape. This board makes direct contact with the detector housing.

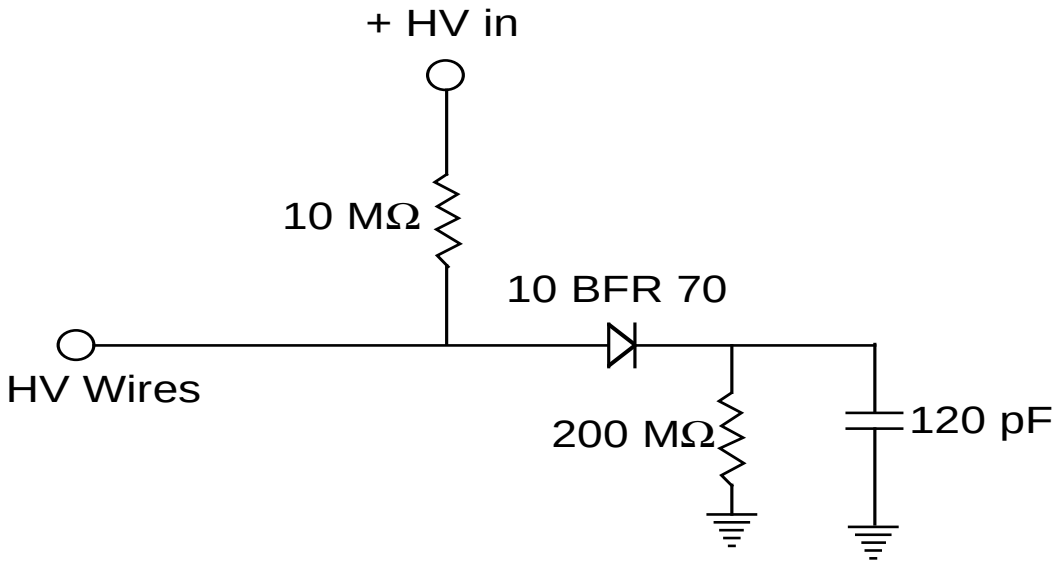

Figure 3.3: Protection circuit for biasing HV wires in position sensing section of detector.

The other plane facing the HV wires is the position measuring board. The board is copper clad G-10 machined to have a series of 200 isolated vertical copper strips below the gap in the board. Two holes are drilled into each copper strip and two rows of in line sockets are soldered across the board. Single-sided aluminized mylar is stretched taut across the gap in the board and held in place again with double-sided tape. The board is then taken to the Duke Physics Instrument Shop and placed on a computer-driven milling machine. A felt-tip pen, with the ink removed, is filled with NaOH and placed in the spindle. The mill is then used to draw a series of lines of NaOH across the aluminized mylar [Gra95]. This results in the chemical reaction

$$2\mathrm{Al(s)} + 2\mathrm{NaOH(aq)} + 2\mathrm{H_2O} \longrightarrow 2\mathrm{AlO_2^-(aq)} + 2\mathrm{Na^+(aq)} + 3\mathrm{H_2(g)}. \qquad (3.4)$$

The acqueous $\mathrm{AlO_2^-}$ is then washed off of the mylar with distilled water. The aluminum remaining on the mylar above and below the gap through the board is removed with NaOH to prevent any shorts between strips. A total of 200 vertical strips of electrically isolated aluminum are produced. The strips are 2.54 mm across, separated by a gap of approximately 0.5 mm.

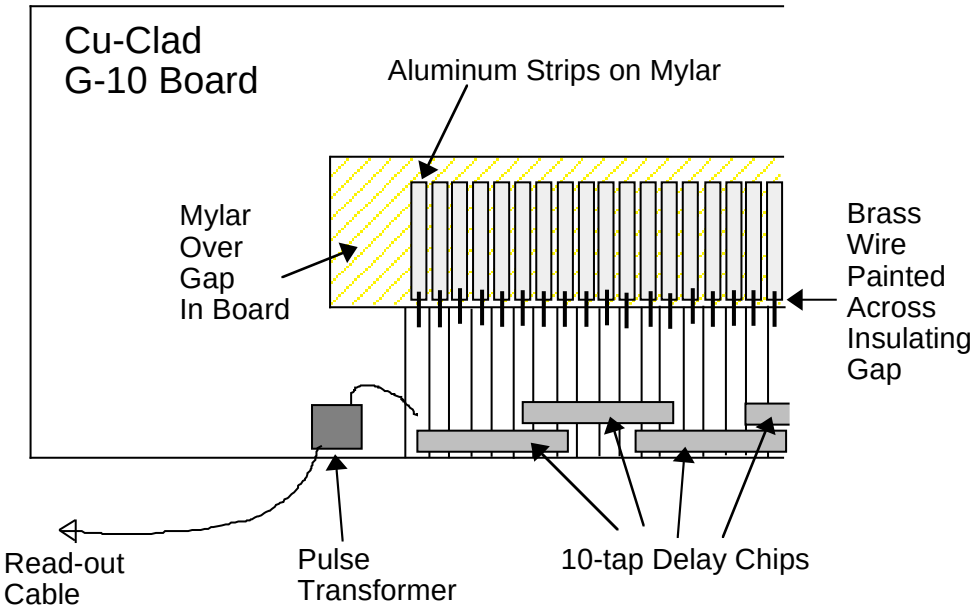

Figure 3.4: Details of one end of the position measuring boards used in the Enge focal plane detector. See text for description of individual parts.

Once the board is cleaned off, small segments ($\approx$ 1 cm in length) of 0.125 mm diameter brass wire (Goodfellow Metals Ltd.) are attached to each segment of aluminum on the mylar and the corresponding copper strip on the G-10 board below the aluminum strip. The wires are painted into place using silver conducting paint manufactured by GC Electronics. This provides an electrical connection from the aluminum strips to the taps on 20 individual 10-tap lumped constant delay chips (Technitrol Inc. #SF10K1) which are plugged into the rows of socket strips in an overlapping pattern. The delay per tap is 5 ns, so the 200 strips are connected to 200 taps on a 1 μs delay line. The impedance of the delay chips (100 Ω) is matched to the 50 Ω preamps using pulse transformers (Mini-Circuits #T1.5-6) soldered onto each end of the board. The signal then passes through a short cable to a single-pin BNC feedthrough on the side of the detector housing and out to the signal processing electronics. A schematic showing one end of the boards with the features described above is shown in Figure 3.4.

The back position measuring section, located after the ΔE section described in Section 3.3.2, is constructed in a similar manner to the front. One difference in the two sections is that an extra ground plane board is placed at the entrance to the back section to provide the back ground plane for the energy loss section. This board is constructed in the same manner as the position measuring board, but without the etching and delay line attachments.

The position measurement is performed as follows: Particles exiting the Enge's magnetic field region pass through the front Kapton window which contains a 200 torr isobutane environment inside the detector. They pass through the position sensitive board with its 200 aluminum strips. Electrons knocked off of isobutane molecules are attracted to the HV wires, gaining energy in the electric field of $\geq$ 6.7 kV/cm. Close to the wires the electrons have gained enough energy to begin ionizing isobutane molecules. This leads to an avalanche of charge centered at the location of the particle as it passes the HV wires. This cloud of electrons induces a positive charge on the Al strips nearest the avalanche in a pattern shown in Figure 3.5. This method is used in several other detectors, see *e.g.* [Mar75].

The image charge is conducted through the Al strip, the silver paint, and the connecting brass wire to the taps on the delay chips. The signal splits and travels through the left and right segments of the delay line. The rise time of the signals carries the position information. The centroid of the charge distribution is found through interpolation of these signals. A timing difference is then used to convert the two signals into a position signal. The signals are processed in dedicated electronics described in Section 3.4.

The back position section operates in the same manner, resulting in a total of four signals, front left and right and back left and right. This provides two position measurements, one on the focal plane of the Enge and one located behind it by $\approx$ 5 cm. The front and back position signals are processed in the software to produce an angle signal.

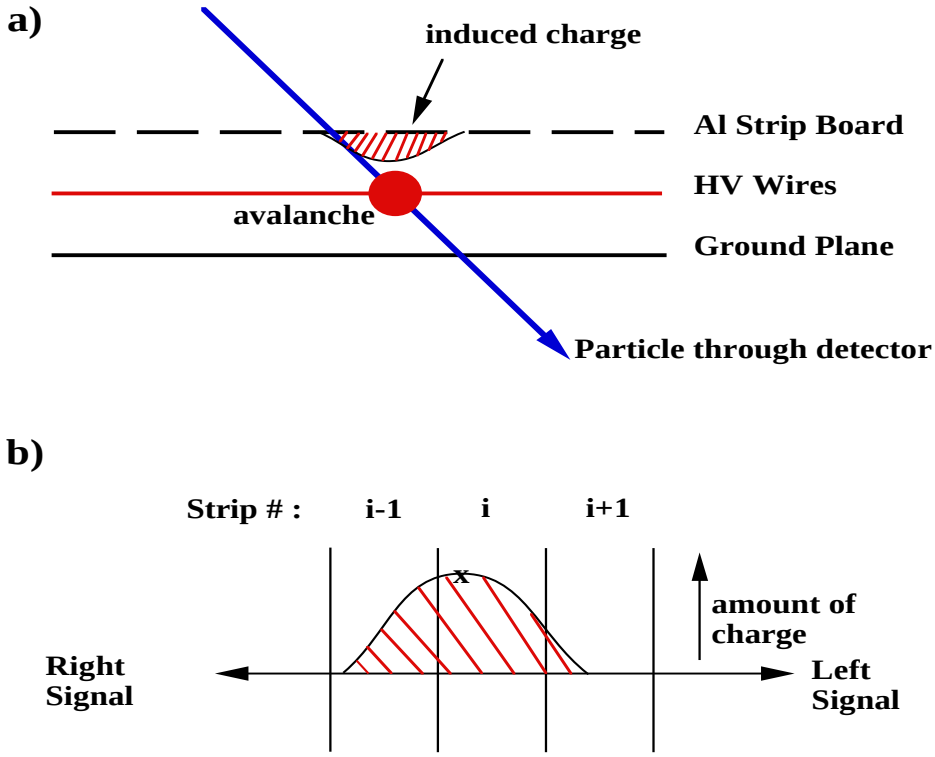

Figure 3.5: Mechanism used in the position measurements. a) Top view of particle's passage through the position measuring section showing the avalanche of electrons on the HV wire and the induced image charge. b) Head-on view of image charge spread across several adjacent strips centered over the x.

3.3.2 Energy loss section

The particles of interest exit the front position section and pass into a 5.08 - cm deep by 1.27 - cm high gap in a solid aluminum piece which contains a single 12.7 - μm diameter wire (Stablohm 650, California Fine Wire Company) stretched parallel to the Enge focal plane. The wire is soldered onto SHV feedthroughs allowing it to be biased to + 1000V. Unfortunately, the breaking tension of the wire is small enough to preclude stretching it with any significant weight. Instead it is pulled slightly taut against the aluminum chassis and held in place with tape while being soldered. The ground planes for this section consist of the top and bottom of the gap in the aluminum piece, the normal ground plane in the front position measuring section and the extra ground board

included in the back position measuring section. The bias is applied through a charge-sensitive preamplifier which measures the energy deposited in this section, providing an energy-loss signal. The bias of the wire is limited so that the energy-loss measurement takes place in the proportional mode.

3.3.3 Total-energy scintillator

The last section of the detector consists of a 6.35-mm thick plastic scintillator (Bicron BC-404 Plastic) which stops the particles and provides a total energy signal. The scintillator is shielded from the isobutane segments of the detector with a 12.7-μm thick Al foil. The foil serves as both a light shield as well as the back vacuum seal between the isobutane and the Enge vacuum chamber. A photomultiplier tube (Burle #8575) is attached to the scintillator and biased to 2000 V. An Ortec 265 photomultiplier base is used for signal preamplification.

3.4 Electronics

Preamplifiers for the four position signals are attached to the detector itself inside the vacuum chamber. The ΔE preamp is located at the feedthrough plate into the chamber. A total of seven signals are sent from the detector into the control room electronics. They are: front position left and right, energy-loss, back position left and right, and the anonde and dynode signals from the scintillator preamp. A schematic of the overall electronics is shown in Figure 3.6.

The four position signals are processed through an Ortec 863 Quad Timing Filter Amplifier and then fed into a Phillips 715 5-Channel Constant-Fraction Discriminator to obtain a time reference. The left signal forms the start of a Time-to-Amplitude Converter. The right signal from the two sections passes through a 1 μs delay box and then into the stop on the TAC (Ortec 567). This converts the $\pm$ 1 μs delay from the detector into a $0 - 2$ μs delay. The TAC options are set to convert the 2 μs time scale into a 10 V analog signal. The

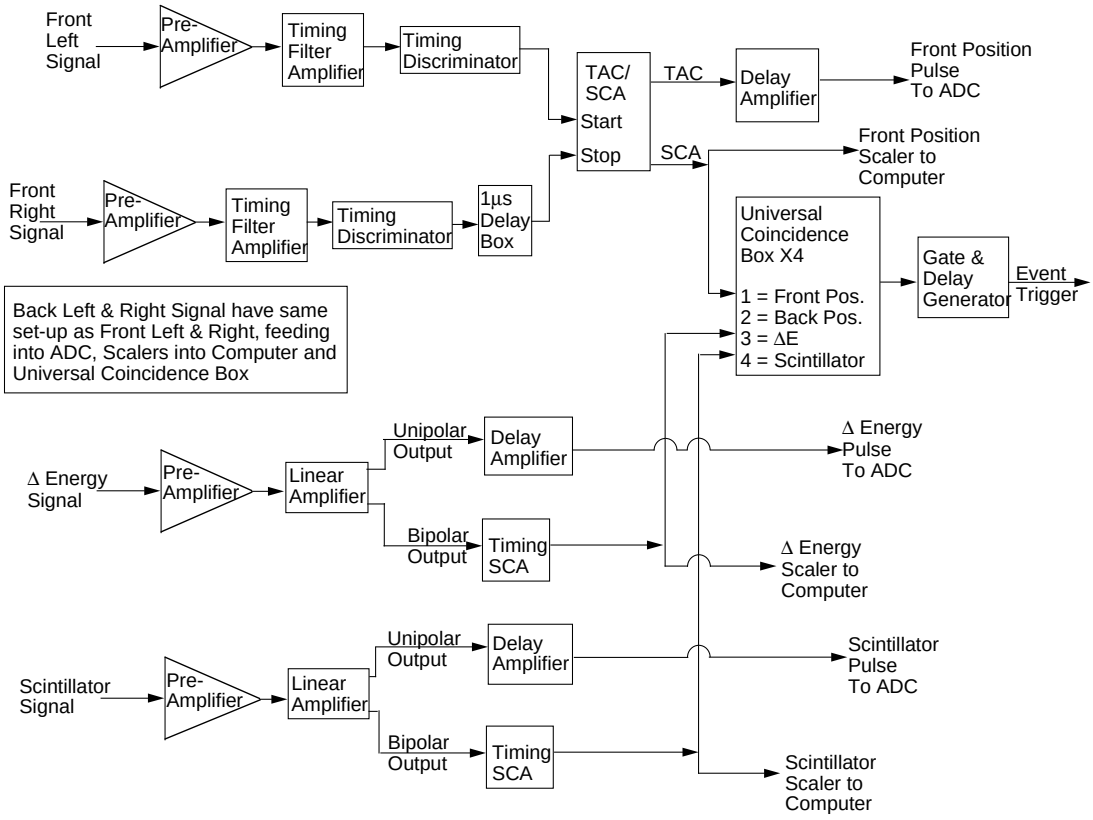

Figure 3.6: Schematic of the signal-processing electronics used with the Enge focal-plane detector. See the text for details.

ordering of the starts and stops places the high-energy side of the detector at the upper end of the time scale. The TACs also provide a simultaneous trigger signal for each position section.

The ΔE preamp and Scintillator dynode signals are fed into individual Ortec 572 Amplifiers. The unipolar output of the amplifiers are passed through delay amplifiers and then on to the ADC. The bipolar output is further processed through Ortec 551 Timing SCAs in order to provide triggers for the event logic.

The outputs of the four SCA modules from the four detector sections are fed into a Universal Coincidence box. This provides a common trigger for the ADC with the requirement that all four sections fire for a valid event. The SCA count rates are monitored to detect any uncontrolled sparking in the detector which manifests itself as a large excess of counts (up to a factor of 10−100) in a single

section. The sections most susceptible to sparking are the three isobutane-filled sections and are all biased with current-limited Bertan supplies. The monitor outputs of these supplies are used as data collection inhibitors in the event that one or more sections trip off.

The dead time for the detector was monitored using the triggers created by the coincidence box compared to the number of events processed by the computer. In the event of a large dead time, the beam current on target was reduced. The detector could operate normally at a count rate of about 10 kHz.

Two different ADCs were used over the course of data collection. It was found that the Silena ADC used in the first several runs produced a marked non-linearity in the position spectrum, so an Ortec AD811 was used in the last run for calibration checks. The data were stored in event mode using the XSYS data acquisition and analysis system, so that the runs could be replayed to test various cuts in the ΔE-E particle ID.

3.5 Results of Test Runs

The full detector was first assembled in January, 1996. Debugging then commenced in earnest. The main recurring problems were shorting of the position signals through spurious contacts to the copper cladding on the G-10 board and capacitive coupling between adjacent aluminum strips that short-circuits the delay line. Careful attention to the assembly of the position sections alleviated these problems. The general procedure was to pass a pulser signal through the delay-line board and observe it relative to the pulser trigger with an oscilloscope. This was done at various stages of assembly to confirm the presence of a signal and the absence of a short around the delay line.

The fill gas for the detector has been changed several times. In order to obtain a larger signal while avoiding excessive sparking the original propane gas has been changed to isobutane. Different grades of both gases have been

tested. The higher gain of the isobutane gas allows lower voltages to be used while maintaining signal strength. The operating procedure involved running CP grade isobutane gas through an MKS regulator to keep the pressure at a constant 200 torr and the flow rate at 100 cc/min.

A test was made using the ^{162}Dy(p,p) reaction at $E_p = 12$ MeV in May 1996. A spectrum is shown in Figure 3.7. The observed resolution of the detector was 9.6 keV, or about 0.91 mm along the focal plane, and includes both beam and target contributions. The energy spread in the beam is on the order of 0.5 keV. Thus the combined target and detector effects contribute on the order of 9 keV to the resolution. This was well within the goals of sub-mm resolution.

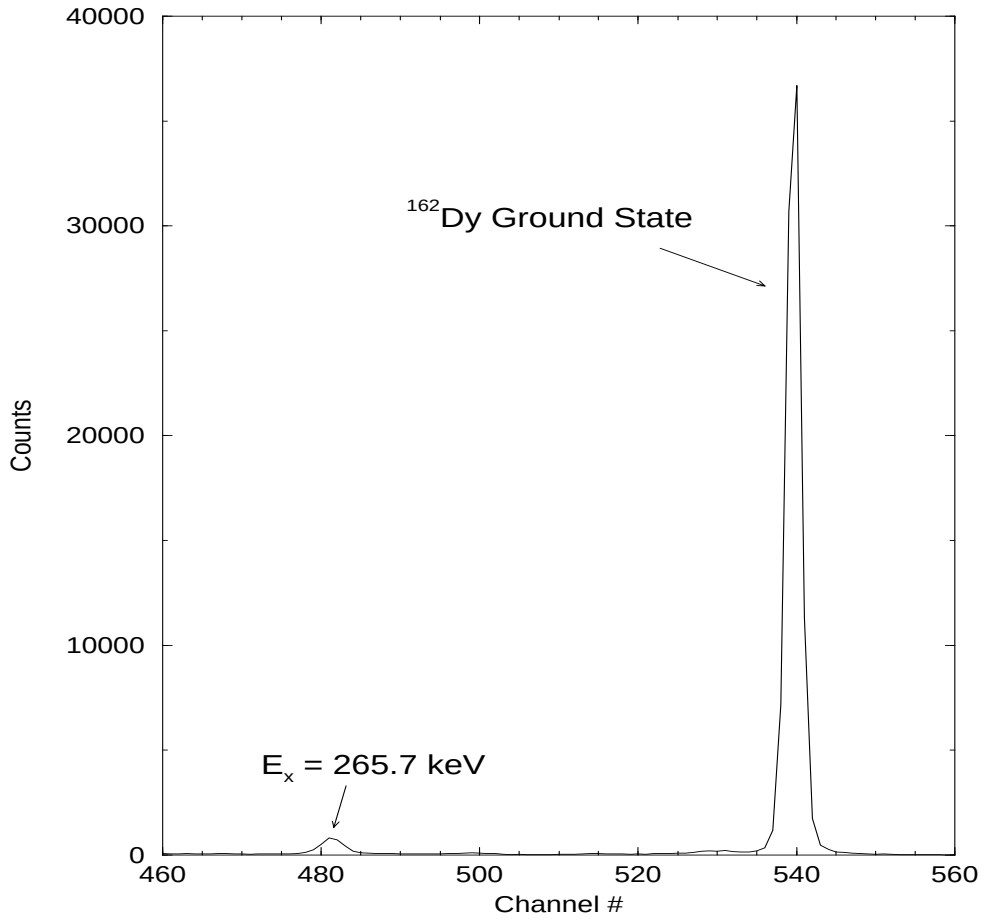

Figure 3.7: Spectrum from ^{162}Dy(p,p) at 10° with $E_p = 12$ MeV. The resolution obtained during this run was 0.91 mm or 9.6 keV.

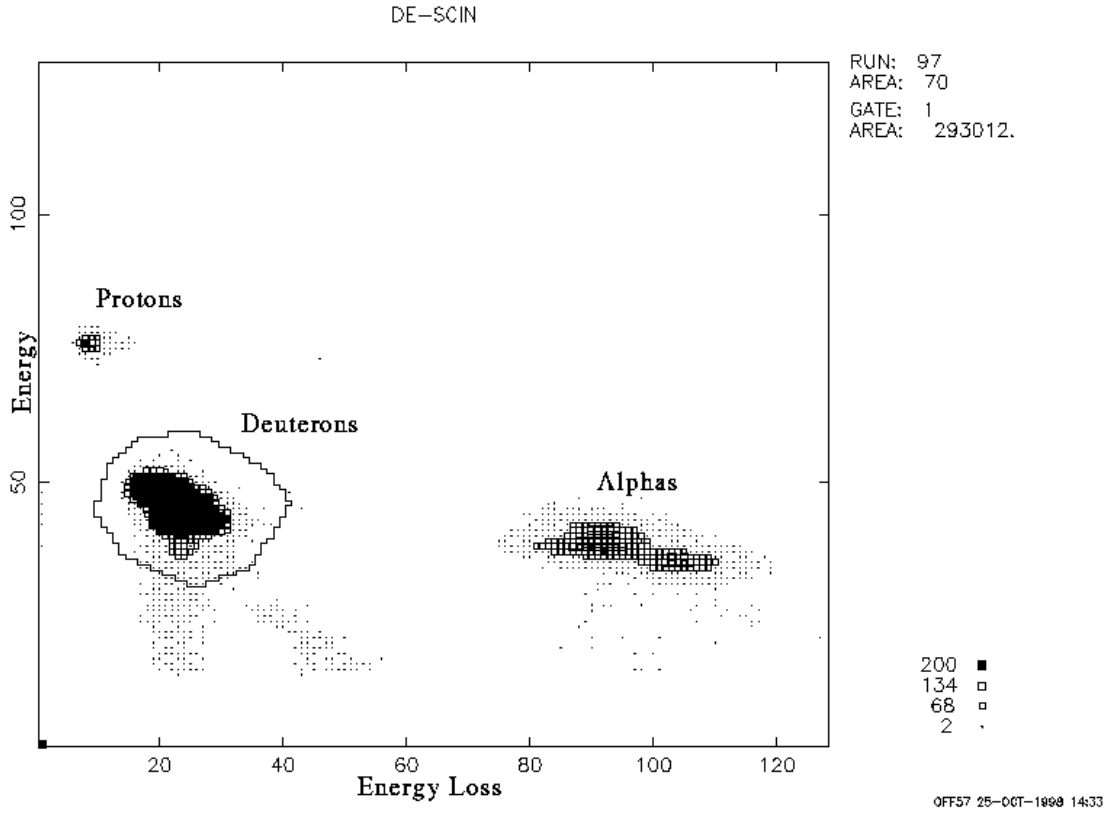

Figure 3.8: Example of ΔE-E separation of particles with the Enge detector. The spectrum shown is from a March 1997 run of ^{27}Al(^{3}He, d)^{28}Si.

An example of the particle ID that can be obtained is shown in Figure 3.8 for 20-MeV ^{3}He on an ^{27}Al target. With adjustment of the gains on the ΔE and Scintillator amplifiers, a wide variety of particles can be placed inside the spectrum for further analysis offline. This was useful in obtaining both (^{3}He, d) and (^{3}He,^{3}He) data from the ^{22}Ne and ^{23}Na targets.

Finally, to show the improved resolution of the new detector over the old, Figure 3.9 shows a spectrum of the ^{22}Ne(^{3}He, d)^{23}Na reaction, as taken in September 1997, compared to that of the original silicon detector. The states are labelled by the energy level in ^{23}Na or the final state formed from the contaminants in the target, ^{12}C and ^{16}O. The resolution of the new detector with this experiment is $\approx$ 20 keV. For a target thickness on the order of 40 $\frac{\mu g}{cm^2}$ of carbon and 3 $\frac{\mu g}{cm^2}$ of ^{22}Ne, the ^{3}He beam can lose roughly 10 keV while passing through the target.

The (^{3}He, d) data collections runs were more susceptible to beam optics instabilities because of the longer duration required for the necessary statistics on the weaker states, and horizontal instabilities in the beam were observed during these runs. Thus the contribution of beam effects and the inherent detector resolution appear to be on the order of 9-10 keV.

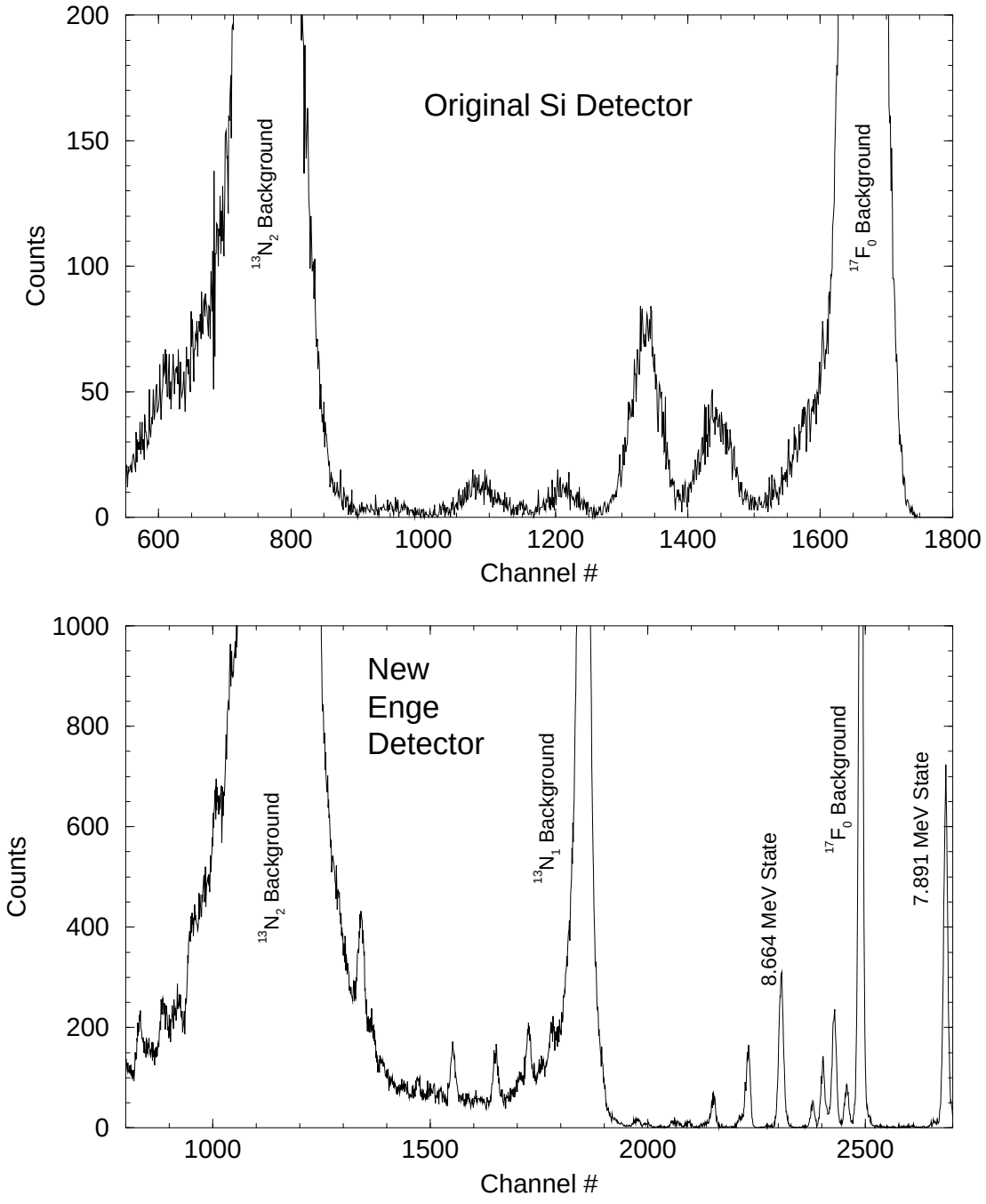

Figure 3.9: A comparison of spectra showing the improved resolution of the new Enge detector. Both spectra are from the reaction ^{22}Ne(^{3}He, d)^{23}Na at 10° and with a beam energy of 20 MeV.

Chapter 4

Targets and Experiments

4.1 Target Fabrication

Detector testing and debugging took place throughout 1996 using a self-supporting ^{27}Al target made by A. E. Champagne and a ^{22}Ne implanted target made by M. S. Smith [Smi90]. Once the detector's behavior was adequate to find distinctive ^{22}Ne(^{3}He, d)^{23}Na peaks it was determined that the neon target did not contain enough material for a reasonable data collection rate. A variety of ^{23}Na targets were made throughout the testing period to find a combination that provided both target stability and lack of contaminants in the region of interest of the deuteron spectrum.

4.1.1 Neon Targets

New implanted neon targets were made in June and August of 1997, using the UNC Department of Physics & Astronomy ion implanter. Natural neon gas (9.22% ^{22}Ne) was obtained and attached to the gas input of the implanter. The system consists of a duoplasmatron source with a 20 kV extraction electrode outside of the plasma forming region, followed by a 90° bending magnet to mass analyze the beam. This entire section can be biased up to 180 kV, providing singly-charged ions from 20 keV to 200 keV. At the beginning of each implan-

AMU Readout	Magnet Current (A)	Beam Intensity (μA)	Beam ID
12.0	15.1	0.23	^{12}C
14.0	16.4	4.5	^{14}N
16.0	17.4	0.85	^{16}O
18.0	18.5	0.11	
19.5	19.5	34.6	^{20}Ne
22.0	20.5	4.36	^{22}Ne
26.0	22.4	0.10	
26.0	22.8	0.40	
27.0	23.2	6.0	$^{14}N_2$

Table 4.1: Beam currents at various bending magnet currents from the August 1997 ^{22}Ne implantation. The AMU readout was recorded for each maximum beam. The expected $^{14}N_2$ beam was seen at a reading of 27 amu.

tation session, the magnet current was scanned over a large range to determine the different components of the ion beam. The beam current was read off a MgO phosphor which was observed while the beam was tuned to obtain the most circular beam spot with the highest current. Both the magnet current and an atomic mass scale are available on the implanter. A different record was made for each maximized beam value of the current, regardless of the atomic mass scale which was used only for relative locations. This can be seen in the observation of the $^{14}N_2$ beam at an AMU readout of 27, instead of the expected value of 28. The beam intensity was recorded after scanning up over the maximum value, down to zero, and then back to the maximum. The results of a scan from the August implantation session are shown in Table 4.1. No beam was observed on either side of the magnet current setting associated with ^{22}Ne. The magnet current was then set for the maximum beam on target. Once beam was maximized on target using the steering and focussing elements, the implanter's beam rastering system was turned on in order to scan the beam across the target to provide uniform implantation.

Following the procedure of Smith [Smi90], 40 $\frac{\mu g}{cm^2}$ carbon foils were floated onto square aluminum target frames (2.35 cm on a side) over a 0.95-cm diameter hole centered on the frame. To prevent the foils from breaking, caused by thermal damage produced by the incident beam, a camera flash unit held about 7 cm from the foil was used to slacken the foils before starting the implantation. This resulted in a pebbled appearance on the foil and allowed the foil to contract while being bombarded with the beam without breaking free of the frame.

A schematic of the target end station is shown in Figure 4.1. Beam from the implanter passed through a copper collimator and then through a copper tube cooled to LN_2 temperature (to prevent contaminants from building up on the target) and biased to -90 V for electron suppression. The diameter of the upstream Cu collimator was slightly smaller than that of the copper tube to minimize the amount of beam hitting the tube. The copper tube extended to within approximately 2 cm of the target holder. A graphite collimator with a defining aperture of 1.27 cm was placed directly over the target frame. This was done so that carbon would be the only material sputtered onto the foil from the beam hitting the collimator. Carbon sputtered onto the target foil could increase the lifetime of the foil during the implantation process [Fif90]. Beam current was read off the electrically insulated endpiece. The back end of the target holder contained a plexiglass viewport to allow visual inspection of the back of the target throughout the implantation. During the June implantation, a diffusion pump was located close to the target end station. This was removed for the August implantation to avoid contamination of the targets by oil.

In order to maximize the amount of neon in the targets, the energy of the beam was varied to implant to different depths in the foil. Amorphous carbon has a density of 1.8−2.1 g cm^{-3}, and so the thickness of the foils was approximately 2000 Å. TRIM [Zie92] calculations were performed for various energies of ^{22}Ne beams to determine the projected range and longitudinal straggling of the ions. The results are shown in Table 4.2.

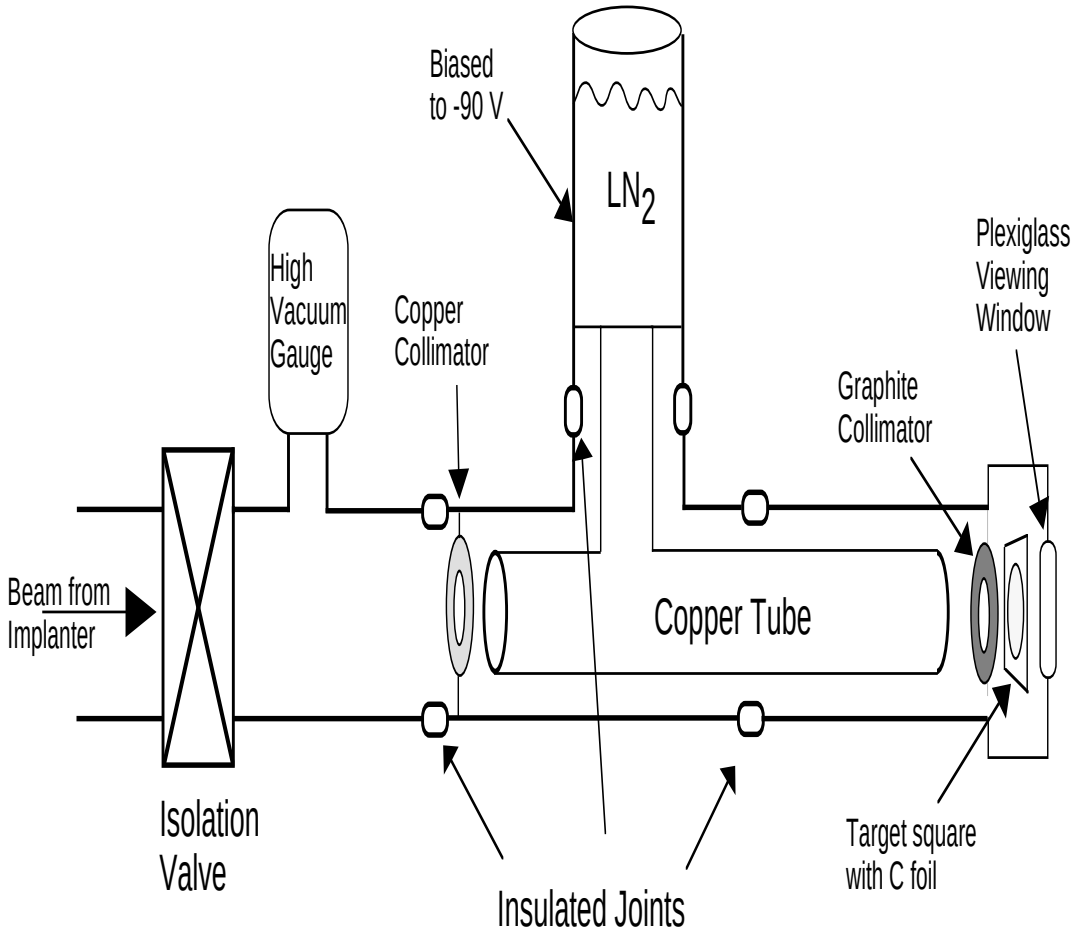

Figure 4.1: Diagram of the end station for implanting neon and sodium into carbon foils.

Ion Energy (keV)	Projected Range (Å)	Longitudinal Straggling (Å)
10	166	54
20	314	92
30	466	127
40	620	159
50	776	189

Table 4.2: ^{22}Ne implantation depths for a variety of energies. The lowest energy of 10 keV is not available at the ion implanter used for producing the targets.

Target Side	Energy (keV)	Target #8 Dose (μA-hr)	Target #12 Dose (μA-hr)	Target #17 Dose (μA-hr)
Front	40	2.4	0.9	2.9
	20	4.0	4.1	3.5
Back	40	2.5	2.6	0.0
	20	3.4	4.4	0.0

Table 4.3: ^{22}Ne implantation doses for 3 completed targets. Target #17 was not exposed on its back side because neon gas was exhausted during the front implantation.

In all, three implanted ^{22}Ne targets were made. The procedure was to implant at 40 and 20 keV on one side of the foil, reverse the direction of the foil, and implant again at these two energies. Based on the energy of the beam, current limits were set to avoid heating the targets too much. Smith found that an optimal power for implanting was 25 $\frac{\mathrm{mW}}{\mathrm{cm}^2}$, which corresponds to 650 nA at 40 keV and 1.3 μA at 20 keV for the size of the beam spot. The final beam current exposures are listed in Table 4.3. Target #12 was made during the June implantation when the diffusion pump was located near the target end station. Possible contamination from silicon is observed in the $(^3\mathrm{He}, d)$ spectra, as shown in Figure 5.4.

For our $(^3\mathrm{He}, d)$ measurements, the neon targets were evaluated for resolution and count rate using several strongly-populated states. The target with the best performance was used for data collection. Three runs were performed to obtain data from neon. In September 1997, and February 1998, target #12 was used. During a calibration run in October 1998, target #8 was used because it was found that #12 had developed several small holes.

Target Material	Method	Results
Na_2WO_4	Evaporation	Too much O in spectrum
NaI	Evaporation	Too much background in monitor detector
Na	Implantation	Unstable in beam
NaF	Evaporation	Too little separation in monitor detector
NaCl	Evaporation	Too little separation in monitor detector
NaBr	Evaporation	Successful
Na + Au	Evaporation	Successful

Table 4.4: Results of tests on various sodium targets.

4.1.2 Sodium Targets

Numerous sodium targets were made and tested before two were selected for data collection. This process took place during detector testing and neon data collection. Table 4.4 shows the results for various targets.

Because of the reaction kinematics, the $^{16}O(^3He, d)^{17}F$ reaction to the ground and 1st excited state (E_x = 495 keV) can obscure the states of interest. This can be minimized, but not completely avoided, by exposing the targets to atmosphere only when transferring them from a dessicator, kept under vacuum, to the target chamber. In the Na_2WO_4 target, the magnitude of the oxygen content was unacceptable.

The NaF, NaCl, and NaI targets caused problems for a target chamber monitor detector either because of peaks too close to the $^{23}Na(^3He,^3 He)^{23}Na$ peak or because of overall background throughout the spectrum.

Implanted sodium targets were made during the August 1997 session of neon implantation using heated NaCl and nitrogen flow gas, and tested in the Septem-

ber 1997 run. The yield in the deuteron and the monitor spectra was found to be highly variable. This was could have been caused by the diffusion of sodium out of the target while under bombardment [Wie97]. Evaporated compounds might provide more stability than implantation because of chemical bonding of the sodium atoms.

The final choice of targets included two different materials. The NaBr target was made by evaporating 3.17 kÅ of material onto 20 $\frac{\mu g}{cm^2}$ carbon foils. The Na + Au target consisted of a layer of sodium metal sandwiched between two thin layers of gold to minimize oxidation. All of this was formed by evaporating each layer successively onto a 20 $\frac{\mu g}{cm^2}$ carbon foil. The final sodium-gold target that was used consisted of 1.6 kÅ of sodium metal between gold layers of 26 and 46 Å thickness.

The deuteron spectra from the Na + Au target were quite clean between peaks, but there was a sizeable amount of ^{16}O in the target resulting in large peaks from the ground and first excited state of ^{17}F. The NaBr target was relatively free of the ^{17}F peaks, but had more background across the full spectrum. Data were collected on the NaBr targets for statistics in the peaks of interest, while the Na + Au target was used to determine if small peaks were being missed in the background. The yield of elastically scattered ^{3}He from the NaBr target was found to drop by approximately 20% over a period of 48 hours of beam on target (20 MeV ^{3}He at $\approx$ 250 nA). This can be seen in Figure 4.8.

4.2 Experimental Set-Up

4.2.1 Beam and Beamline

The ^{3}He beam was produced by the TUNL Helium Source located in the low energy bay. After charge exchange within a sodium vapor canal, $^{3}He^{-}$ was selected with the negative ion source inflection magnet and injected into the

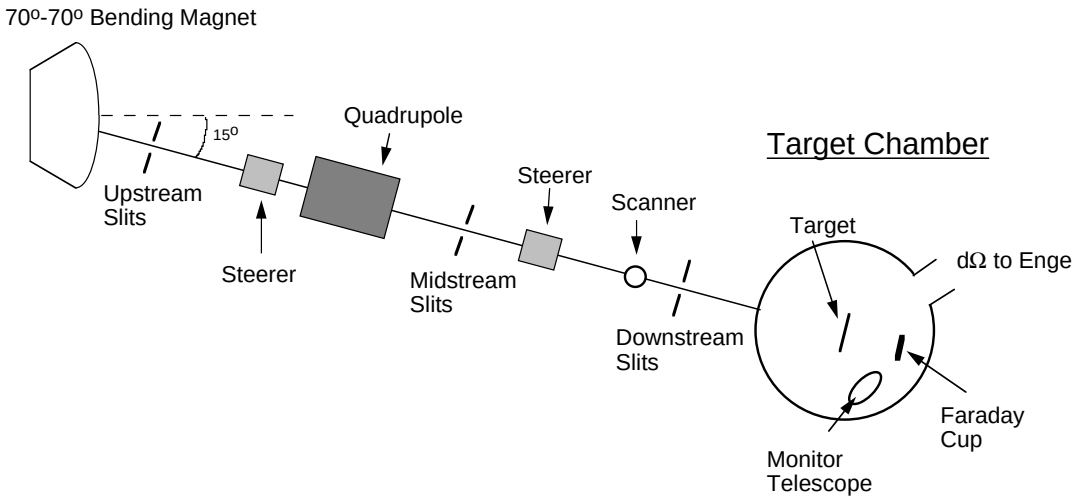

Figure 4.2: Diagram of the Enge spectrometer beamline.

tandem accelerator. The tandem voltage was set at a nominal 6.667 MV, and a 20-MeV beam was produced by stripping the $^3He^-$ ions to $^3He^{+2}$ nuclei in the terminal. The beam was then passed through the $90°-90°$ magnet analyzing system which provides feedback into the tandem voltage stabilizer circuit. The magnetic field in the analyzing system was regulated by NMR at a value of 0.558660 T.

After exiting the second 90° magnet, the beam was steered into the 15° - right leg out of the $70°-70°$ magnet, which is the Enge Spectrometer beamline. Figure 4.2 shows the layout of the beam transport elements along this line up to the target chamber. Three sets of slits along this beamline were used to establish the beam axis. The slits furthest upstream were first set at ± 0.254 cm for tuning purposes and then opened to ± 0.508 cm for data collection. The midstream slits were kept at ± 0.254 cm and the set of slits directly before the target chamber were kept at ± 1.5 mm.

4.2.2 Target Chamber

A ΔE-E silicon telescope was mounted in the target chamber at $\theta_{\rm lab} = 44.2°$ to monitor the targets with elastic ^{3}He scattering throughout the run. The

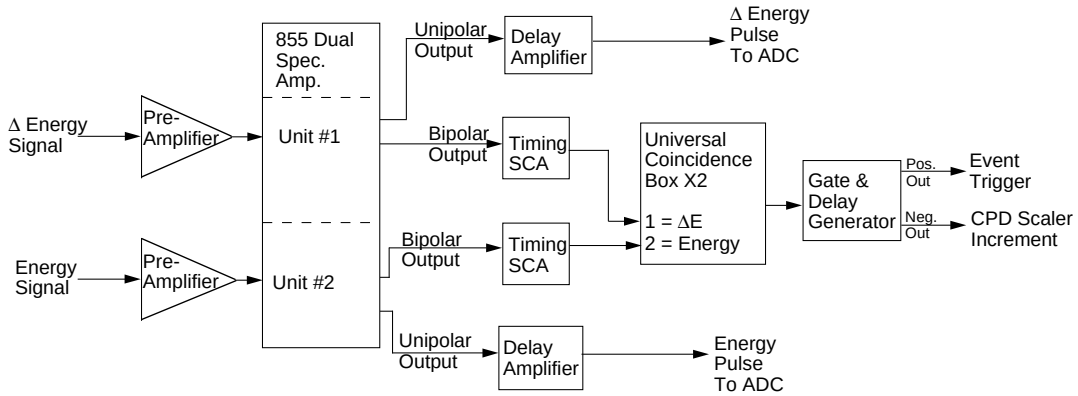

Figure 4.3: Schematic of electronics for the target chamber monitor detector.

measured spectra are also used for normalizing the $(^3\mathrm{He}, d)$ cross sections to the measured elastic scattering. The aperture of the monitor telescope was measured using a calibrated ^{241}Am source and found to be $\mathrm{d}\Omega = 0.92 \pm 0.01$ msr, consistent with a geometric measurement of 0.9 ± 0.1 msr. A schematic of the signal processing electronics is shown in Figure 4.3. Summing of the ΔE and E detector signals was done in software, although a hardware coincidence was required before computer gates were generated. Pulser signals were also sent through the preamps to monitor the dead time and gain match the two amplifiers. Sample ΔE$-$E two-dimensional spectra are shown for the Ne and NaBr targets in Figure 4.4 and Figure 4.5, respectively. The monitor data were stored in event mode so that the particle ID gates could be redrawn offline for analysis of target uniformity and cross-section normalization. The spectra produced by the gates shown in Figures 4.4 and 4.5 are shown in Figures 4.6 and 4.7 below. The results of stability tests for an implanted neon target and an evaporated NaBr target are shown in Figure 4.8. The neon information is from the September 1997 run, when the majority of the neon $(^3\mathrm{He}, d)$ data were taken. The NaBr information is from the October 1998 run, performed for normalization purposes. While the ^{22}Ne target had a uniform thickness from run to run, the ^{23}NaBr target had a slight decrease over the course of the data collection. This was corrected for in the analysis.

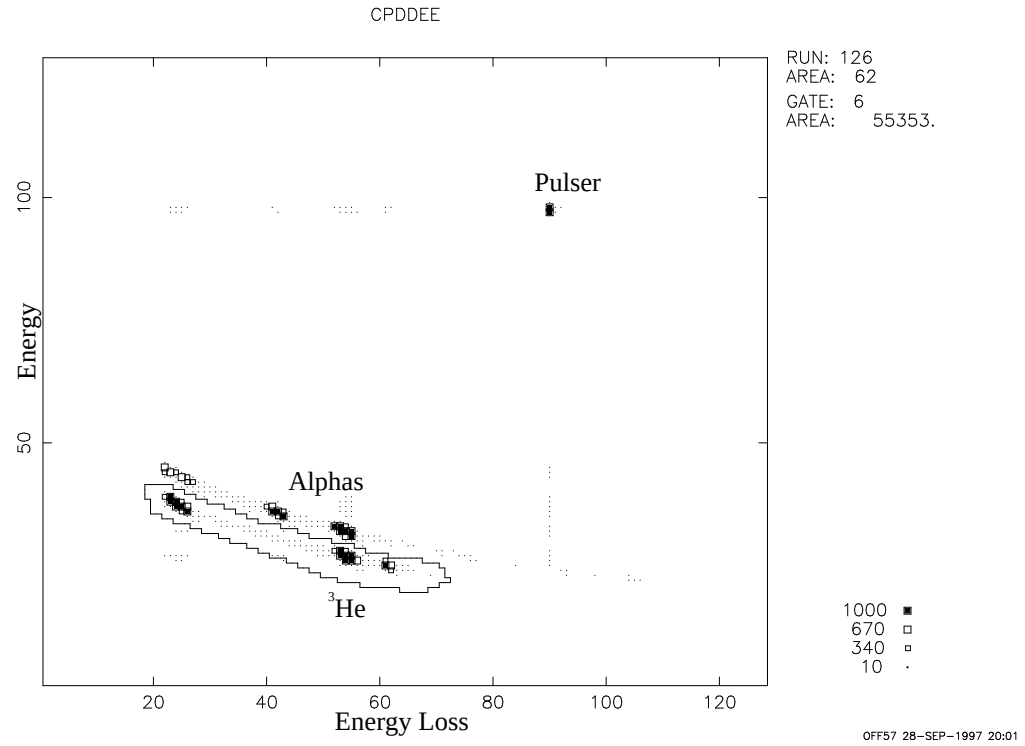

Figure 4.4: Target chamber monitor ΔE-E spectrum from the Ne implanted target.

Beam current was monitored with a tantalum-covered beam stop located in the target chamber. Typical values of beam on target were 200−300 nA. The target chamber pressure was typically 6×10^{-7} torr.

4.2.3 Enge Spectrometer & Detector

Multiple apertures could be loaded into the spectrometer. Data were collected using a 2.0 msr aperture. The pressure in the Enge was typically 5×10^{-6} torr.

The Enge detector was checked prior to each run to ensure that adequate electrical connection existed between each pick-up strip and the corresponding tap on the delay line. The detector was placed in the focal plane box, with the edge of the detector housing in a fixed location on the focal plane table.

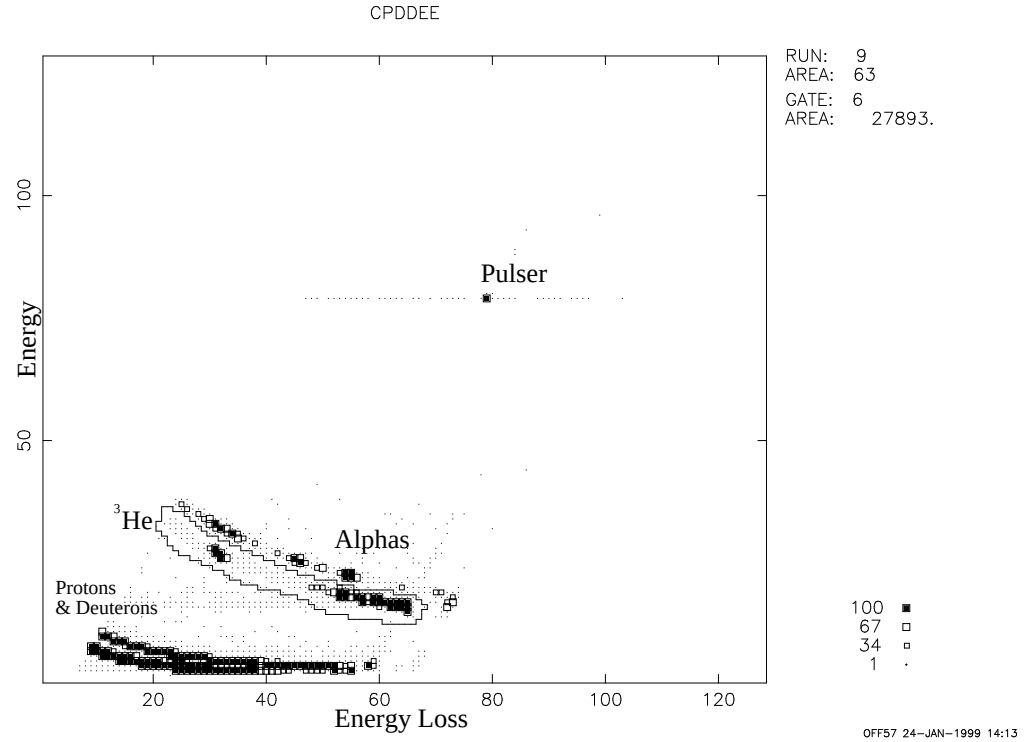

Figure 4.5: Target chamber monitor ΔE-E spectrum from the NaBr evaporated target.

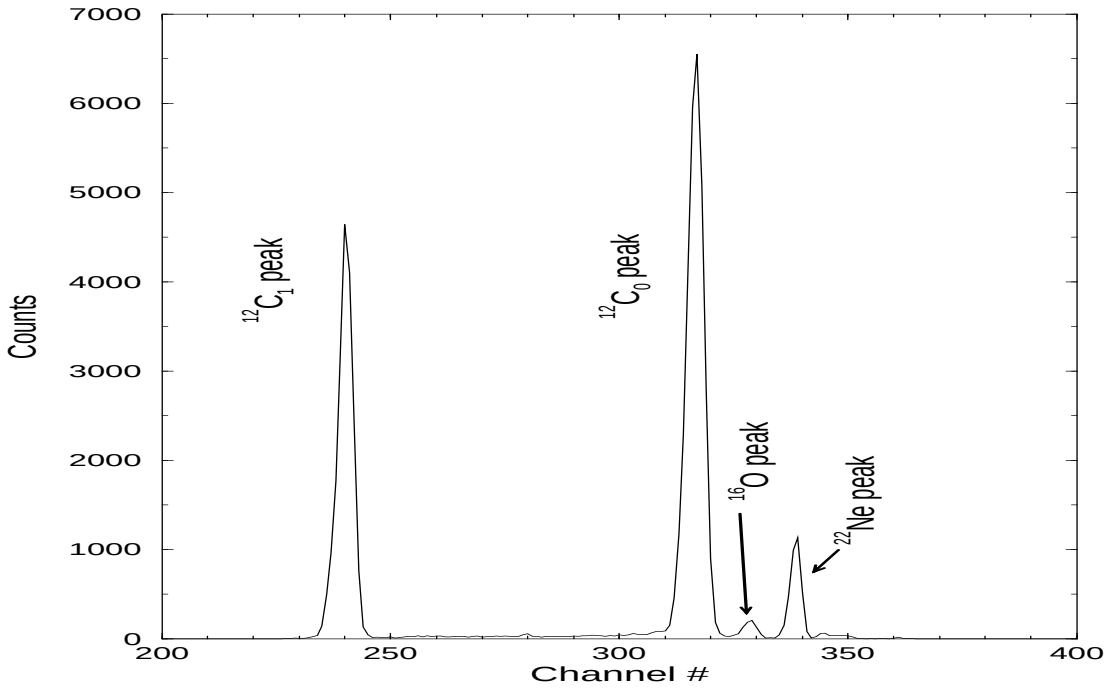

Figure 4.6: Target chamber monitor spectrum for ^{3}He measured with the ^{22}Ne implanted target. Data from September 1997 run.

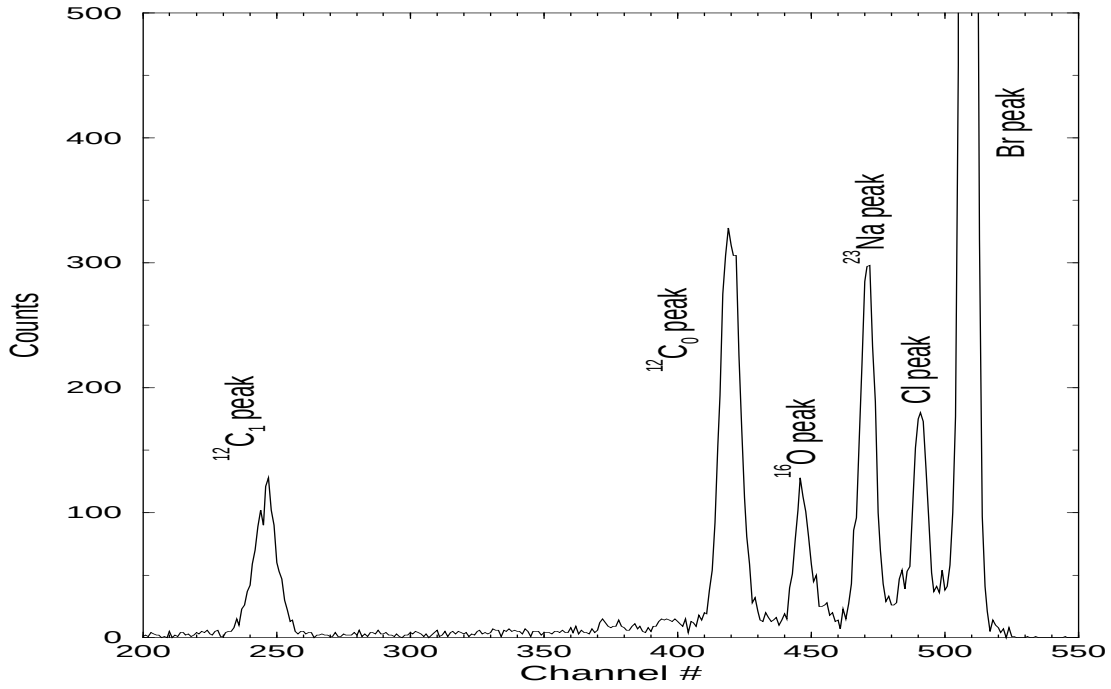

Figure 4.7: Target chamber monitor spectrum for ^{3}He measured with the NaBr evaporated target. Data from October 1998 run.

4.3 Testing of Enge Detector Response

During data collection, the Enge's magnetic field was periodically used to scan the peaks across the front of the detector. This was done to check the efficiency of the detector as a function of channel number, to ensure that individual pick-up strips were not losing electrical contact with the delay line. Generally an aluminum target was used because of the large number of peaks resulting from the ^{27}Al(^{3}He, d)^{28}Si reaction. This allowed a mininum number of field settings to be used to place strong peaks at numerous locations on the detector. A sample efficiency check is shown in Figure 4.9 from the September 1997 run.

A fluctuating response across the detector arises from unequal multiplication on the HV wires in the position sections, which might be caused by insufficient voltage for electron multiplication or by the presence of material with a high electron affinity, such as oxygen. When a large slope was seen in such an efficiency plot, the general solution was to increase the voltage on the position section

and repeat the test. This would usually remedy the situation, as long as care was taken not to produce uncontrolled sparking. The small linear changes in efficiency were corrected for in the analysis. This procedure could not detect individual dead strips on the position measuring board. The full position spectra were monitored to determine if dead regions formed during the course of the experiment.

4.4 Run Summary

In all, three data collection runs were performed. In September 1997, a full angular distribution was taken on the ^{22}Ne implanted target from 5° to 22.5° in 2.5° steps and from 25° to 35° in 5° steps. In February 1998, several runs were taken on ^{22}Ne to gain more statistics at the higher angles. In comparing the September and February neon cross sections at duplicate angles, it was found that the earlier data resulted in yields lower by a factor of approximately 2.5. These changes coincided with a change in the detector fill gas from propane to isobutane. The September cross sections were adjusted upwards by a factor of 2.25 ± 0.05, based on comparison of several peaks at 4 duplicate angles. The measurements were repeated in the October 1998 run and found to be consistent.

During the February run, full angular distributions were taken using the NaBr and Na + Au targets over the same full range of angles as the neon data. A similar angular distribution was taken for the ^{27}Al(^{3}He, d)^{28}Si reaction to study the systematics of the procedure of calibrating the focal plane and extracting cross sections. Both the September and February runs used a Silena ADC for the Enge detector. Unfortunately, this produced a discontinuity approximately halfway across the deuteron spectra, making it difficult to obtain an energy calibration. The ^{23}Na(^{3}He, d)^{24}Mg reaction had a sufficient number of peaks to calibrate the two regions of deuteron energies independently, but this could not be done for the ^{22}Ne(^{3}He, d)^{23}Na spectra.

While analyzing the monitor spectra for the ^{23}Na targets, it was found that the elastic ^{3}He peak from ^{23}Na could not be consistently fitted because of a loss of resolution. The spectra that resulted had no identifiable peaks, with the region of interest consisting of a smeared, featureless structure. The decision was made to keep the existing spectrometer data, and normalize the cross sections relative to a large peak in the deuteron spectra from the ^{24}Mg state at E_x = 8655 keV.

In order to calibrate the neon spectra and to normalize the 8655 keV ^{24}Mg state deuteron peak to the ^{3}He elastic counts, a run was conducted in October 1998 using an Ortec AD811 ADC. Results of the full analysis of the ^{22}Ne and ^{23}Na data will be presented in Chapters 5 and 6.

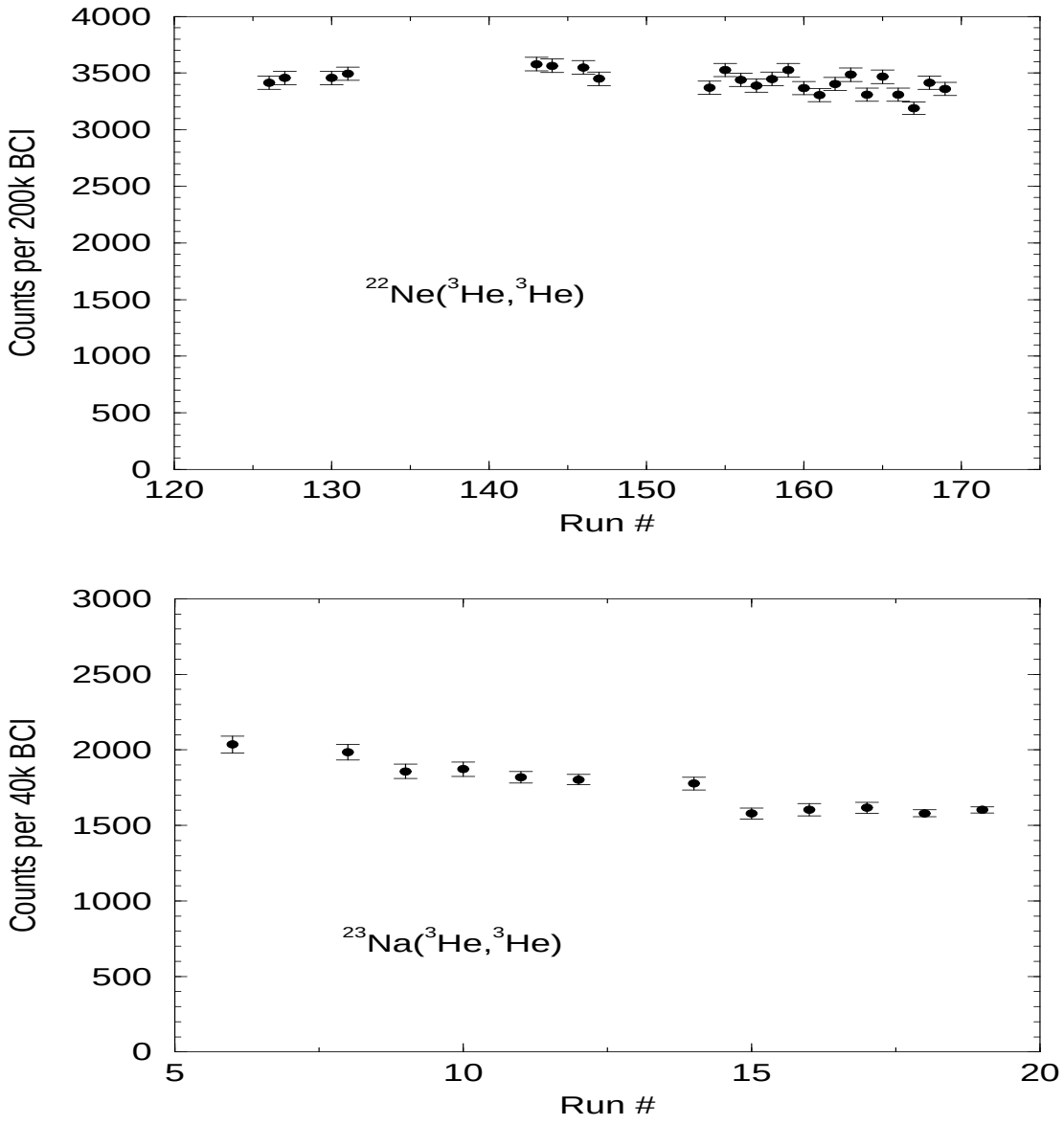

Figure 4.8: A run-by-run test of the yield from the elastic scattering of ^{3}He off of the implanted Ne and evaporated NaBr targets. Corrections have been made for monitor detector dead time.

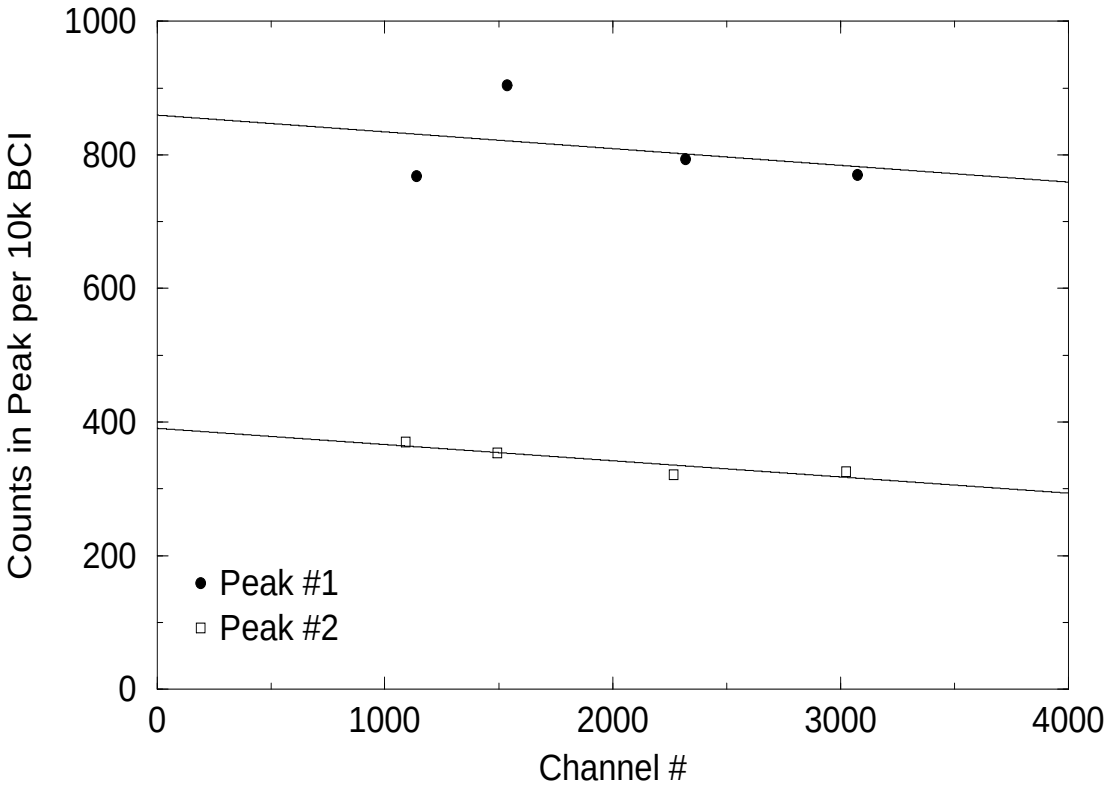

Figure 4.9: Efficiency check of the Enge detector. The peaks from ^{27}Al(^{3}He, d)^{28}Si are scanned across the focal plane detector for a constant amount of beam on target.

Chapter 5

^{22}Ne(^{3}He, d)^{23}Na Analysis

The design of the Enge target chamber allows the spectrometer to take data at angles as low as 3° while still stopping the incident beam on an internal stop. This close geometry prevents accurate measurement of beam current because there is no space for electron suppression equipment around the stop. Thus the cross sections that are measured for comparison to DWBA predictions were normalized to elastic scattering, measured with the spectrometer. The elastic peak measured by the monitor detector was used as the intermediary between the two separate measurements of (^{3}He, d) and (^{3}He,^{3} He).

A typical monitor spectrum is shown in Figure 4.6. The peaks were fit by Gaussians and the areas were corrected for electronic dead time. The details of the deuteron peak fitting are given in Section 5.2.

5.1 ^{3}He Elastic Scattering

In order to normalize the (^{3}He, d) cross sections to elastic scattering, data were taken on ^{22}Ne(^{3}He,^{3} He)^{22}Ne from 15° to 45° in steps of 5°. DWBA analyses of the data were performed using DWUCK4 with ^{22}Ne + ^{3}He optical model parameters obtained from the global parametrization of Becchetti & Greenlees [Bec71]. The data used to determine the global parameterization consisted of ^{3}He elastic scattering off targets with A > 40 and with incident energies < 40 MeV. The ex-

Ref.	V_r	r_r	a_r	W_i	r_i	a_i
[Bec71]	153.1	1.20	0.72	39.10	1.40	0.88
Present	162.2	1.05	0.72	44.89	1.33	0.86

Table 5.1: Optical model parameters of [Bec71] and the results of the parameter search using [Bec71] as the initial starting parameters for ^{22}Ne + ^{3}He elastic scattering. The parameters are as defined in Eq. 2.34. The potential depths are in MeV, while the radii and diffuseness parameters are in fm. The Coulomb radius, as defined in Eq. 2.33, is $r_c = 1.3$ fm.

pressions for the parameters include dependence on ^{3}He energy and target mass and charge. The results are shown in Figure 5.1. The parameters were adjusted to improve the fit to the data by varying each value independently until the best fit was obtained. Several sets of parameters from the compilation by Perey & Perey [Per76] were also tried, with less success than the adjusted global values. This resulted in the parameter set given in Table 5.1. The goodness of fit parameter, Q^2 (described in Section 5.3.1), has the values of 8.3 and 1.1 for the global ^{3}He parameters and the adjusted set of parameters, respectively.

Normalization of the data to the theoretical curve implies a cross section of 8.85 ± 0.24 mb/sr as measured by the monitor detector. The uncertainty cited here reflects only statistical error. The uncertainty that results from the DWBA analysis is evaluated in Section 5.4 along with the $(^{3}\mathrm{He}, d)$ uncertainty.

5.2 Deuteron Spectrum Details

A sample of the deuteron spectrum from $^{22}\mathrm{Ne}(^{3}\mathrm{He}, d)^{23}\mathrm{Na}$ at 10° is shown in Figure 5.2. This shows a range in final excitation energy of ≈ 2 MeV, corresponding to a similar deuteron energy range. The region of astrophysical interest is located roughly in the center, near the 8830-keV state.

For initial peak fitting, a Gaussian shape was combined with a polynomial background which was chosen to reflect the behavior of the counts in the sur-

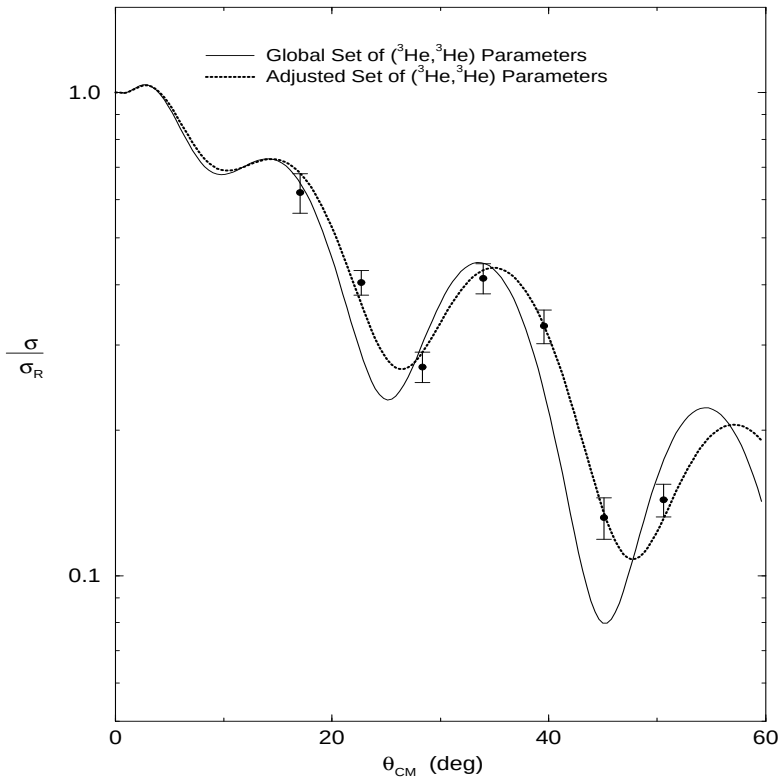

Figure 5.1: Elastic scattering of ^{3}He off ^{22}Ne. The effect of changing the ^{22}Ne + ^{3}He optical model parameters is shown.

rounding channels. The Physics Analysis Workstation (PAW, CERN Application Software Group) program was used for this combination fit. It soon became apparent that isolated peaks showed evidence for a low-channel (low deuteron energy) tail. This has been attributed to the integration time of the signals coming from the front side versus the back side of the high voltage wires in the position-measuring section. The user-defined function option of PAW was used to construct a template for the peak shape, given by a Gaussian on the high- and central-channel portion of the peak, matched to an exponential tail on the low-channel side. The values and the derivatives of the two functions were set equal at a channel number given by $X_{centroid} - 1.4\,\sigma$, where $X_{centroid}$ is the Gaussian mean and σ is the normal Gaussian standard deviation. The value of 1.4 was determined by fitting 3 isolated deuteron peaks in each of the 5°, 10°, and 20° spectra with this template, and then varying the fitting point to minimize

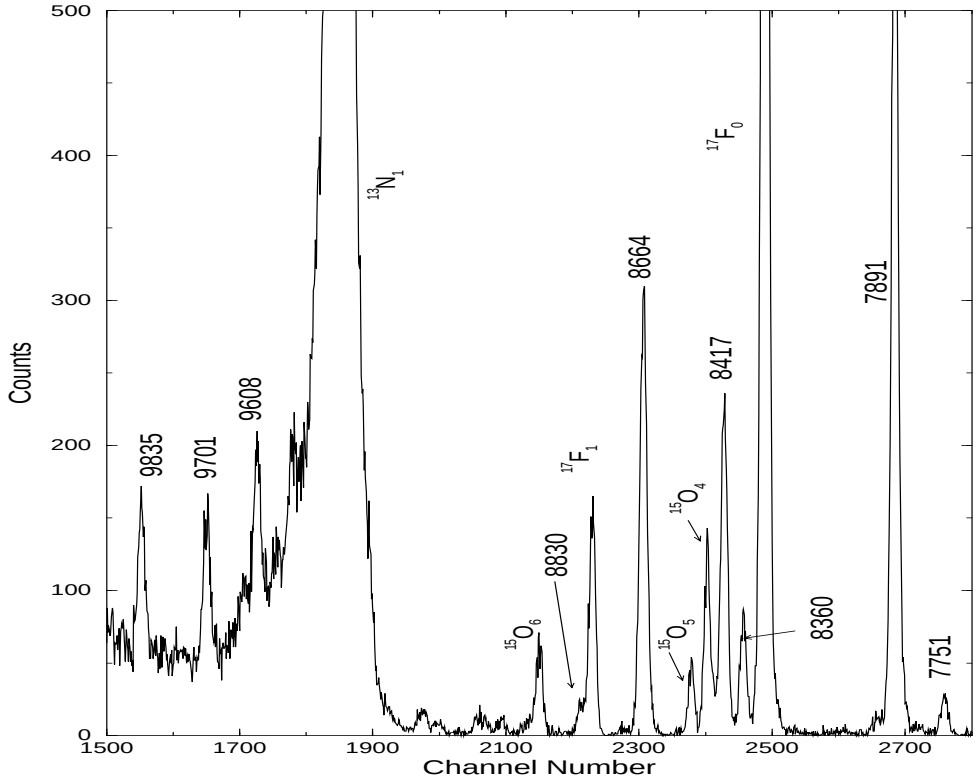

Figure 5.2: Deuteron spectrum from ^{22}Ne(^{3}He, d)^{23}Na at 10°. The peaks are labelled either by their energy in ^{23}Na in keV or by the final state formed from a contaminant in the target.

the χ^2 value reported by PAW. The effect of this shape on the number of counts extracted from a given peak, and a Gaussian peak with the same height N and standard deviation σ, is to change the typical value of $\sqrt{2\pi}\,\mathrm{N}\,\sigma$ to $2.5721\,\mathrm{N}\,\sigma$, a difference of only 2.6%. For peaks located on top of relatively large background, a pure Gaussian shape was found to be equally effective.

Each of the major peaks was fit at all of the angles where they were visible, and counts and centroid values were extracted. Because of the kinematics of the (^{3}He, d) reaction from the different mass nuclei in the target (^{12}C, ^{14}N, ^{16}O, and ^{22}Ne) some of the deuteron peaks from ^{23}Na were obscured by deuterons from contaminants at certain angles.

5.3 Calibration Peaks and Energy Calibration

5.3.1 Identification of Calibration Peaks

A tentative identification of the peaks was made based on comparison with the published spectrum of Powers *et al.* [Pow71] at 15°. With these assigned energies, cross sections were calculated for only six states around the region of interest in order to verify the experimental method. DWUCK4 was run for the appropriate transferred angular momentum, which was derived from the known J^{π} values.

The entrance channel optical model parameters were taken from the results of the (^{3}He,^{3} He) scattering, and given in Table 5.1. The optical model parameters used for the exit channel $^{23}\mathrm{Na} + d$ were taken from the global parametrization of Daehnick *et al.* [Dae80]. The data set used to determine the global expressions covered an energy range of 11.8 to 90 MeV and included a target mass range from ^{27}Al to ^{232}Th. The potential set used here is their 79 DCV L (Table III), for nonrelativisitic kinematics. The parameters depend on deuteron energy, target mass and charge, and include shell corrections. Over the range of deuteron energies appropriate for the states analyzed in this work (between excitation energies of 7751 keV and 9835 keV corresponding to a deuteron energy range of roughly 12500 to 15500 keV) all but one of the parameters were constant. The exception was the volume imaginary strength, which changed from 0.1 MeV to 0.4 MeV, which was too small to have any noticeable effect. An average value of 0.24 MeV was adopted.

The final-state wave function in ^{23}Na was calculated by DWUCK4 using an optical-model potential which contains only a real well depth and a spin-orbit factor of 25 times the Thomas term. The depth of the real potential was varied by the program to match the separation energy of the state in question. The values of the real radius and the real diffuseness were taken from [Ili97], along with the value of the Coulomb radius, $r_c = 1.28$ fm. The optical model parameters for each

Particle	V_r	r_r	a_r	W_i	W_D	$r_i = r_D$	$a_i = a_D$	V_{so}	r_{so}	a_{so}
^{3}He	162.2	1.05	0.72	44.89		1.33	0.86			
d	88.0	1.17	0.73	0.24	35.8	1.33	0.73	13.85	1.07	0.66
p	[a]	1.17	0.69					λ=25		

[a] V varied to match separation energy.

Table 5.2: Optical model parameters used in ^{22}Ne(^{3}He, d)^{23}Na. The parameters are as defined in Eq. 2.34. The potential depths are in MeV while the radii and diffuseness parameters are in fm. The ^{3}He and d Coulomb radii are both 1.3 fm while the p Coulomb radius is 1.28 fm. The ^{3}He parameters are from the fit to the current elastic scattering data. The d parameters are from Daehnick *et al.* [Dae80]. The p parameters are from Iliadis [Ili97].

particle involved in the reaction that were used in analyzing the ^{22}Ne(^{3}He, d)^{23}Na reaction are listed in Table 5.2.

The differential cross sections and DWBA fits are shown in Figure 5.3. The fitting between the experimental cross section and the theoretical cross section was performed using a least-squares fitting program [Ili94]. This program searches for the minimum value of

$$Q^2(\alpha) = \frac{\sum_{i,k}[(e_i - \alpha_k t_{ik})/\delta e_i]^2}{i_{\max} - k_{\max}}. \tag{5.1}$$

The summation index i runs from 1 to the number of angles at which the cross section was measured ($= i_{\max}$), while k numbers the l_p-values that can contribute to the stripping. The experimental cross section is ($e_i \pm \delta e_i$) and the calculated DWBA cross section at angle i for l_p transfer k is t_{ik}. The constants α_k are proportional to the spectroscopic factors. For the ^{22}Ne(^{3}He, d)^{23}Na reaction, the 0^+ nature of the ^{22}Ne ground state limits k to 1, simplifying the procedure. However, for states of unknown or limited J^π values, different l-transfers must be considered.

Because the target nucleus has a $J^\pi = 0^+$, there is no ambiguity between a given spin assignment and the value of the angular momentum transfer. However, for unknown J^π values but identified l-transfer values, two total angular momentum transfers are generally available (the exception is for $l = 0$, correponding to

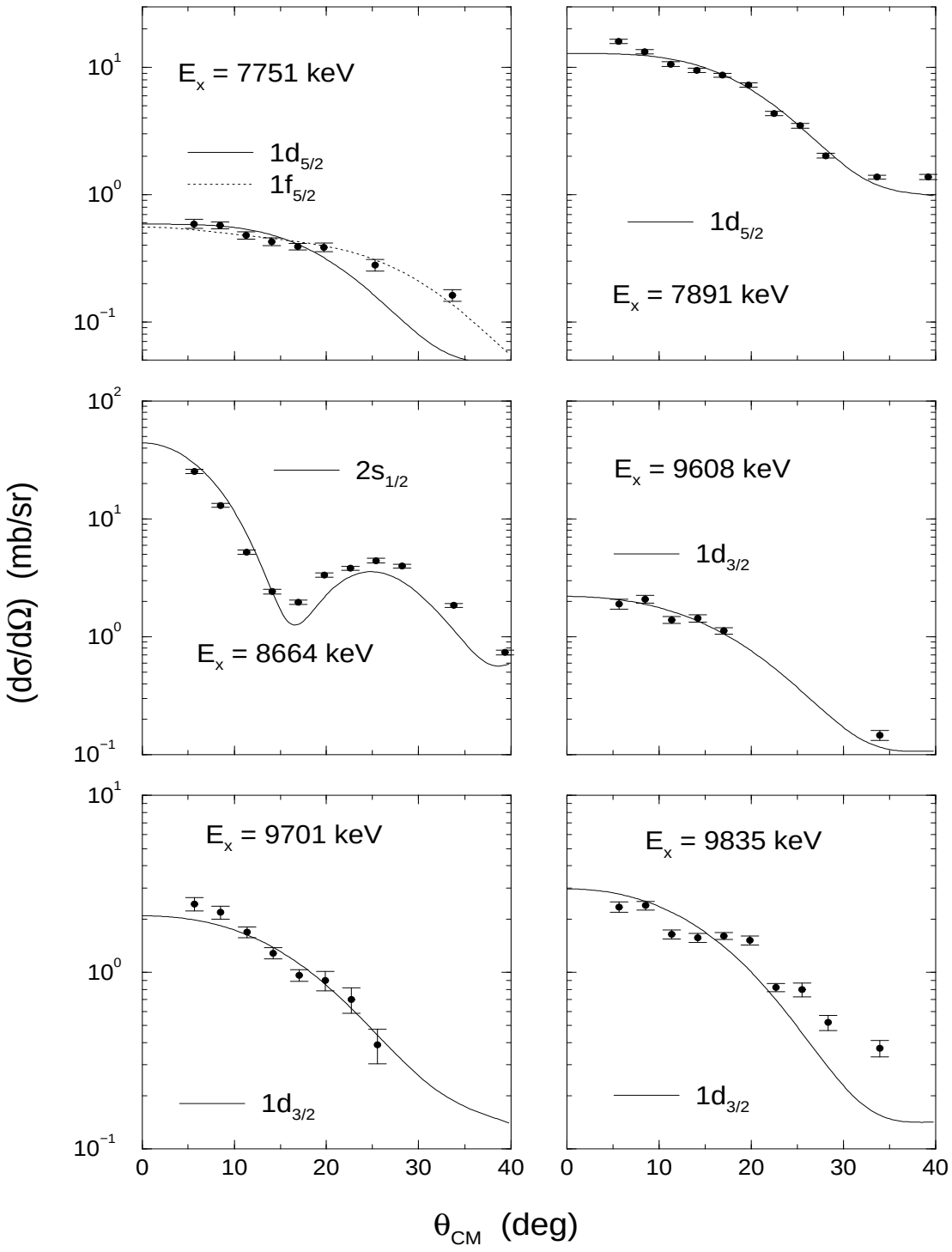

Figure 5.3: Angular distributions and DWBA fits for the calibration states in ^{22}Ne(^{3}He, d)^{23}Na. The angular momentum transfer is noted for each fit. Not all l transfers are shown, for reasons of clarity.

a J^π value of $\frac{1}{2}^+$). The lowest open orbital was assumed for a given l-transfer, so that the transfers calculated and presented are $2s_{\frac{1}{2}}$, $2p_{\frac{3}{2}}$, $1d_{\frac{5}{2}}$, and $1f_{\frac{7}{2}}$. The values of $(2J_f + 1)C^2S$ obtained for these six states are shown in Table 5.3 in comparison with previous measurements. The uncertainty in $(2J_f + 1)C^2S$ is about 27%, for a given spin, based on tests described in detail in Section 5.5.2.

The bound state at 7751 keV was observed by Powers *et al.* with a tentative l_p transfer of 3. This is the best fit value for the present data also, and corresponds to a J^π value of $\frac{5}{2}^-$ or $\frac{7}{2}^-$. It is observed to decay to the $\frac{5}{2}^+$ state at 440 keV and to the $\frac{3}{2}^+$ state at 2982 keV with equal branching ratios of 50% [Bak89]. The same study reports that spins of $\frac{1}{2}$ and $\frac{3}{2}$ are excluded by angular distribution. Thus, they report $J^\pi = \frac{5}{2}^+$ or $\frac{7}{2}^+$, which are presented in [End90a] also. These values correspond to l_p transfers of 2 or 4 respectively for this study. Childs *et al.* report a tentative l_p transfer of 2 from their (d, n) study [Chi73]. The results from the present work, for the fits of all four possible J^π values are reported in Table 5.3.

The two unbound states at 9701 and 9835 keV have been studied by Powers *et al.* [Pow71]. Their analysis treated the states as though they were bound by 10 keV, even though they are unbound by 907 and 1041 keV, respectively.

For the three unbound states, values of $(2J_f + 1)\Gamma_p$ were calculated from the $(2J_f + 1)C^2S$ values and the Γ_{sp} values returned from DWUCK4. They are reported in Table 5.4 along with values determined from $^{22}Ne(p, p)^{22}Ne$ as measured by Keyworth *et al.* [Key68]. They report errors of 50% for Γ_p values for resonances with widths comparable to their beam energy spread of 110 eV (which applies to the three unbound states analyzed and presented here). The values of C^2S derived in the present study reproduce existing results when the states are treated properly (*i.e.* when unbound states are analyzed as such). In the cases where the C^2S values differ from the bound state analysis, the values of Γ_p are consistent with proton-elastic scattering measurements, within a factor of 2, as seen in Table 5.4.

				$(2J_f + 1)C^2S$	
E_x (keV)	J^π	l	Q^2	Present	Previous
7751	$\frac{5}{2}^{+a}$	2	9.8	0.028	0.05[c]
	$\frac{5}{2}^{-b}$	3	1.8	0.076	0.084[d]
	$\frac{7}{2}^{-b}$	3	3.0	0.052	
	$\frac{7}{2}^{+a}$	4	19.4	0.33	
7891	$\frac{5}{2}^{+}$	2	13.3	0.57	0.46[d]
					0.40[c]
8664	$\frac{1}{2}^{+}$	0	24.8	0.59	0.60±0.08[e]
					0.54[d]
					0.50[c]
9608	$\frac{3}{2}^{+}$	2	3.1	0.082	
9701	$\frac{3}{2}^{+}$	2	1.6	0.084	(0.27)[d,f]
9835	$\frac{3}{2}^{+}$	2	18.5	0.11	(0.20)[d,f]

[a] J^π value from [End90a].

[b] J^π value from l-transfer of present data and [Pow71].

[c] (d, n) from [Chi73].

[d] $(^3\mathrm{He}, d)$ from [Pow71].

[e] Direct capture (p, γ) from [Gör83].

[f] Used slightly bound state.

Table 5.3: $(2J_f + 1)C^2S$ values for calibration states in $^{22}\mathrm{Ne}(^3\mathrm{He}, d)^{23}\mathrm{Na}$. Energies and J^π values are taken from [End90a], with the exception of the 7751-keV state, which is discussed in the text.

			$(2J_f + 1)\Gamma_p$ (eV)	
E_x (keV)	J^π	l	Present	Previous[Key68]
9608	$\frac{3}{2}^{+}$	2	44	24
9701	$\frac{3}{2}^{+}$	2	87	116
9835	$\frac{3}{2}^{+}$	2	247	188

Table 5.4: $(2J_f + 1)\Gamma_p$ values for calibration states in $^{22}\mathrm{Ne}(^3\mathrm{He}, d)^{23}\mathrm{Na}$, compared to (p, p) data from Keyworth *et al.* Errors quoted in that work are 50% for resonances of these thin widths (compared to the beam spread of 110 eV).

5.3.2 Energy Calibration

To extract energy values for the states in the astrophysical region of interest and to locate the positions of the possible states at 8862 and 8894 keV, the deuteron spectra need to be calibrated, either in terms of deuteron energy or final excitation energy. The focal plane of the Enge spectrometer is usually calibrated with a 3rd-order polynomial in energy. This has been verified by a brief analysis of the ^{27}Al(^{3}He, d)^{28}Si data collected in February 1998. The method uses the peak centroids returned by PAW and the excitation energies from Endt [End90a]. For the ^{27}Al analysis, the peak identification was obtained by comparing our spectra to those of Nann [Nan92] and Champagne *et al.* [Cha86]. After fitting the (Centroid, E_x) data with a 3rd-order polynomial, the error in the fit was determined by predicting the energies of the calibration states and several well-known states not used in the calibration. The average difference was determined and is shown in Table 5.5.

θ_{lab}	# of Calibration Peaks	# of Predicted Peaks	$\langle\sigma\rangle$
5°	15	8	2.8 keV
15°	12	7	2.0 keV

Table 5.5: Calibration results from ^{27}Al(^{3}He, d)^{28}Si.

Using the six identified calibration states in ^{23}Na, the calibration of the ^{22}Ne(^{3}He, d)^{23}Na spectra resulted in large errors ($>$ 20 keV) in the predicted energies of non-calibration peaks, because of the non-linearity of the Silena ADC used. In order to more accurately predict energies on the focal plane, a calibration from ^{27}Al(^{3}He, d)^{28}Si spectra was applied to the ^{22}Ne(^{3}He, d)^{23}Na data. There were only a few angles at which this was possible, because of a limited amount of overlap between the different data sets. An ^{27}Al run is required at the same angle as the ^{22}Ne run during the same week-long data collection run. Thus, the only difference in the position of deuterons with the same energy on the focal plane would be a slightly different field in the spectrometer. The ratio

of the magnetic fields used in collecting the ^{22}Ne and the ^{27}Al data was typically within 1% of unity.

The only difference in the physical situation for two deuterons, 1 and 2, of the same energy but from the different reactions, 1 and 2, is the magnetic field of the spectrometer. The radii of curvature, ρ_i, are related by

$$\rho_2 = \left(\frac{\mathrm{B}_1}{\mathrm{B}_2}\right) \rho_1, \tag{5.2}$$

where B_1 and B_2 are the magnetic fields associated with the respective targets. The radius of curvature through the Enge can be related to the position on the focal plane, x, by the formula

$$\rho = \mathrm{A} + \mathrm{C}\,\mathrm{x}, \tag{5.3}$$

where A and C are constants from the geometry of the focal plane chassis in relation to the spectrometer. The channel number of a given peak depends on the location of the detector on the focal plane chassis, which can be related to the position on the focal plane, x, by

$$\mathrm{x} = \mathrm{D} + \mathrm{E}\,(\text{channel \#}). \tag{5.4}$$

Here the constants D and E depend on the location of the detector on the focal plane chassis and the location of the position measuring boards inside the detector. Thus, the centroid of the two deuterons of the same energy from the ^{27}Al(^{3}He, d)^{28}Si reaction and the ^{22}Ne(^{3}He, d)^{23}Na reaction are related by combining Equations 5.2, 5.3, and 5.4 to obtain

$$\text{Neon Channel \#} = \mathrm{G} + \frac{\mathrm{B}_{\mathrm{Al}}}{\mathrm{B}_{\mathrm{Ne}}}\,(\text{Aluminum Channel \#}), \tag{5.5}$$

where G is a constant that is determined by normalizing the relationship to a specific deuteron peak.

This calibration method was tested using 5° data from the two reactions ^{23}Na(^{3}He, d)^{24}Mg and ^{27}Al(^{3}He, d)^{28}Si. The calibration from the ^{27}Al target was

applied to the ^{23}Na data, and then compared with the internal calibration of the ^{23}Na data using identified peaks. Because of the nature of the focal plane calibration, peaks further away from the normalization peak will experience increasing errors in predicted deuteron (and excitation) energies. The method was therefore limited to peaks within ± 1 MeV of the calibration peak chosen. In the ^{23}Na-^{27}Al test, the 10917-keV state in ^{24}Mg was chosen for the normalization peak, with a deuteron energy of 15053 keV at 5°. There were a total of 6 clearly identifiable peaks within ± 1 MeV of this state. The standard deviation in the error of the predicted deuteron energy for these states was $\langle\sigma\rangle$ = 4.0 keV. The error in deuteron predicted energy using the internal-peaks calibration method on the ^{23}Na data was $\langle\sigma\rangle$ = 2.5 keV. For the ^{22}Ne data, an uncertainty of 4.0 keV will be assigned to each deuteron energy determination.

There were a limited number of angles in each data collection run that had overlapping ^{22}Ne and ^{27}Al target data. Appropriate spectra were taken at 5°, 10°, 20°, and 22.5° during the three data collection runs. Once the energies of the peaks of interest were determined at these angles, they were used as calibration points in the remaining spectra.

5.4 Analysis of States Below E_{cm} = 460 keV

Six states between the (p,γ) threshold and E_{cm} = 460 keV in the ^{22}Ne + p system were clearly observed at several angles and analyzed in detail. Their analysis is discussed in Section 5.4.1. The tentative states at 8862 and 8894 keV were not observed. There were only a few angles at which upper limits on the peak counts, and thus the cross sections, could be obtained. The resulting analysis is discussed in Section 5.4.2.

5.4.1 Observed States

Figure 5.4 shows the region between (p, γ) threshold and $E_{cm} = 460$ keV for $^{22}Ne(p, \gamma)$ at 5° in the $(^3He, d)$ spectrum. The energy labels reflect the values adopted in this study and discussed below. Only six states in the energy level diagram of Figure 2.2 were observed in the deuteron spectra. Where possible, the deuteron peaks were fit, and counts and centroids were extracted. Sample fits are shown in Figure 5.5. The background peaks from the ^{14}N and ^{16}O nuclei in the target are seen to be a problem. The regions around the peaks were plotted on a shifted horizontal scale in order to make background estimation easier. The

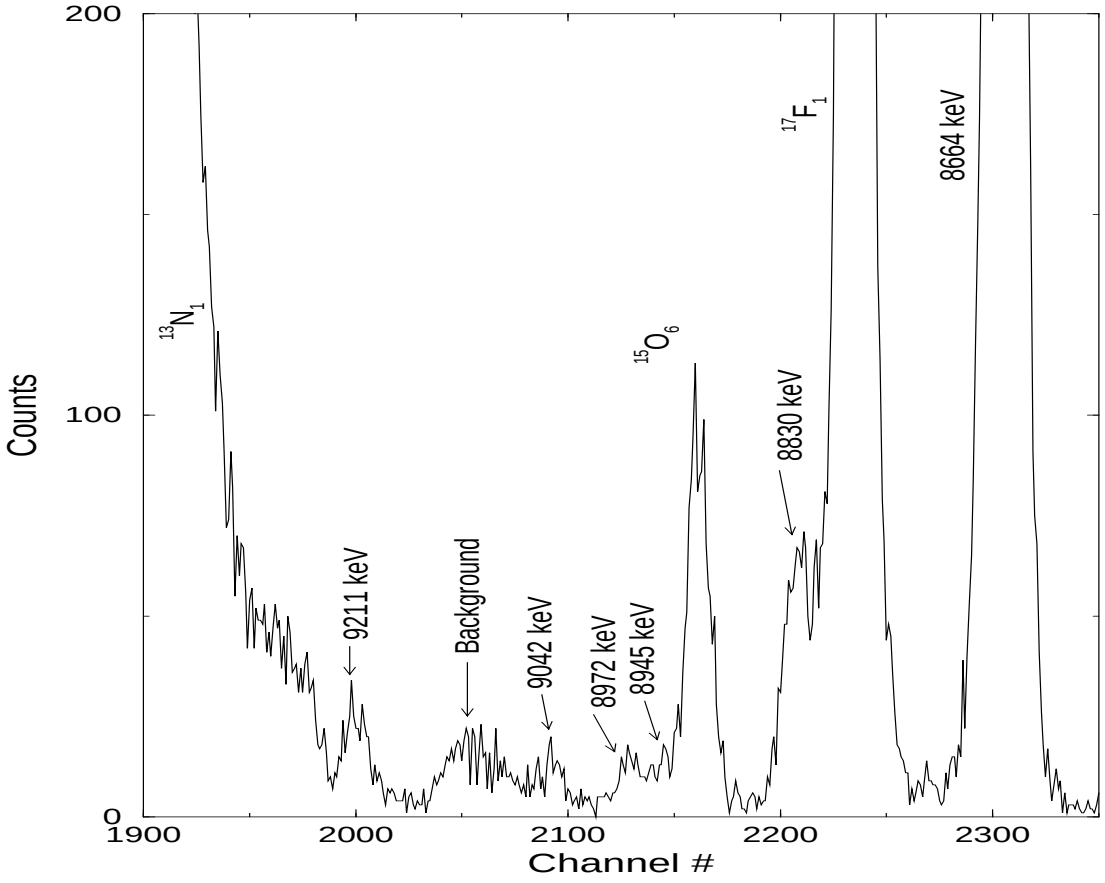

Figure 5.4: Region of interest for $^{22}Ne(p, \gamma)^{23}Na$ at 5° in the $(^3He, d)$ spectrum. Peaks are labelled by their excitation energy in the ^{23}Na nucleus, or by the final state created from a contaminant in the target. The peak labelled Background is most likely due to ^{28}Si in the target from a diffusion pump near the target-making facility described in Section 4.1.1.

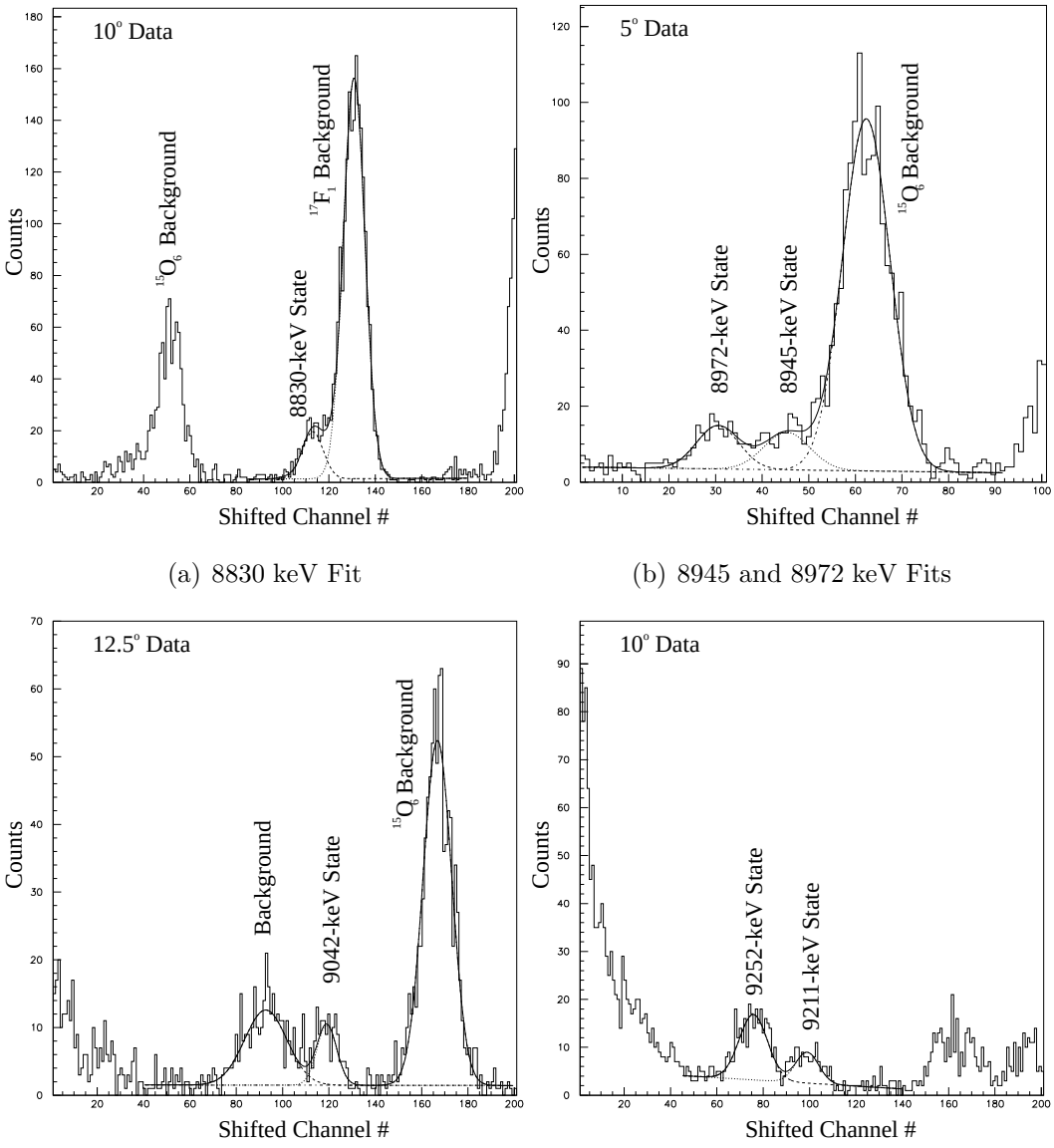

(a) 8830 keV Fit

(b) 8945 and 8972 keV Fits

(c) 9042 keV Fit

(d) 9211 and 9252 keV Fits

Figure 5.5: Sample fits from deuteron peaks in ^{22}Ne(^{3}He, d)^{23}Na. The spectra have been shifted to smaller channel regions in order to ease the background estimation for the fitting process. Energy labels reflect the current adopted values as listed in Table 5.7.

E_x (keV) Present	E_x (keV) [End90a]
8830 ± 3	8829.5 ± 0.7
8946 ± 3	8945 ± 3
8973 ± 3	8972 ± 3
9044 ± 3	9041 ± 2
9215 ± 3	9211.3 ± 0.8
9257 ± 3	9252.6 ± 0.8

Table 5.6: Measured energies for $^{22}\mathrm{Ne} + p$ resonances compared to the latest compilation [End90a].

resulting centroids were converted to full spectrum channels and then used in the calibration equations to determine deuteron energies. The 8830-keV state was obscured by the deuterons from the first-excited state of ^{17}F at 12.5°, 15°, and 17.5°. In order to obtain information from the overlapping peaks, the number of $^{17}\mathrm{F}_1$ deuterons was determined by scaling from the number of $^{17}\mathrm{F}_0$ deuterons. The ratio between the two states in ^{17}F was determined from data taken on $^{16}\mathrm{O}(^3\mathrm{He}, d)^{17}\mathrm{F}$ as provided by A. E. Champagne [Cha97]. With this procedure we were able to extract cross sections for the 8830-keV peak at 12.5° and 15°. However, the 17.5° data were too badly obscured for a reliable estimate to be made.

The 8664-keV state in ^{23}Na was used as the normalization peak for applying the ^{27}Al calibrations. The program RKIN was used to predict deuteron energies. Although RKIN does not use the most currect mass values (Audi & Wapstra 1995 [Aud95]), measuring the deuteron energies relative to the deuterons from the 8664-keV state removes the problem. This was checked using a kinematics code, utilizing the 1995 mass values, provided by A. E. Champagne [Cha98]. An average of the excitation energies gives the results shown in Table 5.6. They are compared to latest compilation of values [End90a] and are in agreement.

E_x (keV)	E_{cm} (keV)	E_{lab} (keV)	J^π
8829.5 ± 0.7	35.4	37.0	$\frac{1}{2}^+$
8945 ± 2	151	158	$\frac{7}{2}^-$
8972 ± 2	178	186	?
9042 ± 1	248	259	?
9211.3 ± 0.9	417.2	436.2	$(\frac{1}{2}^+, \frac{3}{2}^-)^a$
9252.1 ± 0.9	458.0	478.8	$\frac{1}{2}^+$

[a] $\frac{1}{2}^+$ from the present study, $\frac{3}{2}^-$ from [End90a].

Table 5.7: Adopted excitation energies for $^{22}Ne + p$ resonances observed in this work. The values consist of a weighted average of previous data, adjusted for any changes in masses [Aud95], and the present results.

The energies adopted in this study, for the states that are presently observed, are shown in Table 5.7. They are determined from a weighted average of all previous data, corrected for any changes in masses [Aud95], and the current results. The center-of-mass energies and lab energies quoted are for the new Q-value mentioned in Section 2.3.1 (Q = 8794.1 ± 0.3 keV).

The angular distributions for these states were analyzed using DWUCK4 with the optical model parameters given in Table 5.2. The resulting fits are shown in Figure 5.6. In the event of an unknown J^π value for a state, multiple l-transfers were tried.

The 8972-keV state was observed by Powers *et al.*, with an l-transfer of 2 or 3. With the limited data available in this study, these values were both tested. The 9042-keV state does not have a known J^π value, so DWUCK4 was run for the three lowest l-transfer values. The best fit was for a $1d_{\frac{5}{2}}$ transfer, though with the limited data available none of the fits were very bad. Several studies of the $^{12}C(^{12}C, p\gamma)^{23}Na$ reaction show evidence that the state is a high-spin ($J^\pi \geq \frac{11}{2}^+$) member of the $K^\pi = \frac{3}{2}^+$ ground state rotational band of ^{23}Na [Gre75, Bac76, KeK77]. The 9211.3-keV state is reported by Endt [End90a] to be $\frac{3}{2}^-$, though it is favored here to be $\frac{1}{2}^+$. The $\frac{3}{2}^-$ assignment is based on an upper limit of $J \leq \frac{5}{2}$

from the ^{22}Ne(p,γ) experiment of Meyer *et al.* [Mey73] and a value of $l_p^- = 1$ from the ^{24}Mg$(d,^3\,\mathrm{He})^{23}$Na experiment of Krämer *et al.* [Kra71].

Values of $(2\mathrm{J_f}\,+\,1)\mathrm{C^2S}$ and $(2\mathrm{J_f}\,+\,1)\Gamma_\mathrm{p}$ along with the resulting $\omega\gamma$ values and related uncertainties will be discussed in Section 5.5

5.4.2 Upper Limits on the 8862- and 8894-keV States

With no definite evidence for the 8862- and 8894-keV states, a method to find the number of counts in the appropriate region of the spectrum was required. The locations of the peaks were determined at each angle and it was found that the 8862-keV state location was clear of background peaks at 10° and 12.5° while the 8894-keV state location was clear at 10°, 12.5° and 15°. The region of interest at 10° is shown in Figure 5.7.

In order to obtain the number of counts in each peak, maximum likelihood estimation (MLE) with Poisson statistics for both the peak and the background was performed with a program provided by M. D. Hannam and W. J. Thompson [Han99]. If the mean number of counts in a channel is μ, then the probability of observing c counts in that channel is given by [Bev92]

$$P_{Poisson}(c;\mu) = \frac{\mu^c}{c!}\,e^{-\mu}. \tag{5.6}$$

For a range of channels from 1 to N, the likelihood L is given by

$$L = \prod_{i=1}^{N} P_{Poisson}(x_i;a) \tag{5.7}$$

where the counts in channel i are labelled by x_i, which depend on a set of parameters given by a. For convenience, the value normally maximized is $\ln L$. If N is small, the standard deviation of parameter a_j can be estimated by finding the value of a_j at which $\ln L$ drops by a value of 0.5 from its maximum value. The program allows any confidence level to be determined by integrating the likelihood with respect to the parameter of interest. Thus, for a quoted error of

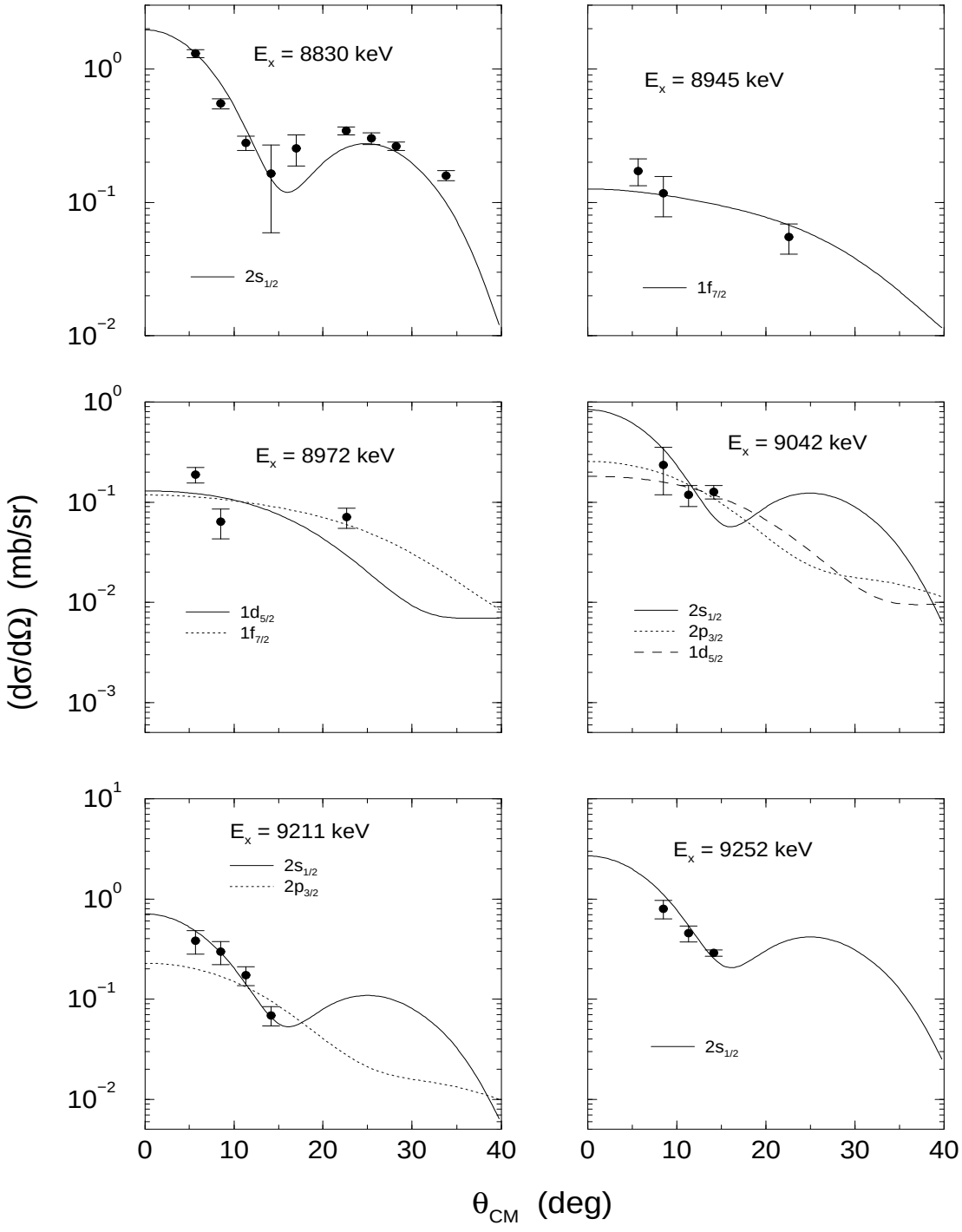

Figure 5.6: Angular distributions and DWBA fits for the states of interest in ^{22}Ne(^{3}He, d)^{23}Na. The angular momentum transfer is noted for each fit. Not all fits are shown, for reasons of clarity. Energies noted are from the present study.

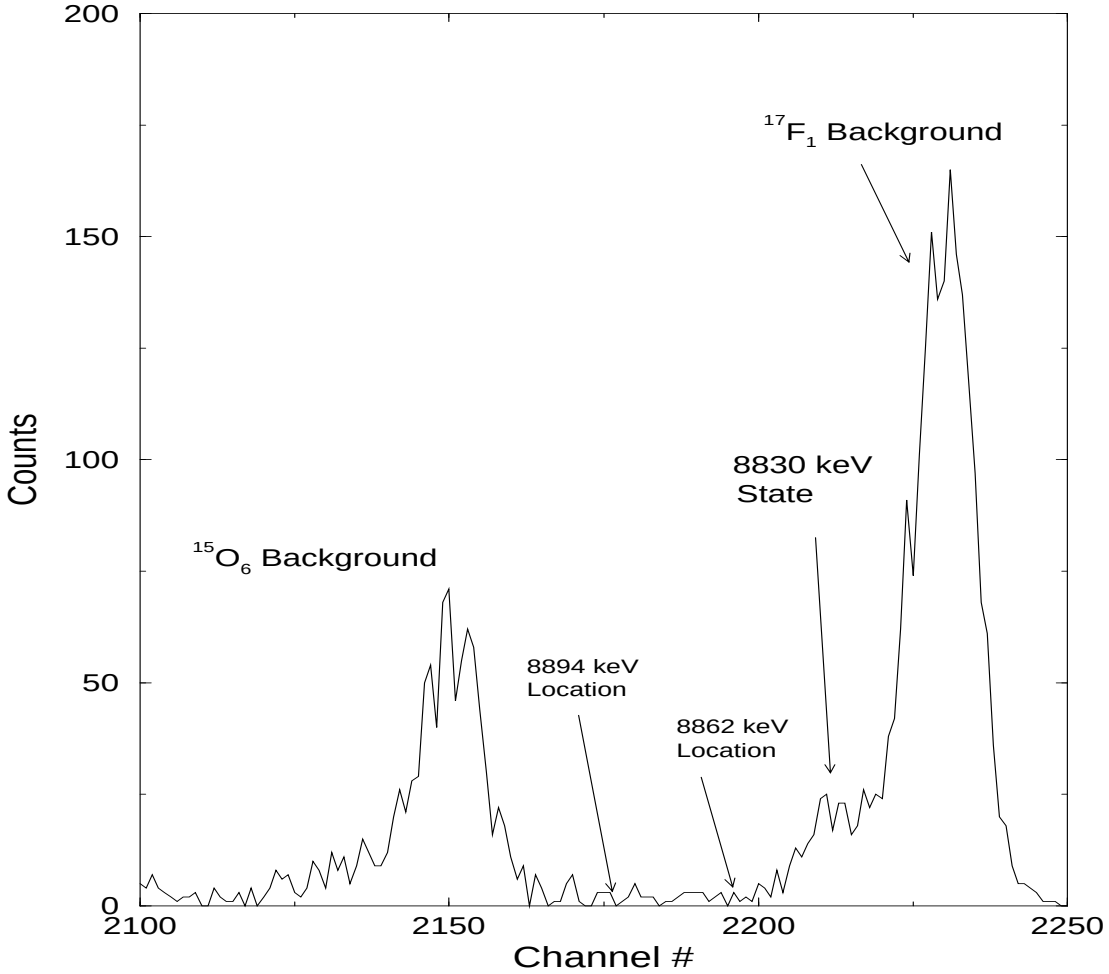

Figure 5.7: Region of interest for the two tentative states at 8862- and 8894-keV at 10°.

Δa_j on the parameter a_j, the confidence level is

$$\text{C.L.} = \int_{a_j-\Delta a_j}^{a_j+\Delta a_j} L_{a'_j}\ da'_j, \tag{5.8}$$

where $L_{a'_j}$ is the likelihood normalized with respect to the variable a'_j.

The signal shape and background shape are programmed into the code. They are held fixed while their normalization is varied in maximizing $\ln L$. Thus, for the mean number of counts in channel i, μ_i, we have

$$\mu_i = Bb_i + Ss_i, \tag{5.9}$$

in which b_i and s_i are the background and signal shapes, respectively. B and S are the normalizations of these shapes. For the peaks of interest in this study,

a linear background and a Gaussian peak shape were chosen. The standard deviation, σ, of the Gaussian was taken to be an average of the σ values from other peaks that were fit at the same angle.

The difficulty with looking for the number of counts in peaks that *might* exist is demonstrated in Figure 5.8. The maximum $\ln L$ corresponds to a physically unrealizable situation, a negative value of S which results in negative counts in the peak. In such a situation, the concept of a ΔS corresponding to a symmetric confidence belt loses its physical meaning. Thus, some method of determining upper limits on the number of counts, and hence the cross section, must be used. Unfortunately, there is no established convention on how this should be done (see, *e.g.*, [Bar89], The Review of Particle Properties [Par92] pages III.32 to III.42, [Cow98], and references therein). The method chosen for this work was to renormalize the likelihood function such that the integral over the physical region ($S > 0$) is equal to unity. The resulting new likelihood is then integrated up to the value of S at which 90% of the area is included. This is then reported as the upper limit at the 90% confidence level.

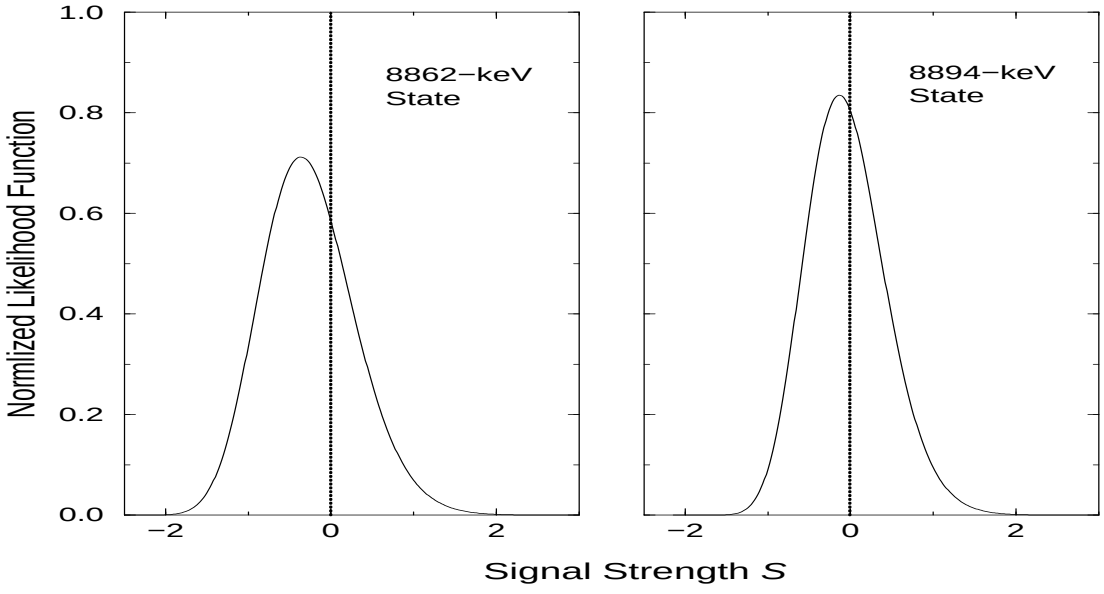

Figure 5.8: Normalized likelihood functions for the two states at 8862- and 8894-keV at 10°. The parameter S is the height of the signal shape.

The results of this procedure for the examples shown in Figure 5.8 are shown in Figure 5.9 with the location of the S parameter for the 90% confidence level.

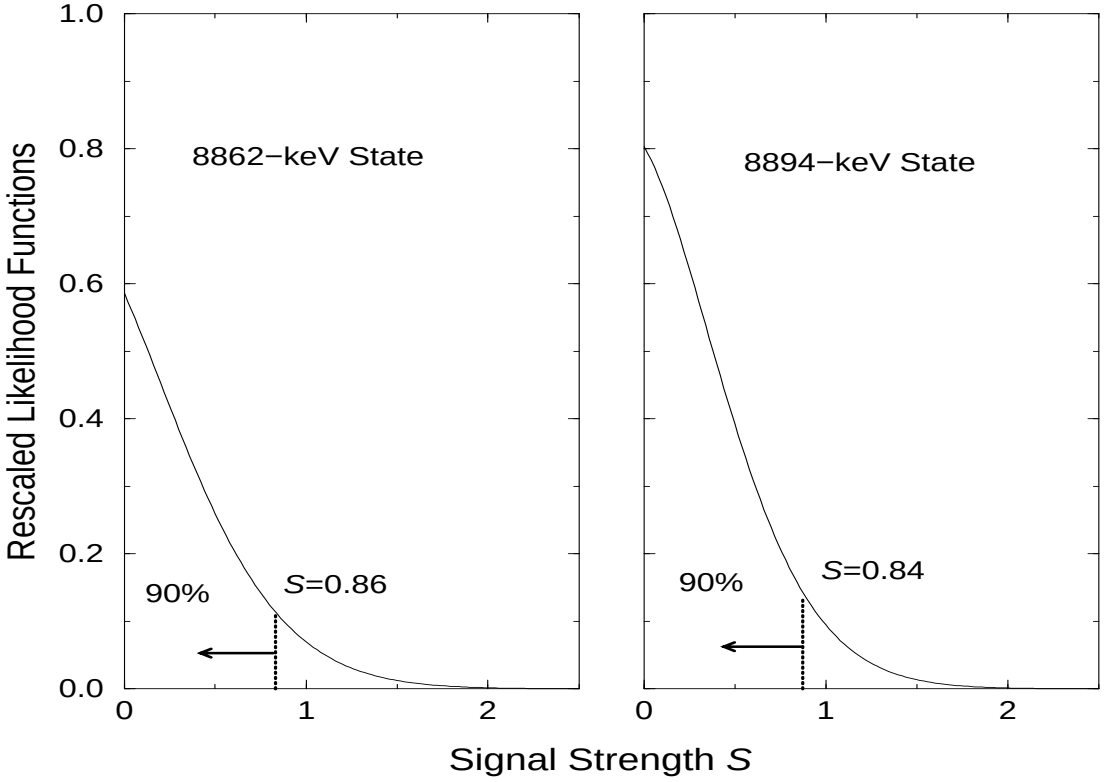

Figure 5.9: The rescaled $\ln L$ functions for the two states of interest at 10°. The 90% confidence level of S is indicated by the dotted vertical line.

The resulting angular distributions are shown in Figure 5.10. The data were analyzed by assuming a J^π value of $\frac{1}{2}^+$ for each state, which would correspond to the largest contribution to the reaction rate.

Values of $(2J_f + 1)C^2S$ and $(2J_f + 1)\Gamma_p$ along with the resulting $\omega\gamma$ values and related uncertainties will be discussed in Section 5.5

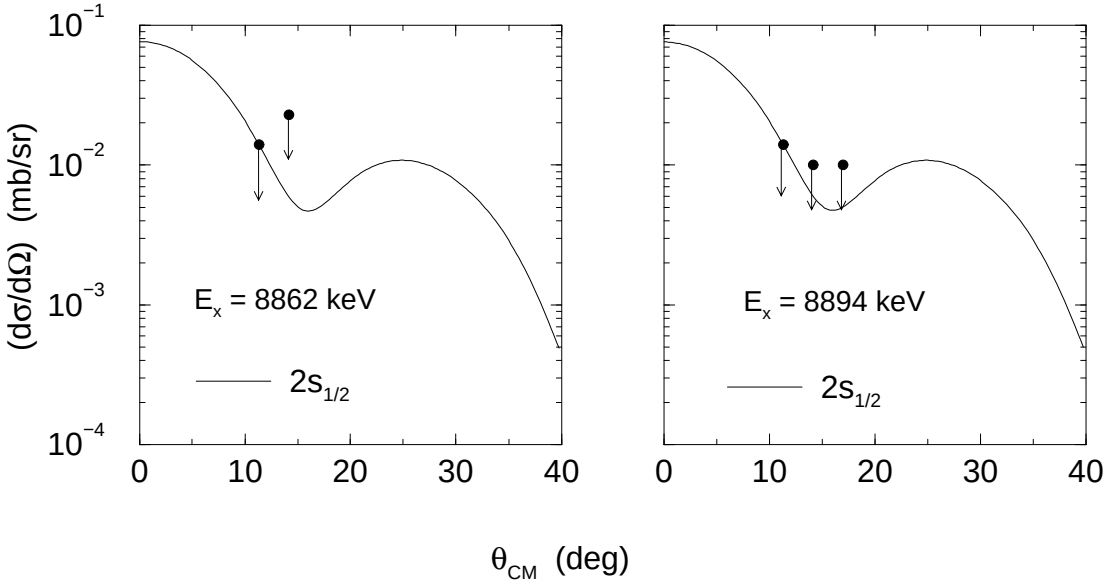

Figure 5.10: Angular distributions and DWBA fits for the two states at 8862- and 8894-keV states in ^{22}Ne$(p,\gamma)^{23}$Na. A value of $J^\pi = \frac{1}{2}^+$ was assumed for each state.

5.5 Results and Uncertainties for ^{22}Ne$(p,\gamma)^{23}$Na Resonances

5.5.1 C^2S, Γ_p and $\omega\gamma$ Values

The results of the DWBA analysis of the states described in Sections 5.4.1 and 5.4.2 are shown in Table 5.8. Using an l-transfer value from a given J^π assignment or assumption, values of $(2J_f + 1)C^2S$ and $(2J_f + 1)\Gamma_p$ are shown. The single-particle proton widths calculated by DWUCK4 were used for all of the states presented here.

Information regarding states of interest has been obtained from several previous studies. In particular, data also exist from a $(^3\mathrm{He}, d)$ study by Powers *et al.* [Pow71], a (d, n) study by Childs *et al.* [Chi73], a direct measurement of ^{22}Ne$(p,\gamma)^{23}$Na by Görres *et al.* [Gör82] which resulted in numerous upper limits, and a direct capture study by Görres *et al.* [Gör83] which modified some of the upper limits in their previous work.

E_x (keV)	J^π	l	Q^2	$(2J_f+1)C^2S$	$(2J_f+1)\Gamma_p$ (eV)
8830	$\frac{1}{2}^+$	0	8.4	0.039	9.3×10^{-15}
8862	$\frac{1}{2}^{+a}$	0	n.a.	≤ 0.0015	$\leq 3.9 \times 10^{-10}$
8894	$\frac{1}{2}^{+a}$	0	n.a.	≤ 0.0016	$\leq 2.8 \times 10^{-7}$
8945	$\frac{7}{2}^-$	3	1.3	0.0087	2.1×10^{-8}
8972	$\frac{5}{2}^{+a}$	2^b	8.0	0.0050	7.6×10^{-6}
	$\frac{7}{2}^{-a}$	3^b	4.9	0.0092	1.8×10^{-7}
9042	$\frac{1}{2}^{+a}$	0	5.9	0.020	0.25
	$\frac{3}{2}^{-a}$	1	1.2	0.0041	0.011
	$\frac{5}{2}^{+a}$	2	0.7	0.0058	3.6×10^{-4}
9211	$\frac{1}{2}^{+c}$	0	0.6	0.020	18
	$\frac{3}{2}^{-d}$	1	3.5	0.0039	0.84
9252	$\frac{1}{2}^+$	0	3.5	0.079	130

[a] Assumed J^π values.

[b] l-value based on fits of [Pow71]. Results from present data.

[c] Based on present study.

[d] Based on [End90a].

Table 5.8: $(2J_f+1)C^2S$ and $(2J_f+1)\Gamma_p$ values for states in ^{22}Ne(^{3}He, d)^{23}Na corresponding to ^{22}Ne + p resonances for $E_{cm} \leq 460$ keV.

The 8830-keV state has been seen previously in (^{3}He, d), (d, n), and direct capture. The stripping studies result in values of $(2J_f+1)C^2S = 0.05$ and 0.08, respectively. However, the data were analyzed by assuming that the state was bound. The direct capture study obtained a value of $(2J_f+1)C^2S$ of 0.054 ± 0.010, which results in $(2J_f+1)\Gamma_p = 1.4 \times 10^{-14}$ eV, which coresponds well with the present value. The strength of the resonance is thus 4.7×10^{-15} eV from the present work and 6.8×10^{-15} eV from direct capture, in agreement with each other. The present strength is adopted for this resonance.

The 8862-keV state was not seen in the direct measurement ($\omega\gamma \leq 3.2$ μeV) or the direct capture study ($\omega\gamma \leq 4.2 \times 10^{-9}$ eV), which assumed $J^\pi = \frac{1}{2}^+$. The upper limit on the resonance strength from the present work using the same J^π assumption is $\omega\gamma \leq 2.0 \times 10^{-10}$ eV.

Similarly, the upper limit on the resonance strength from the 8894-keV state has been lowered. The direct measurement reported $\omega\gamma \leq 0.6$ μeV, while the direct capture obtained $\omega\gamma \leq 5.6$ μeV. The present work obtains a value of $\omega\gamma \leq 0.14$ μeV. The last two values were derived assuming $J^\pi = \frac{1}{2}^+$.

The state at 8945 keV has a J^π value of $\frac{7}{2}^-$, based on l-transfer seen in the (d, n) study and the observation that this state decays 100% of the time to a $\frac{9}{2}^+$ state at 2704 keV [End90a]. Powers *et al.* observed the state but noted that it seemed to be uncharacteristic of pure-l transfer. Their Table III contains a misprint in which the fit of the 8972-keV state is reported as that of the 8945-keV state. Based on an l=3 transfer, the current study finds a resonance strength of $\omega\gamma = 1.1 \times 10^{-8}$ eV, lower than the currently used value (based on the Powers reported value) of $\omega\gamma = 6.5 \times 10^{-7}$ eV.

The observation of the 8972-keV state by Powers *et al.* with an l-transfer of 2 or 3, corresponded to $(2J_f + 1)C^2S = 0.013$ $(1d_{\frac{5}{2}})$ or 0.030 $(1f_{\frac{5}{2}})$, respectively. Again, it should be noted that these were obtained by assuming the state was bound. For the upper limit of a $1d_{\frac{5}{2}}$ transfer, the present work obtains a value of $\omega\gamma = 3.8$ μeV. The quality of our angular distribution prevents an indepedent determination of the l-transfer. The upper limit from the direct (p, γ) measurement is 2.6 μeV, so the two measurements are in fair agreement. The lower limit is adopted in this study.

The 9042-keV state was found to have $\omega\gamma \leq 2.6$ μeV in the direct measurement. The present study finds as an upper limit from l=0 transfer a value of 125 meV. The best fit for the $1d_{\frac{5}{2}}$ transfer results in $\omega\gamma \leq 160$ μeV. The limited angular distribution data prevent a more restrictive assignment. Thus, the most restrictive limit (from the direct measurement) will be used.

The last two states below $E_{cm} = 460$ keV that are analyzed here have been measured directly by Meyer & Smit [Mey73]. For the 9211-keV state, they report a strength of $\omega\gamma = 0.065$ eV. Since there is no other width information about the state, and the values determined in this study for the proton-partial width

are on the order of eV, the assumption that $\omega\gamma \approx \omega\Gamma_p$ cannot be used. Using the directly measured $\omega\gamma$ value and the two possible Γ_p values from the current study, $\Gamma_p = 9.0$ eV ($\frac{1}{2}^+$) or 0.21 eV ($\frac{3}{2}^-$), the combination of $\Gamma_p\Gamma_\gamma/\Gamma$ is 0.065 eV ($\frac{1}{2}^+$) or 0.033 eV ($\frac{3}{2}^-$). It appears that, for this state, $\Gamma_p \approx \Gamma$ and thus $\omega\gamma \approx \omega\Gamma_\gamma$.

Similarly for the 9252-keV state, the directly measured strength is $\omega\gamma = 0.5$ eV. With the present proton partial width of $\Gamma_p = 65$ eV, the situation is again $\Gamma_p \approx \Gamma$. This state was observed in the (^{3}He, d) study of Powers *et al.*, who derived a value of $(2J_f + 1)C^2S = 0.032$, assuming the state was bound.

The adopted values of the excitation energies for all states below $E_{cm} = 460$ keV are listed in Table 5.9. The excitation energies have been recalculated using a weighted average of the present results and all previous existing data, corrected for the effect of any changes in masses [Aud95]. Of the states not seen in the present study, the 8798- and 8822-keV states have negligible impact on the reaction rate, the first because of its low energy as a resonance, and the second because of its high spin value. Upper limits have been found for 6 other states in the direct measurement by Görres *et al.* Their values are adopted for the states between 8972 and 9113 keV. The adopted values of $\omega\gamma$ are also given in Table 5.9. The effect of the new $\omega\gamma$ factors will be discussed in Section 7.1.

5.5.2 Uncertainties

In evaluating the error in C^2S and Γ_p obtained from the analysis of (^{3}He, d) data, it is important to analyze the type of input parameters that are used. On the experimental side of the project, poor statistics can lead to large error bars in the cross section data, which makes the choice of a good DWBA fit more difficult. Harder to quantify is the uncertainty that occurs because of the details of the DWBA calculation itself. The assumptions of a zero-range interaction and local potentials can be accounted for by using correction factors. The three sets of optical model potentials for the entrance channel, exit channel, and final state all suffer from uncertainties, as can be seen by looking at the numerous data

E_x (keV)	E_{cm} (keV)	J^π	$\omega\gamma$ (eV)
8798	4	?	
8822	28	$(\frac{9}{2}, \frac{11}{2})^-$	
8829.5	35.4	$\frac{1}{2}^+$	4.7×10^{-15}
(8862)	68	$\frac{1}{2}^{+a}$	$\leq 2.0 \times 10^{-10}$
(8894)	100	$\frac{1}{2}^{+a}$	$\leq 1.4 \times 10^{-7}$
8945	151	$\frac{7}{2}^-$	1.1×10^{-8}
8972	178	?	$\leq 2.6 \times 10^{-6b}$
(9000)	206	?	$\leq 1.4 \times 10^{-6b}$
9042	248	?	$\leq 2.6 \times 10^{-6b}$
9070	276	?	$\leq 2.2 \times 10^{-6b}$
9103	309	?	$\leq 2.2 \times 10^{-6b}$
9113	319	?	$\leq 3.0 \times 10^{-6b}$
9147	353	?	
9170	376	?	
9211.3	417.2	$(\frac{1}{2}^+, \frac{3}{2}^-)^c$	0.065
9252.1	458.0	$\frac{1}{2}^+$	0.5

[a] Assumed J^π values.

[b] From [Gör83].

[c] $\frac{1}{2}^+$ from present study, $\frac{3}{2}^-$ from [End90a].

Table 5.9: Adopted $\omega\gamma$ values for ^{22}Ne$(p,\gamma)^{23}$Na.

sets in a compilation such as [Per76]. The effect of these errors or ambiguities is explored here.

The choice of step size and cutoff radius R_{max} (where the internal and external wave functions are matched) in the numerical integration of the wave functions in DWUCK4 can also affect the value of the single-particle proton width. In the manner of [Ili97], this effect was checked by varying both the step size and the value of R_{max} and verifying that the value of Γ_{sp} did not vary by more than 5%.

Finite-range (FR) and non-locality (N-L) correction parameters were used as given in [Bas66]. The finite-range correction factor is 0.77 fm for (^{3}He, d) and the non-locality correction factor values are 0.25 fm for the ^{3}He and 0.54 fm for the deuteron. The effect of turning off the corrections either simultaneously or one at a time was investigated and found to result in a change of 20% for the value of C^{2}S for both the 8830-keV state and the 9701-keV state, though the quality of the fit did not change significantly. The different fits are shown in Figure 5.11. Since there is not any justification for neglecting the correction factors, they are left on throughout the analysis of the ^{22}Ne(^{3}He, d)^{23}Na data.

In order to determine the error associated with the fit to the data points, the normalization of the DWBA prediction for the 8830-keV state was varied. The

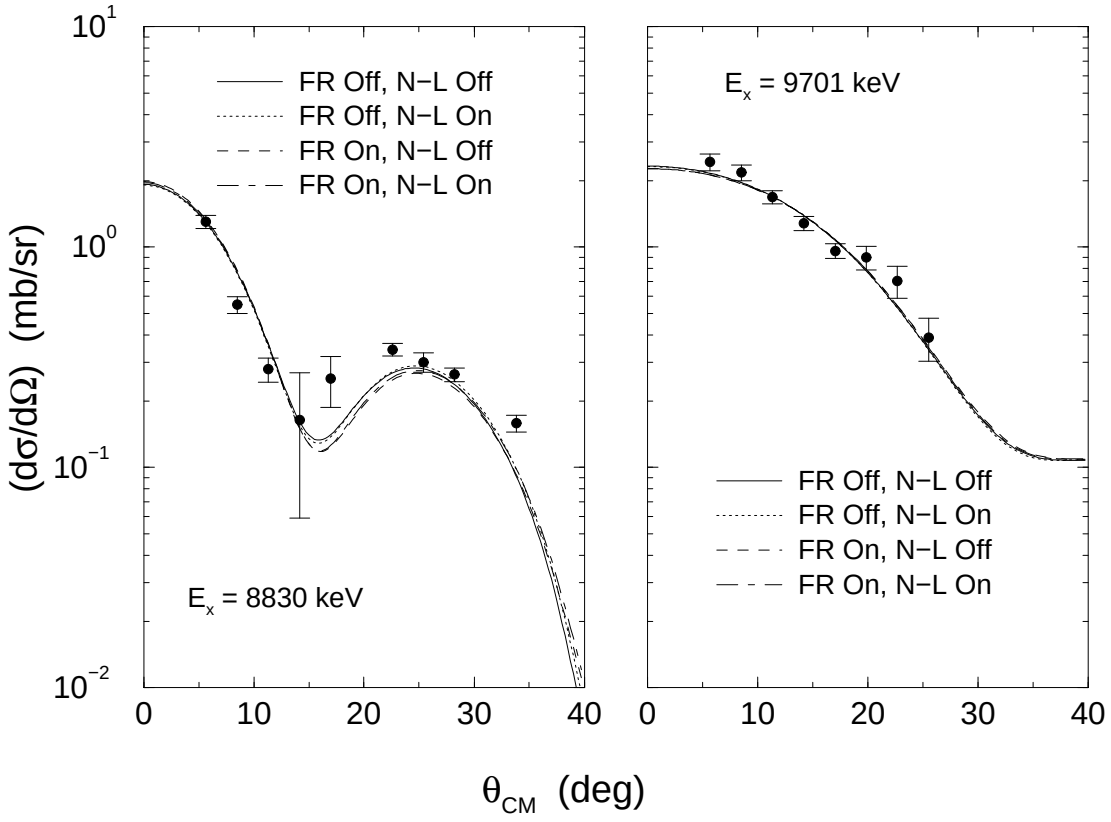

Figure 5.11: Test of the effects of turning the finite-range (FR) and non-locality (N-L) corrections on and off for the states at 8830 keV (l = 0) and 9701 keV (l = 2). The change in the Q^2 of the fit was negligible.

value which minimized $Q^2(\alpha)$ in Equation 5.1 was used to determine a value of C^2S. The normalization was then varied until the value of $Q^2 \cdot (i_{max}+1)$ (since Q^2 is calculated per degree of freedom) increased from its minimum value, Q^2_{min}, to $Q^2_{min}+1$. The resulting error in C^2S was found to be 3.1%. A similar process with the elastic scattering data resulted in an error of 2.6%.

The error resulting from the choice of final-state parameters, r_r, a_r, and r_c, was investigated by trying two different sets (those from [Ili97] and the more standard set of $r_r = 1.25$ fm, $a_r = 0.65$ fm, and $r_c = 1.25$ fm). The error in C^2S that resulted was 2.1%, while the prediction of Γ_{sp} changed by 2.0%. By changing the values of r_r and a_r by up to 10%, it was found that C^2S and Γ_{sp} change by up to 40%, but consistently in opposing directions. Thus the resulting change in the physical parameter Γ_p was less than 5% over this range of r_r and a_r. The value of Γ_{sp} depends on the matching of the internal wave function of the proton to the external Coulomb wave function, so changes inside the nucleus can create large variations. However, the value of Γ_p is not as sensitive to the interior of the nucleus, since it effectively measures the probability that a proton will be able to make it through the Coulomb and centrifugal barrier to the nucleus.

The value of C^2S depends on the ratio of the ^{22}Ne(^{3}He,^{3} He)^{22}Ne and the ^{22}Ne(^{3}He, d)^{23}Na calculated cross sections. To obtain a value for the uncertainty related to the optical model uncertainties, these two cross sections were calculated using DWUCK4 for 2 separate sets of optical model potentials and compared over the angular range of 0° to 20°, where the treatment of the reaction as single-step is most likely to hold true. This provided an estimate of the error resulting from different optical model sets. This test was performed for all three sets of optical model parameters in Table 5.2. The effect of varying the ^{22}Ne+p parameters was found from the comparison mentioned above, between the conventional values for the radius and diffuseness and those from [Ili97]. The ratios of the cross sections from varying the ^{3}He and the d parameters are shown in Figure 5.12. The (^{3}He, d) calculations were performed for the 8830 keV state in ^{23}Na.

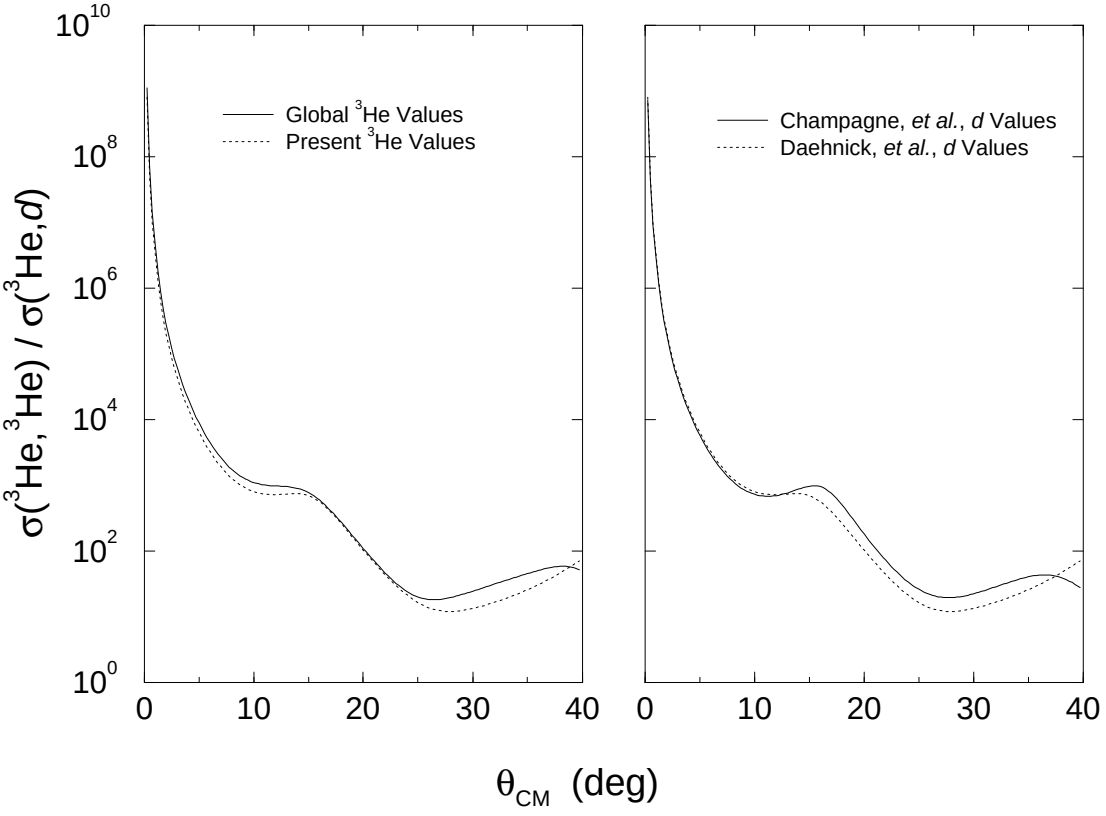

Figure 5.12: Optical model potential parameter test for entrance and exit channels of ^{22}Ne(^{3}He, d)^{23}Na.

The ^{3}He variation was done using the d and p parameters listed in Table 5.2 with the two ^{3}He parameter sets from Table 5.1. Integrating the average difference between the two predictions from $0°-20°$ results in an error of 24%.

The d variation was performed using the ^{3}He and p parameters listed in Table 5.2 with the d parameter sets coming from Daehnick's predictions (also in Table 5.2) and a separate set of parameters from a study of ^{25}Mg(^{3}He, d)^{26}Al performed by Champagne *et al.* [Cha89]. Deuteron energies from the ^{25}Mg investigation were comparable to those of the reactions investigated in this study ($E_d \approx$ 12-15 MeV). The parameters are listed in Table 5.10 and compared with the values calculated from Daehnick's parametrization. Again integrating the average difference between the two predictions over the $0°$ to $20°$ range gives an error of approximately 11%.

Ref.	V_r	r_r	a_r	W_i	W_D	$r_i = r_D$	$a_i = a_D$	V_{so}	r_{so}	a_{so}
[Cha89]	120.0	1.00	0.90	0.0	100.0	1.50	0.50	0.0	0.0	0.0
[Dae80]	88.0	1.17	0.73	0.24	35.8	1.33	0.73	13.85	1.07	0.66

Table 5.10: The deuteron optical model parameters used in testing the resulting error in C^2S values.

The contributions to the errors on C^2S are given in Table 5.11. Treating these errors as independent results in a total error for C^2S of 27%. This is consistent with Endt's evaluation of a 25% error in single-nucleon stripping reactions (for strong transitions) in the *sd*-shell [End77]. Thompson and Iliadis [Tho99] found a typical uncertainty in measured S values of about 40%. This value came from comparing neutron spectroscopic factors in the s-d shell for both bound and unbound states. A total of 46 states were analyzed which had two or more experimental determinations of S.

The errors in Γ_p are a bit more difficult to quantify due to the interplay between C^2S values and Γ_{sp} predictions. A study by Iliadis *et al.* [Ili99] compared proton partial widths derived from nucleon transfer reactions and resonant reactions for 21 pairs of transitions in the s-d shell. Their conclusion was that a factor of 1.7 uncertainty can be quoted reliably. Based on the values of the three unbound states listed in Table 5.4, an accuracy of a factor of 2 seems to be a conservative estimate.

Source of Error	Nature of Error	% Error of C^2S
$(^3He, d)$ Fit	Statistical	3.1
Elastic Data Fit	Statistical	2.6
^3He OMP	Systematic	24
d OMP	Systematic	11
p OMP	Systematic	2.1

Table 5.11: Sources of error for C^2S in $^{22}Ne(^3He, d)^{23}Na$. The errors should be independent.

Chapter 6

^{23}Na(^{3}He, d)^{24}Mg Analysis

As was done for the ^{22}Ne(^{3}He, d)^{23}Na data, the ^{23}Na(^{3}He, d)^{24}Mg cross sections were normalized to elastic scattering. Since the data were collected at different times, the monitor detector elastic peak from ^{3}He scattering off ^{23}Na was again used to apply the elastic cross section to the stripping data. Details of the cross section determination are given in Section 6.2.

6.1 ^{3}He Elastic Scattering

Data were taken on ^{23}Na(^{3}He,^{3} He)^{23}Na over the same angular range as the neon elastic scattering, 15° to 45° in steps of 5°. The parameter expressions of Becchetti and Greenlees [Bec71] were used to calculate the ^{23}Na + ^{3}He optical model parameters. The change from the predicted parameters for ^{22}Ne + ^{3}He was quite small, as might be expected from the small change in mass and charge, and again the fit was found to be unsatisfactory. After varying the parameters independently, and comparing the results versus those using several sets from [Per76], it was decided to scale the global predictions by the same amount as the ^{22}Ne parameter predictions. The results obtained using both the original parameters and the final values are shown in Figure 6.1. The two sets of parameters are shown in Table 6.1. The goodness of fit parameter, Q^2, has the values of 11.7 and 2.3 for the global ^{3}He parameters and the adjusted set, respectively.

Ref.	V_r	r_r	a_r	W_i	r_i	a_i
[Bec71]	150.7	1.20	0.72	37.01	1.40	0.88
Present	159.3	1.05	0.72	42.12	1.33	0.86

Table 6.1: Optical model parameters of [Bec71] and the results of scaling the parameters in the same amounts as the ^{22}Ne + ^{3}He parameters. The parameters are as defined in Eq. 2.34. The potential depths are in MeV, while the radii and diffuseness parameters are in fm. The Coulomb radius, as defined in Eq. 2.33, is $r_c = 1.3$ fm.

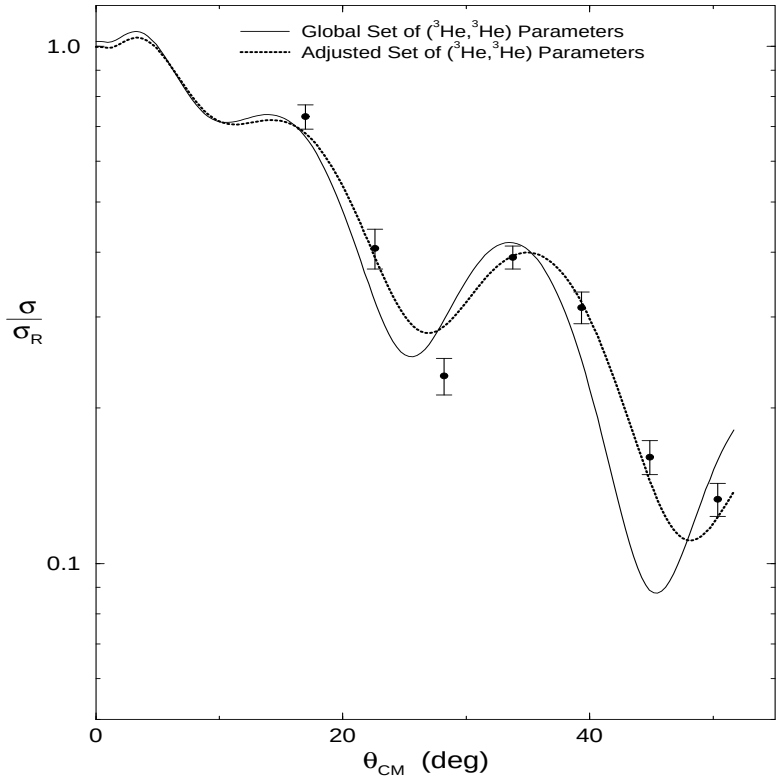

Figure 6.1: Elastic scattering of ^{3}He off ^{23}Na. The effect of changing the ^{23}Na + ^{3}He optical model parameters is shown.

Normalization of the data to the theoretical curve implied a monitor cross section of 7.98 ± 0.19 mb/sr, reflecting only the statistical error in the fit. The errors from the DWBA fits are evaluated in Section 6.5.2.

6.2 Cross Section Determination

As mentioned in Section 4.4, the resolution in the monitor detector during the February 1998 run was not sufficient to allow elastic ^{3}He counts to be extracted. To solve this problem, the counts for all the states in ^{24}Mg were first normalized to the counts in the 8655-keV state in ^{24}Mg, which was then expressed in terms of the monitor counts using the October 1998 data. The monitor spectrum shown in Figure 4.7 is typical of the elastic peaks that were fitted to extract counts during this run. The normalization data were collected at all of the angles where data were obtained in February. The behavior of the monitor detector was continuously checked to ensure clean spectra. Data were taken at each angle until the statistics for the 8655-keV state were better than 5%, which resulted in monitor peak statistics of better than 3%.

To test the normalization method, the cross sections for the states at 9458 and 9516 keV were calculated using only October data, and using the February data normalized through the 8655-keV state. The results are shown in Figure 6.2. The counts from each detector were corrected for dead-time effects in calculating the cross sections. Fitting deuteron peaks in the Enge spectra was typically done using a Gaussian combined with a polynomial background.

6.3 Calibration Peaks and Energy Calibration

The deuteron spectrum in Figure 6.3 was collected at $\theta_{\rm lab} = 12.5^\circ$ from the NaBr target, and shows the region from 10712- to 13090-keV excitation energy in ^{24}Mg, which corresponds to a deuteron range from 12726 to 15191 keV. The region of astrophysical interest stretches roughly from channel 1600 to 1900. Counts and centroids were first extracted for the numerous large peaks on either side of this region. All peak energy labels are in keV, taken either from Endt [End90a] and corrected for the effects of new masses [Aud95] in the case of the calibration peaks, or from this study (as discussed in Section 6.4) for the

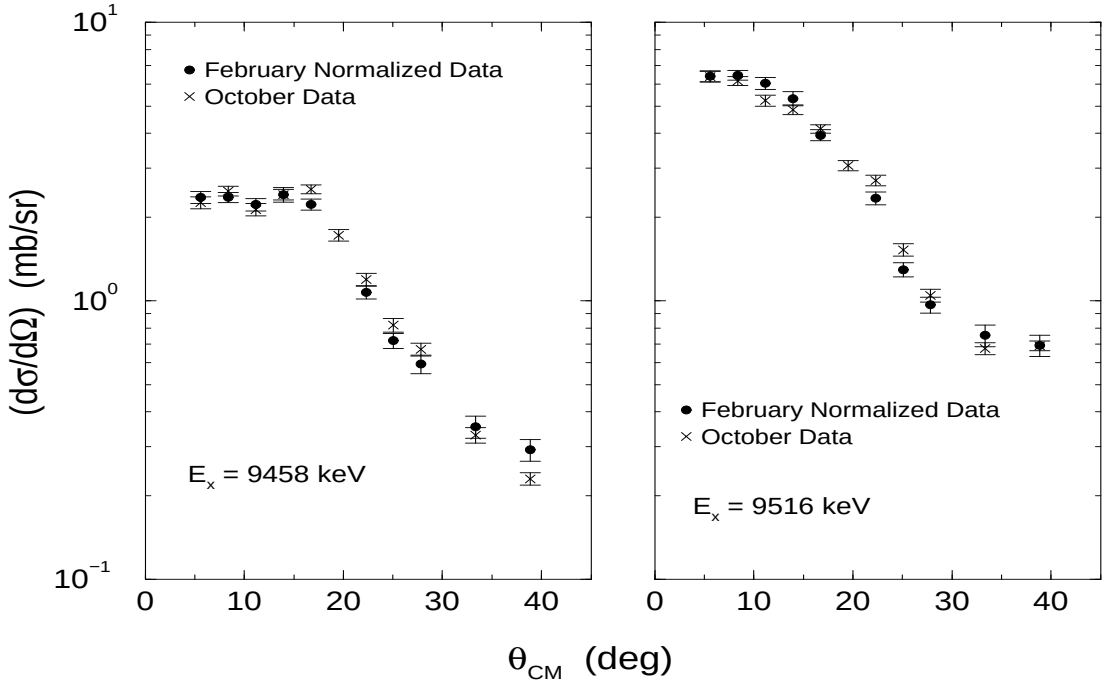

Figure 6.2: Comparison of normalized and unnormalized cross sections for the 9458- and 9516-keV state in ^{24}Mg.

peaks from channel 1600 to 1900. Contaminant peaks from the ^{12}C, ^{14}N, and ^{16}O in the target are also labelled by the final state formed. Unlabelled peaks correspond to mixtures of states in ^{24}Mg. The high level density of ^{24}Mg prevented some states from being used for calibration purposes because of uncertain identification.

A total of 12 peaks above and below the region of interest were analyzed for calibration purposes. The energies of the calibration states are shown in Table 6.2. A 3rd-order polynomial was used to fit the E_x vs. channel number data, calibrating the peaks in terms of ^{24}Mg excitation energies directly. The error in the calibration was estimated to be $\pm$ 2 keV for $\theta \leq 10^\circ$ and $\pm$ 3 keV for $\theta \geq 12.5^\circ$, based on predictions of the known energies of states not used in the calibration scheme.

The entrance channel optical model parameters were taken from the results of the (^{3}He,^{3} He) scattering, and given in Table 6.1. The optical model param-

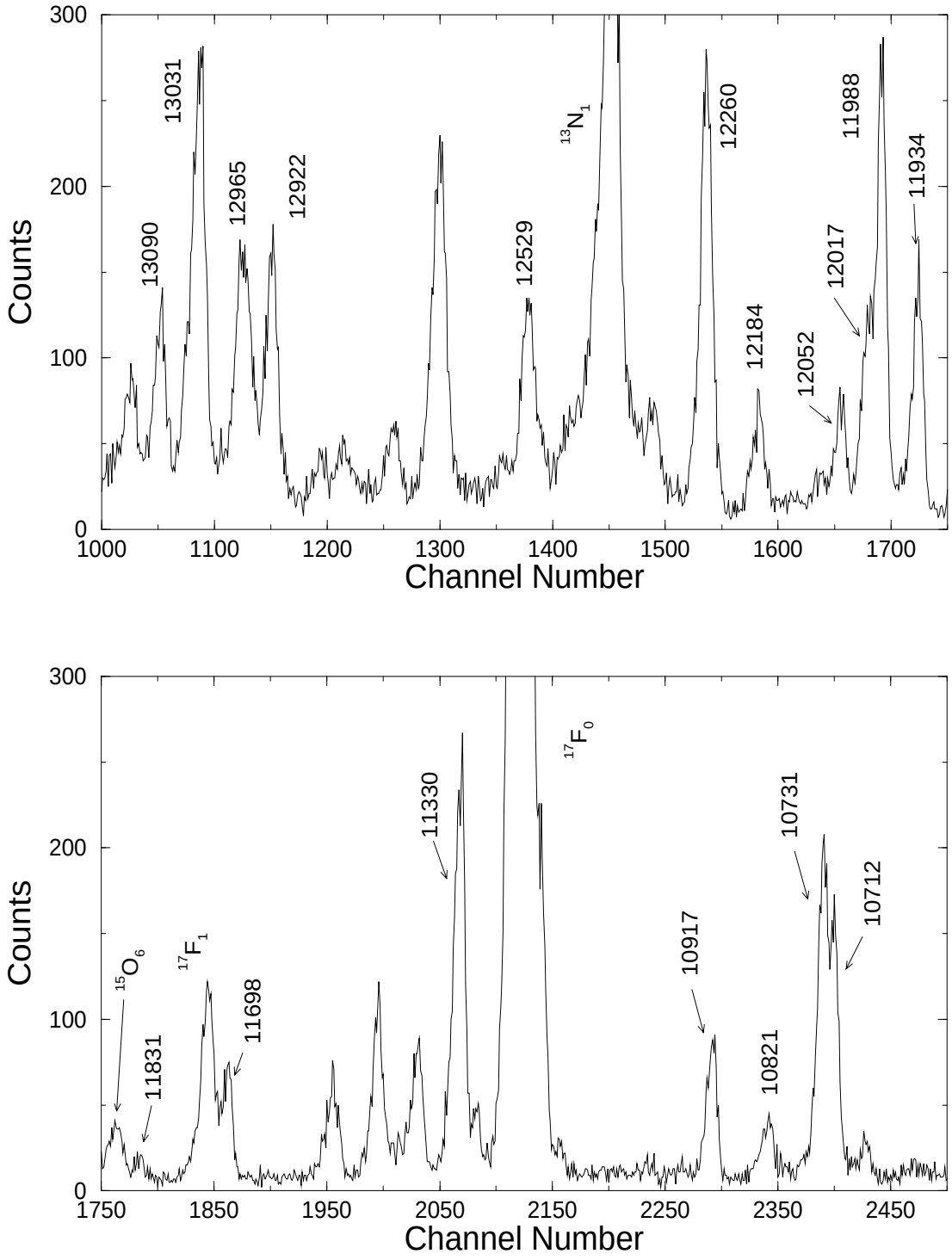

Figure 6.3: Deuteron spectrum from ^{23}Na(^{3}He, d)^{24}Mg at 12.5° from the NaBr target. The peaks are labelled either by their energy in ^{24}Mg in keV or by the final state formed from a contaminant in the target.

E_x (keV)	J^π
10712.2 ± 0.2	1^+
10731.1 ± 0.2	2^+
10820.8 ± 0.4	3^+
10917.2 ± 0.3	2^+
11330 ± 3	$(2\text{-}4)^+$
12183.7 ± 0.7	$(1,2)^+$
12259.8 ± 0.7[a]	3^-
12260.2 ± 0.7[a]	2^-
12529.0 ± 0.8	1^+
12922.3 ± 0.7	3^-
12964.5 ± 0.8	2^-
13030.5 ± 0.6	2^+
13089.5 ± 0.7	3^-

[a] States not resolved.

Table 6.2: Calibration states used in ^{23}Na(^{3}He, d)^{24}Mg spectra. Excitation energies and J^π values are taken from [End90a]. Unbound states are corrected for the change in Q-value where appropriate.

eters for the ^{24}Mg + d channel were calculated from the global parametrization of Daehnick *et al.* [Dae80]. There are very slight changes from those calculated for the ^{23}Na + d channel from Section 5.3.1. The values do not change significantly over the range of deuteron energies for the states that are analyzed in the ^{23}Na(^{3}He, d)^{24}Mg reaction. As in the ^{22}Ne(^{3}He, d)^{23}Na analysis, the volume imaginary strength was set at 0.24 MeV. The final state parameters are the same as those used for the ^{22}Ne target analysis. The full set of optical model parameters used is given in Table 6.3.

Because the ^{23}Na ground state has $J^\pi = \frac{3}{2}^+$, it is possible to form the spin of the final state using two different l-transfers, separated by 2 units of angular momentum. This is because both $j = l_p - \frac{1}{2}$ and $j = l_p + \frac{1}{2}$ can add vectorially

Particle	V_r	r_r	a_r	W_i	W_D	$r_i = r_D$	$a_i = a_D$	V_{so}	r_{so}	a_{so}
^{3}He	159.3	1.05	0.72	42.12		1.33	0.86			
d	88.6	1.17	0.73	0.24	36.1	1.33	0.73	13.86	1.07	0.66
p	[a]	1.17	0.69					$\lambda = 25$		

[a] V varied to match separation energy.

Table 6.3: Optical model parameters used in ^{23}Na(^{3}He, d)^{24}Mg. The parameters are as defined in Eq. 2.34. The potential depths are in MeV while the radii and diffuseness parameters are in fm. The ^{3}He and d Coulomb radii are both 1.3 fm while the p Coulomb radius is 1.28 fm. The ^{3}He parameters are from the fit to the current elastic scattering data. The d parameters are from Daehnick *et al.* [Dae80]. The p parameters are from Iliadis [Ili97].

to the target spin to yield the same J_{final}. In the present case, we must consider combinations of $l = 0 + 2$, $l = 1 + 3$, and $l = 2 + 4$ in addition to pure l-transfer. In the analysis, the lowest open orbital was assumed for a given l_p transfer. Thus the transfers calculated and presented are $2s_{\frac{1}{2}}$, $2p_{\frac{3}{2}}$, $1d_{\frac{5}{2}}$, $1f_{\frac{7}{2}}$, and $1g_{\frac{9}{2}}$. In the event that the true transfer is the alternate j value, the values of $(2J_f + 1)C^2S$ and $(2J_f + 1)\Gamma_p$ tabulated below would have to be multiplied by factors of 0.5, 0.667, 0.75 and 0.8 for transfers of $2p_{\frac{1}{2}}$, $1d_{\frac{3}{2}}$, $1f_{\frac{5}{2}}$, and $1g_{\frac{7}{2}}$ respectively. Since a combination of two l_p transfers will generally give a better fit to the data, such a combination is only adopted if it results in a sizeable improvement in the quality of the fit.

The angular distributions for the five states below the (p, γ) threshold that are used in the calibration are shown in Figure 6.4 along with the results from the DWBA calculations, while those of the unbound calibration states are shown in Figure 6.5. The values of the fit parameter Q^2 and the resulting $(2J_f + 1)C^2S$ values are shown in Table 6.4. At these high excitation energies in ^{24}Mg, not many previous data exist.

The values of $(2J_f + 1)\Gamma_p$ for the unbound states have been calculated using the results shown in Table 6.4 and the Γ_{sp} values returned by DWUCK4. These results are compared to previous values of Vanhoy *et al.*, [Van87] in Table 6.5.

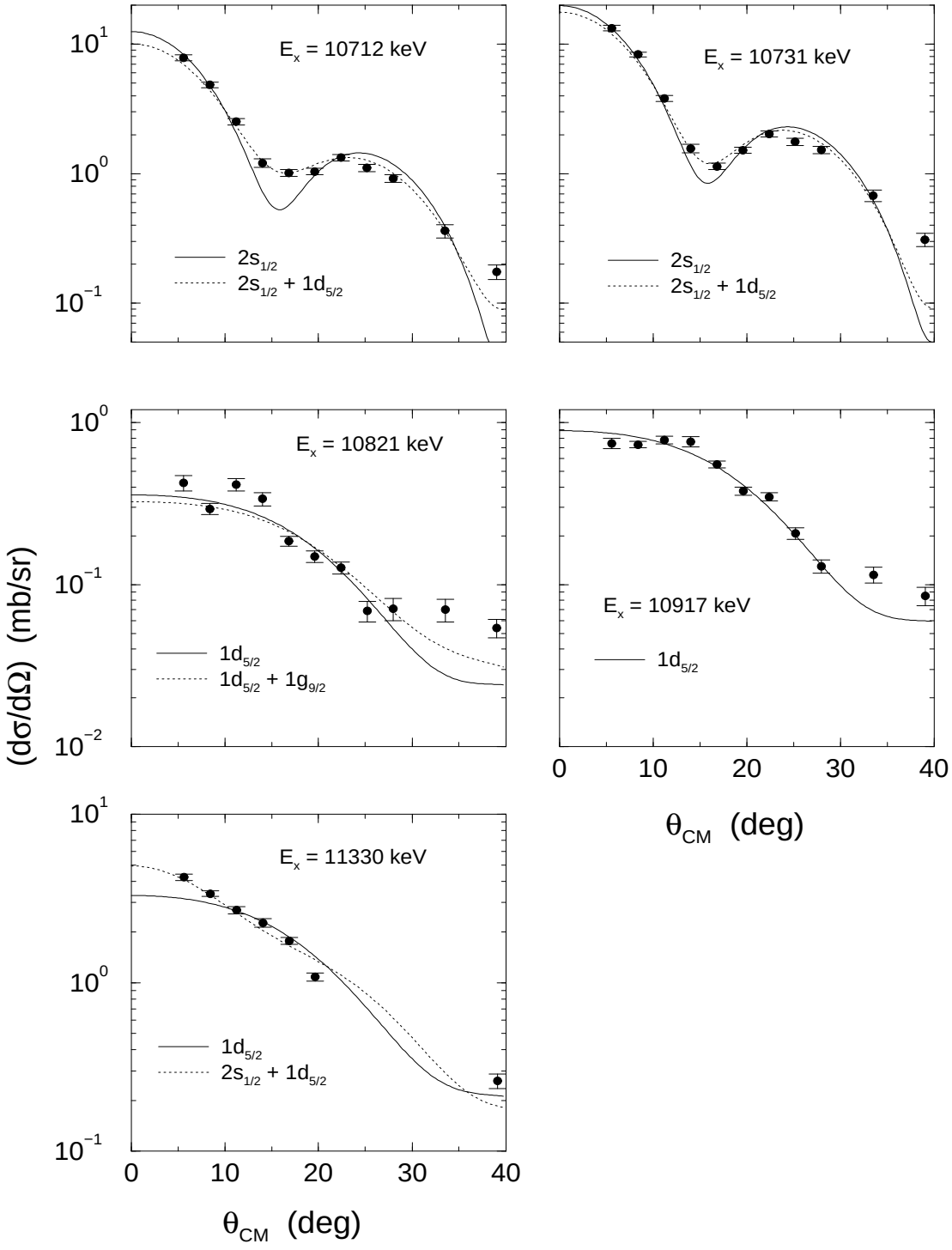

Figure 6.4: Angular distributions and DWBA fits for the bound calibration states in ^{23}Na(^{3}He, d)^{24}Mg. The angular momentum transfer is noted for each fit.

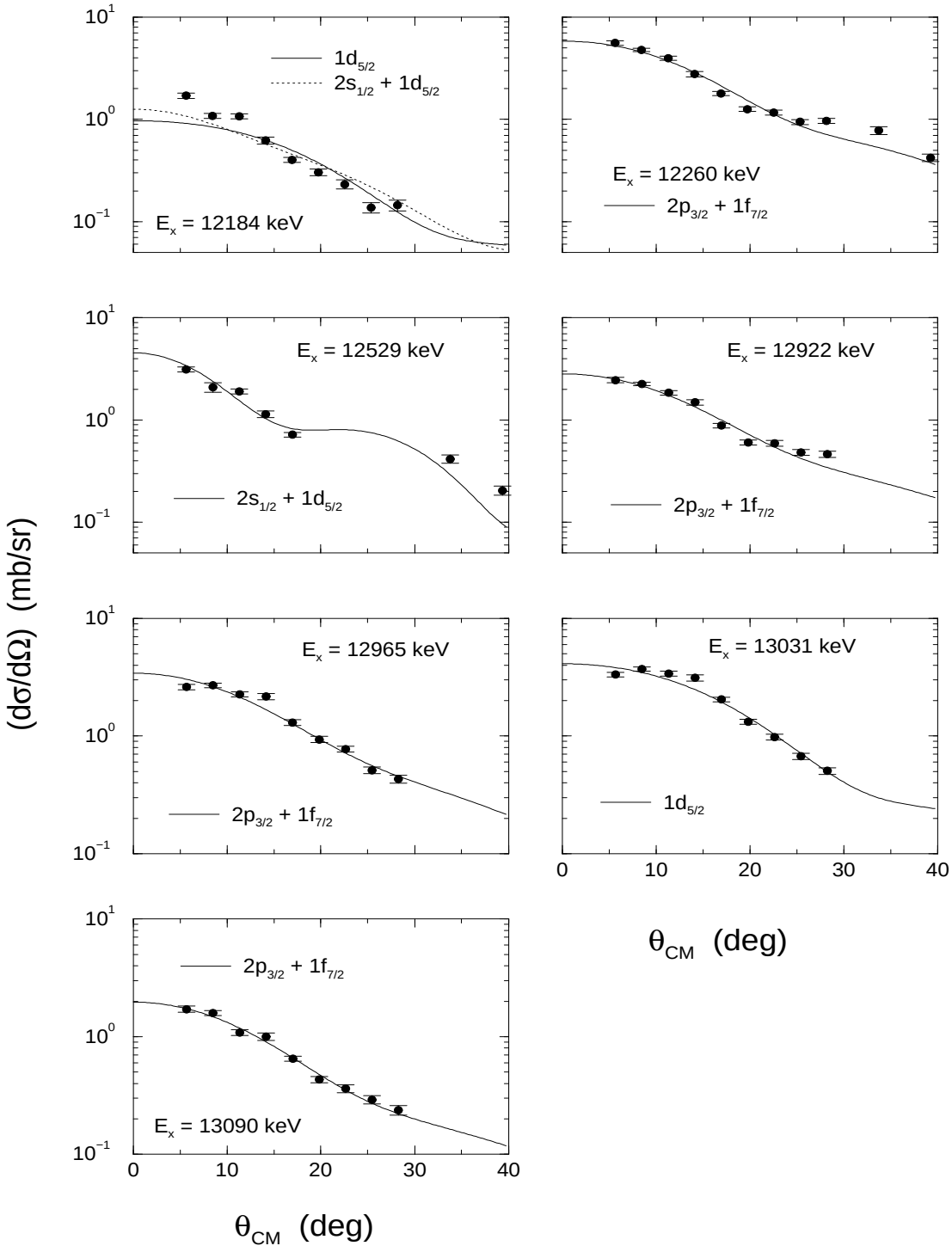

Figure 6.5: Angular distributions and DWBA fits for the unbound calibration states in ^{23}Na(^{3}He, d)^{24}Mg. The angular momentum transfer is noted for each fit.

				$(2J_f + 1)C^2S$	
E_x (keV)	J^π	l	Q^2	Present	Previous [Gar78]
10712	1^+	0	17.2	0.53	[a]
		0 + 2	4.0	0.38 + 0.16	
10731	2^+	0	12.3	0.84	[a]
		0 + 2	8.3	0.72 + 0.12	
10821	3^+	2	6.7	0.057	0.25[b]
		2 + 4	6.5	0.050 + 0.035	
10917	2^+	2	4.3	0.14	0.35[c]
11330	$(2\text{-}4)^+$	2	13.9	0.48	
		0 + 2	7.9	0.13 + 0.40	
12184	$(1,2)^+$	2	18.5	0.13	
		0 + 2	18.6	0.048 + 0.11	
12260[a]	2^-,3^-	1 + 3	8.9	0.35 + 0.28	
12529	1^+	0 + 2	12.9	0.57 + 0.12	
12922	3^-	1 + 3	6.6	0.21 + 0.13	
12965	2^-	1 + 3	4.0	0.31 + 0.19	
13031	2^+	2	4.4	0.56	
13090	3^-	1 + 3	1.6	0.17 + 0.073	

[a] Unresolved doublet.

[b] Tentative $l = 2$ fit.

[c] $l = 2$ fit only.

Table 6.4: $(2J_f + 1)C^2S$ values for calibration states in ^{23}Na(^{3}He, d)^{24}Mg.

6.4 Analysis of States Below $E_{cm} = 400$ keV

The region of interest for ^{23}Na(p,γ) in the (^{3}He, d) spectrum at 17.5° is shown in Figure 6.6. The energy values quoted in the figure reflect the values adopted in this study and discussed below. The states in ^{24}Mg corresponding to resonances in ^{23}Na$(p,\gamma)^{24}$Mg between threshold and a cm proton energy of 400 keV were analyzed in detail. The majority of the states labelled in Figure 2.4 were seen at several angles or more. The 0^+ state at 11730 keV was not seen because of a sizeable background peak from the $^{17}F_1$ state at the lower angles ($\theta < 20°$) and

			$(2J_f + 1)\Gamma_p$ (eV)	
E_x (keV)	J^π	l	Present	Previous
12184	$(1,2)^+$	2	1.2	
		0 + 2	51 + 0.99	
12260[a]	2^-,3^-	1 + 3	270 + 0.20	3^- : 322 ± 28 [b]
12529	1^+	0 + 2	16000 + 52	
12922	3^-	1 + 3	14000 + 25	42000 [c]
12965	2^-	1 + 3	19000 + 46	15000 [c]
13031	2^+	2	3600	l=0 : 2000 [c]
				l=2 : 7000 [c]
13090	3^-	1 + 3	19000 + 31	l=1 : 38500 [c]
				l=3 : 1750 [c]

[a] Unresolved doublet.

[b] From [End90a].

[c] From [Van87].

Table 6.5: $(2J_f + 1)\Gamma_p$ values for calibration states in ^{23}Na(^{3}He, d)^{24}Mg.

because of limited statistics above 20°. The deuteron peak from the 6th state of ^{15}O obscured the two states at 11831 and 11862 keV over several angles. Counts in the 11831-keV peak at 7.5° were extracted from the overlapping peaks. The number of counts expected in the $^{15}O_6$ peak at this angle was determined in relation to the $^{15}O_5$ state which could be fit in the spectrum. The ratio of the counts in the two ^{15}O peaks was found using ^{14}N(^{3}He, d)^{15}O data provided by P. F. Bertone [Ber98]. The amount of nitrogen in the target during the 7.5° and 10° runs based on the $^{15}O_5$ state was averaged and used with the provided data to determine the number of counts in the $^{15}O_6$ peak at 5°, and thus extract the counts in the 11831-keV state. The effect of the cross sections at these angles will be discussed below. The state 2 keV below the 1^- state at 11862, has a J^π of $\geq 6^+$ (requiring an l-transfer greater than 4) which limits its contribution to the peak seen in the present study at that energy, probably to the level of the compound nucleus contribution. The 11910-keV state was not observed at

any angle. The $J^\pi = 6^+$ nature of the state at 12002 keV, as well as its location between two other states with more favorable J^π values prevented its observation.

The states that were observed were fitted at all possible angles. Figure 6.7 shows an example of the fits obtained. The regions around the peaks were plotted on a shifted horizontal scale to ease background estimation. The resulting centroids were converted to full spectrum channels and used in the calibrations to determine excitation energies. Though the spectra were calibrated for all angles up to 25°, the energy predictions from the lowest three angles for each state were used to minimize error. A weighted average of the predicted energies of the observed states was performed. The results are shown in Table 6.6.

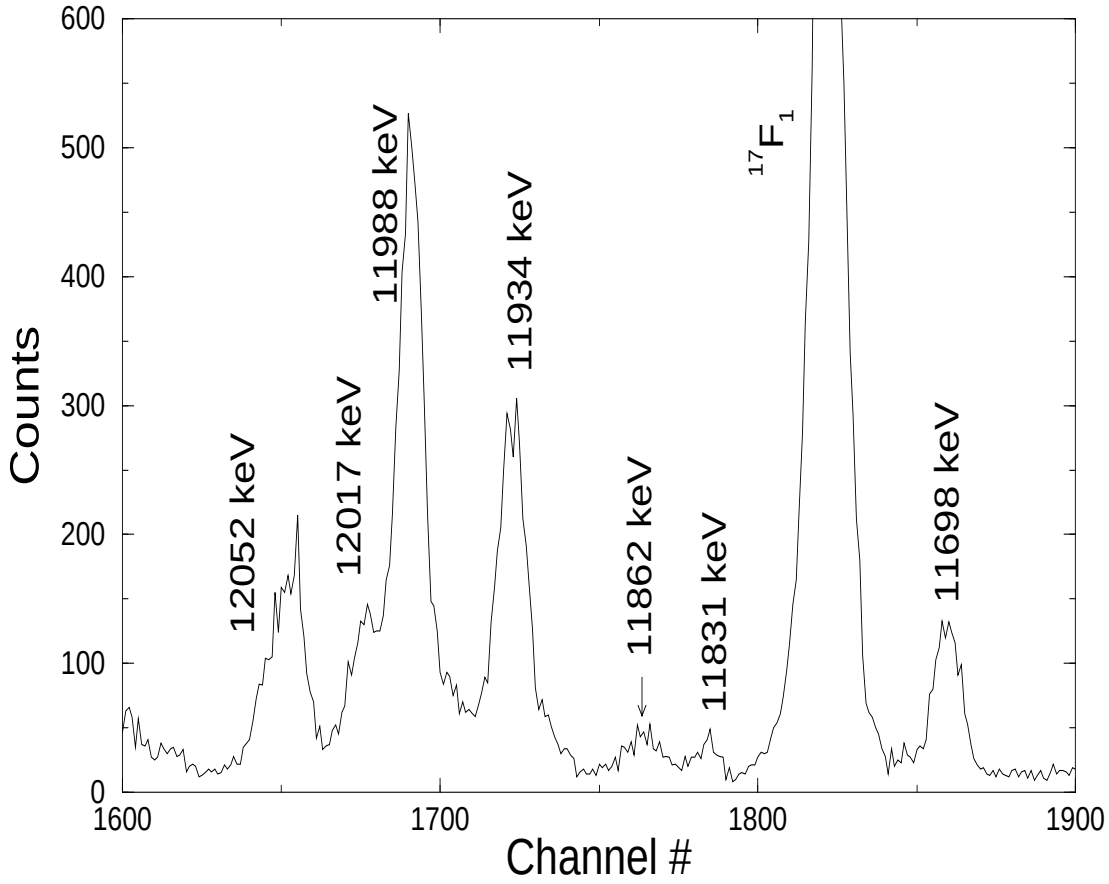

Figure 6.6: Region of interest for $^{23}\mathrm{Na}(p,\gamma)$ at 17.5° in the $(^3\mathrm{He},d)$ spectrum. Peaks are labelled by their excitation energy in the ^{24}Mg nucleus, or by the final state created from a contaminant in the target.

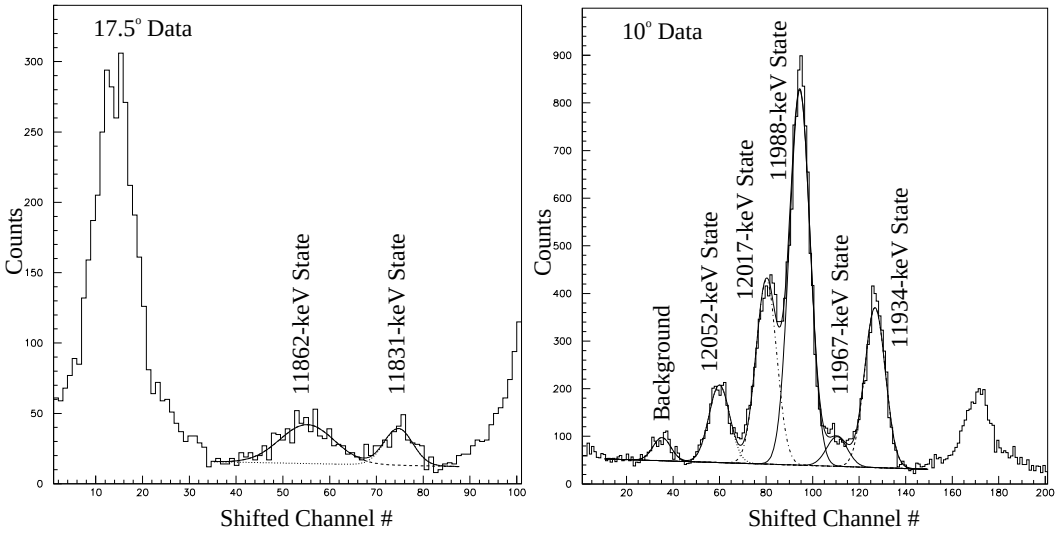

(a) E_x = 11831 and 11862 keV Fits (b) E_x = 11934 to 12052 keV Fits

Figure 6.7: Sample fits from deuteron peaks in ^{23}Na(^{3}He, d)^{24}Mg. The spectra have been shifted to smaller channel regions in order to ease the background estimation for the fitting process. Energy labels reflect the adopted values as listed in Table 6.7.

E_x (keV) Present	E_x (keV) [End90a]
11698.6 ± 1.3	11695 ± 2
11831.7 ± 1.8	11828 ± 3
11862.7 ± 1.2	11864 ± 3
11936.5 ± 1.2	11931.2 ± 0.6
11965.3 ± 1.2	11964.7 ± 0.8
11992.9 ± 1.2	11988.0 ± 0.3
12019.0 ± 1.2	12015.2 ± 0.8
12051.8 ± 1.2	12049.4 ± 0.7

Table 6.6: Measured excitation energies corresponding to ^{23}Na + p resonances below E_{cm} = 400 keV, from the present study, compared to the latest compilation [End90a]. The [End90a] values have not been corrected for the Audi & Wapstra 1995 mass update.

E_x (keV)	E_{cm} (keV)	E_{lab} (keV)	J^π
11698 ± 1	5	5	4^+
11831 ± 2	138	144	?
11862.4 ± 0.9	169.5	176.9	1^-
11933.6 ± 0.4	240.7	251.2	(2-4)
11966.9 ± 0.5	274.0	285.9	2^+
11988.3 ± 0.3	295.4	308.2	2^+
12017.4 ± 0.5	324.5	338.6	3^-
12051.6 ± 0.5	358.7	374.3	4^+

Table 6.7: Adopted excitation energies for $^{23}\mathrm{Na} + p$ resonances observed in this work. The values consist of a weighted average of previous data, adjusted for any changes in masses [Aud95], and the present results.

Previous ^{24}Mg studies include $^{12}\mathrm{C}(^{16}\mathrm{O}, \alpha)^{24}\mathrm{Mg}$ [Bra72], $^{20}\mathrm{Ne}(\alpha, \gamma)^{24}\mathrm{Mg}$ [Fif78, Sch83], $^{23}\mathrm{Na}(p, \gamma)^{24}\mathrm{Mg}$ [Uhr85, Gör89, End90b], $^{23}\mathrm{Na}(p, \alpha)^{20}\mathrm{Ne}$ [Zys81, Gör89], and $^{24}\mathrm{Mg}(p, p')^{24}\mathrm{Mg}$ [Mos76]. With the change in masses as reflected in [Aud95], the Q-values for several of these reactions have changed significantly since the experiments were performed. The existing data that have contributed to the values as tabulated by Endt has been re-examined with the newer Q-values taken into account. The excitation energies obtained from a weighted average of all existing data (including the present results) are shown in Table 6.7 along with the center-of-mass and lab energies of the protons involved in the $^{23}\mathrm{Na}(p, \gamma)^{24}\mathrm{Mg}$ reaction. Only resonances from (p, γ) threshold to $E_{cm} \leq 400$ keV are tabulated. The new Q-value for the (p, γ) reaction is $Q = 11692.9 \pm 0.3$ keV [Aud95].

Cross sections were calculated for the states observed. The angular distributions of these states, along with the results of the DWBA analysis, are shown in Figure 6.8. The optical model parameters listed in Table 6.3 were used for these calculations. Based on known J^π values or ranges and the shape of the angular distribution, possible values of l_p values are determined. For reasons of clarity, the plots show fits only for selected l_p values.

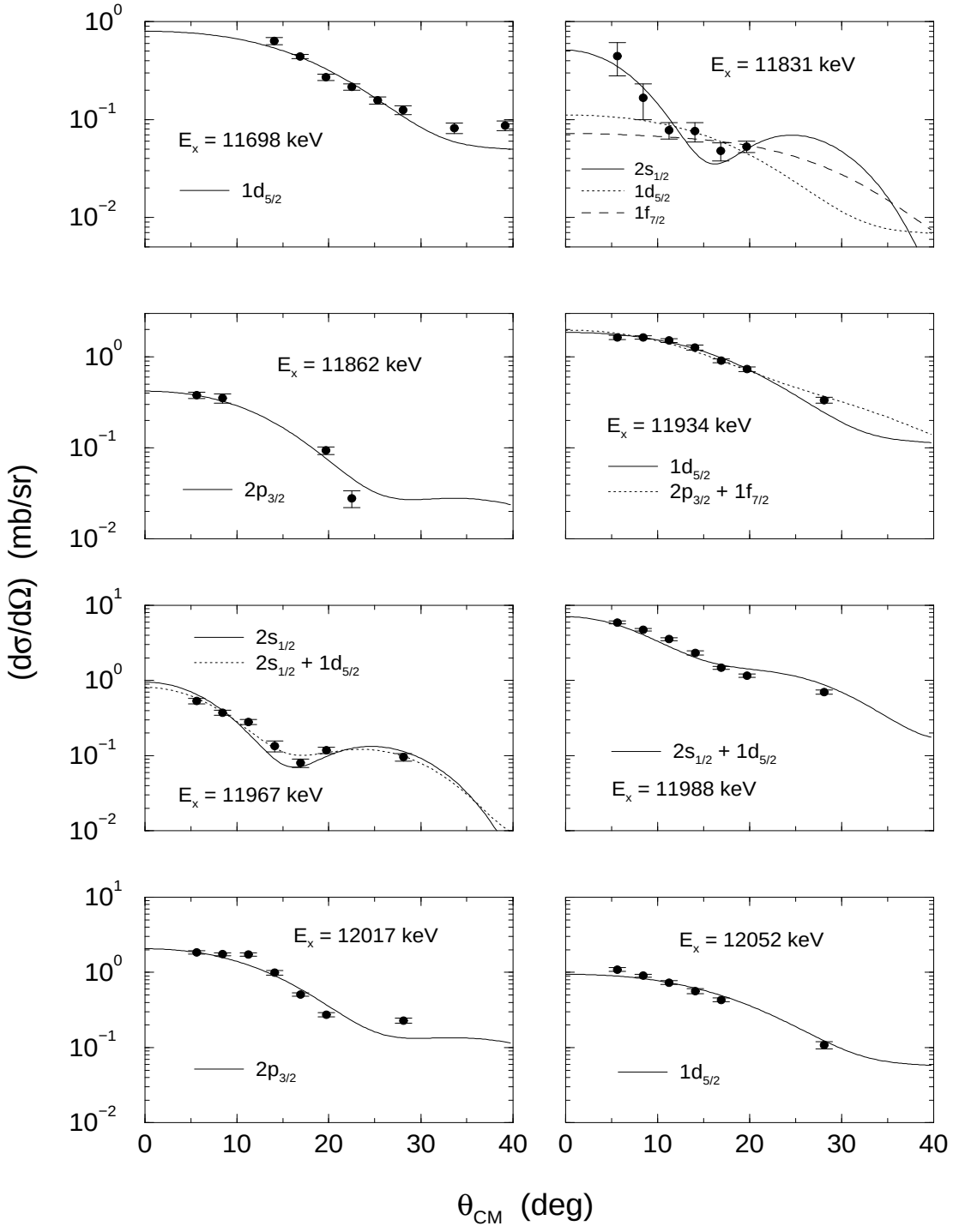

Figure 6.8: Angular distributions and DWBA fits for the states of interest in ^{23}Na(^{3}He, d)^{24}Mg. The angular momentum transfer is noted for each fit, though only selected curves are plotted for reasons of clarity. Energies noted are from the present study.

The state at 11698 keV is clearly observed at multiple angles, but is only unbound by 4 keV, which leads to computational problems in the evaluation of the single particle proton width by DWUCK4. The fit of the calculations to the data for the $l = 2$ and $l = 4$ transfers was tested for two conditions to verify its accuracy: 1) the cross section was evaluated for the state as it exists at 4 keV above threshold and 2) as a fictitious state with the same quantum numbers but bound by 10 keV. The scaling of the calculated cross sections agrees in these two cases to better than 0.05%, as expected, since there is a smooth transition across the (p, γ) threshold. The value of Γ_{sp} needs to be obtained in a different manner, however, because of computational difficulties. The method for obtaining Γ_{sp} is described in Section 6.5.1.

The resulting values of $(2J_f + 1)C^2S$ and $(2J_f + 1)\Gamma_p$ are presented for these states in Section 6.5. Estimates of the uncertainties are also shown there.

6.5 Results and Uncertainties for $^{23}\mathrm{Na}(p,\gamma)^{24}\mathrm{Mg}$ Resonances

6.5.1 C^2S, Γ_p Values, and $\omega\gamma$ Values

Values of $(2J_f + 1)C^2S$ and $(2J_f + 1)\Gamma_p$ for the states discussed in Section 6.4 are shown in Table 6.8. The single-particle proton widths calculated by DWUCK4 were used for all states, with the exception of the state at 11698 keV. To determine the single-particle proton width, Γ_{sp} was calculated for the same quantum numbers as the 11698-keV state, but over a large range of final-state energies (11698 keV to 12808 keV). Plotting the values of Γ_{sp} versus E_{cm}, as in [Ili96], produces the linear relationship shown in Figure 6.9. The value at 5 keV can then be read off for each of the two possible l-transfers. The values obtained for this case are $\Gamma_{sp} = 1.5 \times 10^{-59}$ eV for a $1d_{5/2}$ transfer and 4.8×10^{-66} eV for a $1g_{9/2}$ transfer. These are then used to determine the values of $(2J_f + 1)\Gamma_p$.

Because the states of interest in ^{24}Mg have open proton, alpha, and γ-ray channels, they can be observed as (p,γ), (p,α), or (α,γ) resonances. In addition, the branching ratio for γ emission, Γ_γ/Γ, has been directly measured for some of these states. For a known spin, the combination of resonance strengths, total width, or Γ_γ/Γ can be used to deduce the values of Γ_α, Γ_γ and Γ_p. For six of the states that are observed in this work below E_{cm} = 400 keV (E_x = 11862, 11934, 11967, 11988, 12017, and 12052 keV) enough information exists so that Γ_p can be calculated. These values are then compared to the results from the present analysis, as shown in Table 6.9. The agreement is generally within a factor of two, as also seen in the ^{22}Ne analysis.

The 11831 keV state has an unknown J^π value. The present angular distribution shows that there can be a pure l=0 contribution, which would correspond to $J^\pi = (1,2)^+$. This conclusion is heavily based on the first two data points in the angular distribution. The lowest angle cross section is determined under the approximation that the nitrogen content in the target during the 5° run was the average of that during the 7.5° and 10° runs with an uncertainty in that content

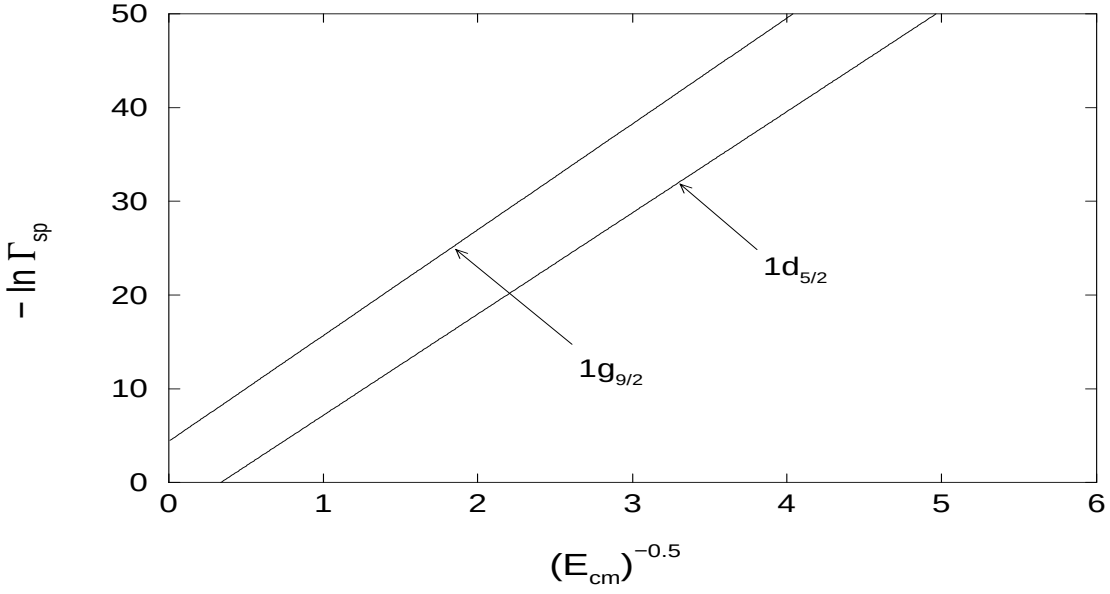

Figure 6.9: Γ_{sp} versus E_{cm} for (nlj) values appropriate for the 11698-keV state. The widths and energies are in MeV.

E_x (keV)	J^π	l	Q^2	$(2J_f + 1)C^2S$	$(2J_f + 1)\Gamma_p$ (eV)
11698	4^+	2	4.9	0.11	1.6×10^{-54}
		2 + 4	4.6	0.097 + 0.043	$1.4 \times 10^{-54} + 2.0 \times 10^{-61}$
11831	?	0	1.6	0.040	7.4×10^{-5}
		2	1.6	0.015	1.3×10^{-7}
		0 + 2	1.1	0.021 + 0.0079	$3.8 \times 10^{-5} + 6.4 \times 10^{-8}$
		1	3.3	0.011	4.2×10^{-6}
		3	2.0	0.024	2.5×10^{-9}
		1 + 3	1.8	0.0039 + 0.016	$1.5 \times 10^{-6} + 1.7 \times 10^{-9}$
11862	1^-	1	4.4	0.026	1.6×10^{-4}
11934	(2-4)	2	3.4	0.25	2.5×10^{-3}
		0 + 2	3.7	0.021 + 0.24	$4.0 \times 10^{-2} + 2.4 \times 10^{-3}$
		1 + 3	2.1	0.085 + 0.20	$3.6 \times 10^{-2} + 3.2 \times 10^{-5}$
		2 + 4	1.9	0.23 + 0.13	$2.3 \times 10^{-3} + 1.4 \times 10^{-7}$
11967	2^+	0	5.5	0.084	0.60
		0 + 2	2.9	0.064 + 0.012	$0.46 + 4.9 \times 10^{-4}$
11988	2^+	0 + 2	14.5	0.42 + 0.33	6.2 + 0.029
12017	3^-	1	17.1	0.13	1.1
12052	4^+	2	4.3	0.13	0.076

Table 6.8: $(2J_f + 1)C^2S$ and $(2J_f + 1)\Gamma_p$ values for states in ^{23}Na(^{3}He, d)^{24}Mg corresponding to ^{23}Na + p resonances for $E_{cm} \leq 400$ keV.

of $\approx 25\%$ from the observations at the two angles. Thus, it is the most suspect point in the angular distribution. The state is not so weak that a direct reaction is ruled out. For the case of pure $l = 0$ transfer, $(2J_f + 1)\Gamma_p = 7.4 \times 10^{-5}$ eV. Vermeer *et al.*, found a ratio of $\Gamma_\gamma/\Gamma = 0.95 \pm 0.04$. Thus, the resonance strength is 8.8×10^{-6} eV. Görres *et al.* measured the resonance directly [Gör89] and found an upper limit of 5×10^{-6} eV. The present value is not inconsistent with this upper limit, with the (^{3}He, d) uncertainties. The upper limit quoted by EEC95 for a maximum spin of J = 2 is 1.4×10^{-9} eV, assuming a ratio of $\Gamma_\gamma/\Gamma = 1$ and a proton partial width of $\Gamma_p \leq 2.3 \times 10^{-9}$ eV. This value is much lower than our present value and appears to be erroneous [Cha99].

E_x (keV)	E_{cm} (keV)	J^π	$(2J_f + 1)\Gamma_p$ Present	$(2J_f + 1)\Gamma_p$ [End90a]
11862.4	169.5	1^-	160 μeV	210 μeV
11933.6	240.7	(2-4)	2.5 meV[a]	4.2−6.1 meV[b]
11966.9	274.0	2^+	0.46 eV	0.31 eV
11988.3	295.4	2^+	6.2 eV	1.3 eV
12017.4	324.5	3^-	1.1 eV	0.77 eV
12051.6	358.7	4^+	76 meV	41 meV

[a] From $l = 2$ transfer.

[b] Using $\Gamma_\gamma/\Gamma > 0.7$ from Vermeer *et al.* [Ver88].

Table 6.9: Comparison of $(2J_f + 1)\Gamma_p$ for 6 states below $E_{cm} = 400$ keV in ^{23}Na + p.

A rough estimate of a lower limit can be found by ignoring the 5° cross section and inspecting the DWBA fits. The $l = 3$ prediction drops below the 7.5° data point while the $l = 2$ prediction still maintains a reasonable fit to the remaining data. Thus, as a tentative lower limit of the strength of the 11831-keV state, a pure $l = 2$ transfer is adopted which results in $(2J_f + 1)\Gamma_p = 1.3 \times 10^{-7}$ eV. This gives a resonance strength of 1.5×10^{-8} eV. The ratio of the resonance strength upper limit to the lower limit is roughly 600.

The Γ_γ/Γ value for the 11698-keV state has also been measured by Vermeer *et al.* With a pure l=2 transfer, the proton partial width is 1.8×10^{-55} eV. Combining this with the value $\Gamma_\gamma/\Gamma = 0.08 \pm 0.03$, the resonance strength is $\omega\gamma = 1.6 \times 10^{-56}$ eV. This is completely negligible in the total reaction rate.

There are 4 states below $E_{cm} = 400$ keV which were not observed in the present study. Their influence is discussed below.

The state at 11730 keV was investigated by running appropriate DWBA calculations to obtain the single-particle proton width. The J^π value is 0^+, so the only possible transfer is $l = 2$. For a $1d_{5/2}$ transfer, a value of $\Gamma_{sp} = 1.6 \times 10^{-17}$ eV was found. Using the value of C^2S estimated by EEC95 of $\leq$0.6, the

upper limit is $\Gamma_p \leq 9.8 \times 10^{-18}$ eV. With the values of $\Gamma_\alpha = 10$ keV and $\Gamma_\gamma = 0.35$ eV [End90a], the resonance strength is given by $\omega\gamma \leq 4.3 \times 10^{-23}$ eV. This value is slightly higher than in EEC95, reflecting the slightly higher resonance energy from the new Q-value and excitation energy.

The high spin (6^+, 7^-, 8^+) state at 11860 keV can only be formed by partial waves $l \geq 4$, so its contribution to the (p,γ) reaction will be negligible.

Görres *et al.*, have measured the (p,α) resonance strength for the state at 11910 keV and found a value of $(\omega\gamma)_{(p,\alpha)} = 7.0 \times 10^{-5}$ eV [Gör89]. The width is known to be $\Gamma \approx \Gamma_\alpha = 5.5$ keV [Fif78]. The (p,γ) strength will be weaker by the ratio $\Gamma_\gamma/\Gamma_\alpha \approx 1/5500$, assuming a Γ_γ width on the order of 1 eV. This results in a (p,γ) strength on the order of 1×10^{-8} eV.

The state at 12002 keV is also negligible because of its $J^\pi = 6^+$ value.

The adopted values of $\omega\gamma$ are given in Table 6.10. The effect of the new $\omega\gamma$ values will be discussed in Section 7.1. Those not explicitly discussed here have been taken from the existing data.

6.5.2 Uncertainties

The investigation of uncertainties in C^2S values for the ^{23}Na(^{3}He, d)^{24}Mg reaction will follow the same structure as was described for the ^{22}Ne(^{3}He, d)^{23}Na reaction discussed in Section 5.5.2.

The dependence of Γ_{sp} on the integration controls (step size and cut-off radius) was tested and a variation of $< 5\%$ was found.

The finite-range (FR) correction and non-locality (N-L) corrections were tested by turning them on and off both simultaneously or one at a time for the 11967 ($l = 0 + 2$) keV state. The range of C^2S was found to decrease with increasing l-transfer, from 30% at $l = 0$ to 18% at $l = 2$. The fit-test parameter Q^2 did not change significantly with these changes, as seen in Figure 6.10. Again, without any justification to do otherwise, the corrections are left on throughout the analysis of the ^{23}Na(^{3}He, d)^{24}Mg data.

E_x (keV)	E_{cm} (keV)	J^π	$\omega\gamma$ (eV)
11698	5	4^+	1.6×10^{-56}
11730	37	0^+	$\leq 4.3 \times 10^{-23}$
11831	136	?	$\leq 8.8 \times 10^{-6}$
			$\geq 1.5 \times 10^{-8}$
11860	167	$(6^+,7^-,8^+)$	negligible
11862.4	169.5	1^-	1.4×10^{-9}
11910	217	N	$\approx 1 \times 10^{-8}$
11933.6	240.7	(2-4)	5.3×10^{-4}
11966.9	274.0	2^+	2.6×10^{-6}
11988.3	295.4	2^+	0.12
12002	309	6^+	negligible
12017.4	324.5	3^-	4.0×10^{-5}
12051.6	358.7	4^+	1.4×10^{-3}

Table 6.10: Adopted $\omega\gamma$ values for $^{23}\mathrm{Na}(p,\gamma)^{24}\mathrm{Mg}$.

The effect of statistical errors in the $(^3\mathrm{He}, d)$ fit was tested using the 11967-keV state. The overall error was found to be 6%. The statistical error from the fit of the elastic scattering data was 2.5%.

The final-state parameters were again tested using the sets of [Ili97] and the more conventional values. There was no noticeable effect of this change ($\leq 1\%$). While varying r_r and a_r by up to 10%, large variations were again noticed in individual C^2S and Γ_{sp} values. The changes in the two parameters offset each other producing changes in Γ_p of $\leq 7\%$.

The effect of changing the optical model parameters was investigated using the 11862 keV state. The results of the ^{3}He and d parameter tests are shown in Figure 6.11. The difference between the two sets of optical models was integrated from 0° to 20°. The ^{3}He variation was done while using the d and p parameters listed in Table 6.3 with the two ^{3}He parameter sets from Table 6.1. Integrating

the average difference between the two predictions from 0° to 20° results in an error of 26% in C^2S, but this is presumably larger for the 11831-keV state due to the sensitivity of the fit to the first two data points in the angular distribution.

The d variation was performed using the ^{3}He and p parameters listed in Table 6.3 with the d parameter sets coming from both Daehnick's predictions (also in Table 6.3) and from [Cha89], as tabulated in Table 5.10. Again integrating the average difference between the two predictions over the 0° to 20° range gives an error of 11%, as in the ^{22}Ne(^{3}He, d)^{23}Na study.

The contributions to the errors on C^2S are given in Table 6.11. Treating these errors as independent, results in a total error in C^2S of 29%. Errors in Γ_p are again seen to be accurate to within a factor of ≈ 2, from the comparison of the unbound calibration states to the data from ^{24}Mg$(p,p)^{24}$Mg of Vanhoy *et al.* [Van87] shown in Table 6.5, as well as from comparison shown in Table 6.9.

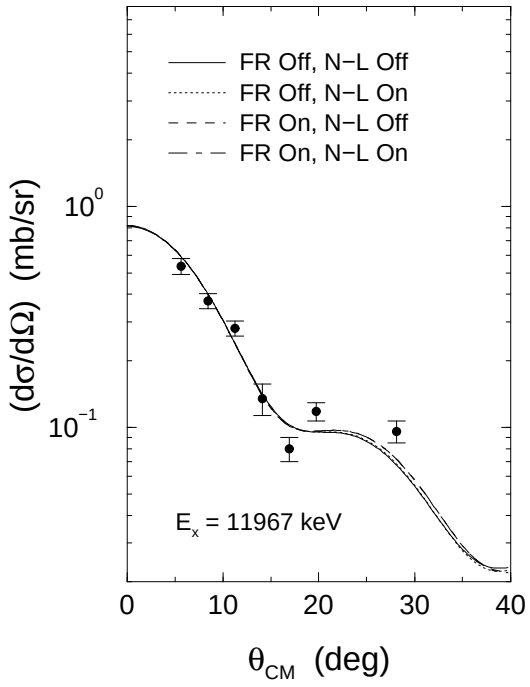

Figure 6.10: Test of the effects of turning the finite-range (FR) and non-locality (N-L) corrections on and off for the 11967 keV state (l = 0+2). The change in the Q^2 of the fit was negligible.

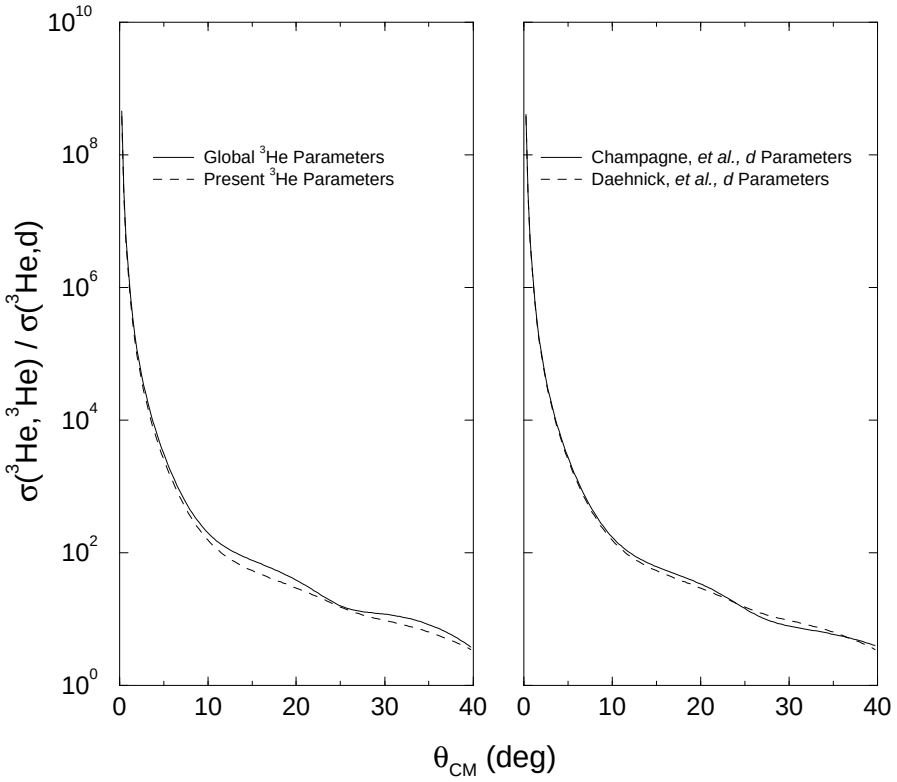

Figure 6.11: Optical model potential parameter test for entrance and exit channels of ^{23}Na(^{3}He, d)^{24}Mg. The effects have been investigated for the 12670-keV state, with an l-transfer of 2.

Source of Error	Nature of Error	% Error of C^2S
(^{3}He, d) Fit	Statistical	6.0
Elastic Data Fit	Statistical	2.5
^{3}He OMP	Systematic	26
d OMP	Systematic	11
p OMP	Systematic	≤ 1.0

Table 6.11: Sources of error for C^2S in ^{23}Na(^{3}He, d)^{24}Mg. The errors should be independent.

Chapter 7

Astrophysical Implications

7.1 Reaction Rates

The reaction rate $N_A \langle \sigma v \rangle$ is calculated for the two (p, γ) reactions studied in this work using the resonance parameters listed in Tables 5.9 and 6.10. Comparison is made to the compilation of EEC95. The new values for Γ_p for ^{24}Mg states are also applied to the ^{23}Na$(p, \alpha)^{20}$Ne reaction rate.

7.1.1 ^{22}Ne$(p, \gamma)^{23}$Na

No new strengths are determined for the resonances above E_{cm}=151 keV. The resonance strengths that have changed are shown in Table 7.1 in comparison with the values of EEC95.

	$\omega\gamma$ (eV)	
E_{cm} (kev)	EEC95	Present
35.4	7.5×10^{-15}	4.7×10^{-15}
68	$\leq 2.0 \times 10^{-9}$	$\leq 2.0 \times 10^{-10}$
100	$\leq 6.1 \times 10^{-7}$	$\leq 1.4 \times 10^{-7}$
151	1.8×10^{-7}	1.1×10^{-8}

Table 7.1: Strength comparison for important resonances in ^{22}Ne$(p, \gamma)^{23}$Na.

The upper limits on the strengths of the possible resonances at 68 and 100 keV drop by a factor of 10 and 4, respectively. Because the strength of the 151-keV resonance is decreased by an order of magnitude, the current upper limit for the 178-keV resonance becomes larger than that for the 151-keV resonance at a temperature near $T_9 = 0.060$. Above a temperature of $T_9 = 0.085$, the 178-keV resonance becomes larger than the direct capture component. This is at the upper end of the temperature region of interest for this study. The contribution from direct capture is adopted from EEC95, as is the effect of resonances higher than E_{cm}=178 keV. With the large number of resonances that contribute to the reaction rate at the temperatures of interest for red giant hydrogen-burning shells, the tails of resonances do not significantly influence the reaction rate, and are thus neglected.

The present reaction rate for $T_9 = 0.01$ - 0.10 is given by

$$\begin{aligned} N_A \langle \sigma v \rangle &= 1.05 \times 10^9 \, {T_9}^{-2/3} \exp(-19.431/{T_9}^{1/3}) \\ &+ 7.74 \times 10^{-10} \, {T_9}^{-3/2} \exp(-0.411/T_9) \\ &+ 1.81 \times 10^{-3} \, {T_9}^{-3/2} \exp(-1.752/T_9) \\ &+ 9.30 \times 10^4 \, {T_9}^{-1.174} \exp(-5.100/T_9) \\ &+ 5.71 \times 10^5 \, {T_9}^{-0.249} \exp(-7.117/T_9) \\ &+ [0-1] \, 3.3 \times 10^{-5} \, {T_9}^{-3/2} \exp(-0.789/T_9) \\ &+ [0-1] \, 0.0230 \, {T_9}^{-3/2} \exp(-1.161/T_9) \\ &+ [0-1] \, 0.428 \, {T_9}^{-3/2} \exp(-2.066/T_9) \\ &\text{cm}^3 \text{ mole}^{-1} \text{ sec}^{-1}. \end{aligned} \tag{7.1}$$

The first three terms represent the direct capture, 35.4-keV resonance, and 151-keV resonance contributions, respectively. The next two terms represent the resonances above 178 keV. The last three terms represent the upper limit contributions from the 68-, 100-, and 178-keV resonances, respectively. The total reaction rate and the individual contributions are shown in Figure 7.1. The un-

certainty betwen the upper and lower limit grows from a factor of 1.1 at T_9 = 0.03 to a factor of approximately 1800 at T_9 = 0.09. This is dominated by the influence of the possible resonances at 68 and 100 keV. The uncertainty caused by the 178-keV resonance as given in Equation 7.1 is only a factor above T_9 = 0.09, which is far above the temperatures reached in red giant hydrogen-burning shells.

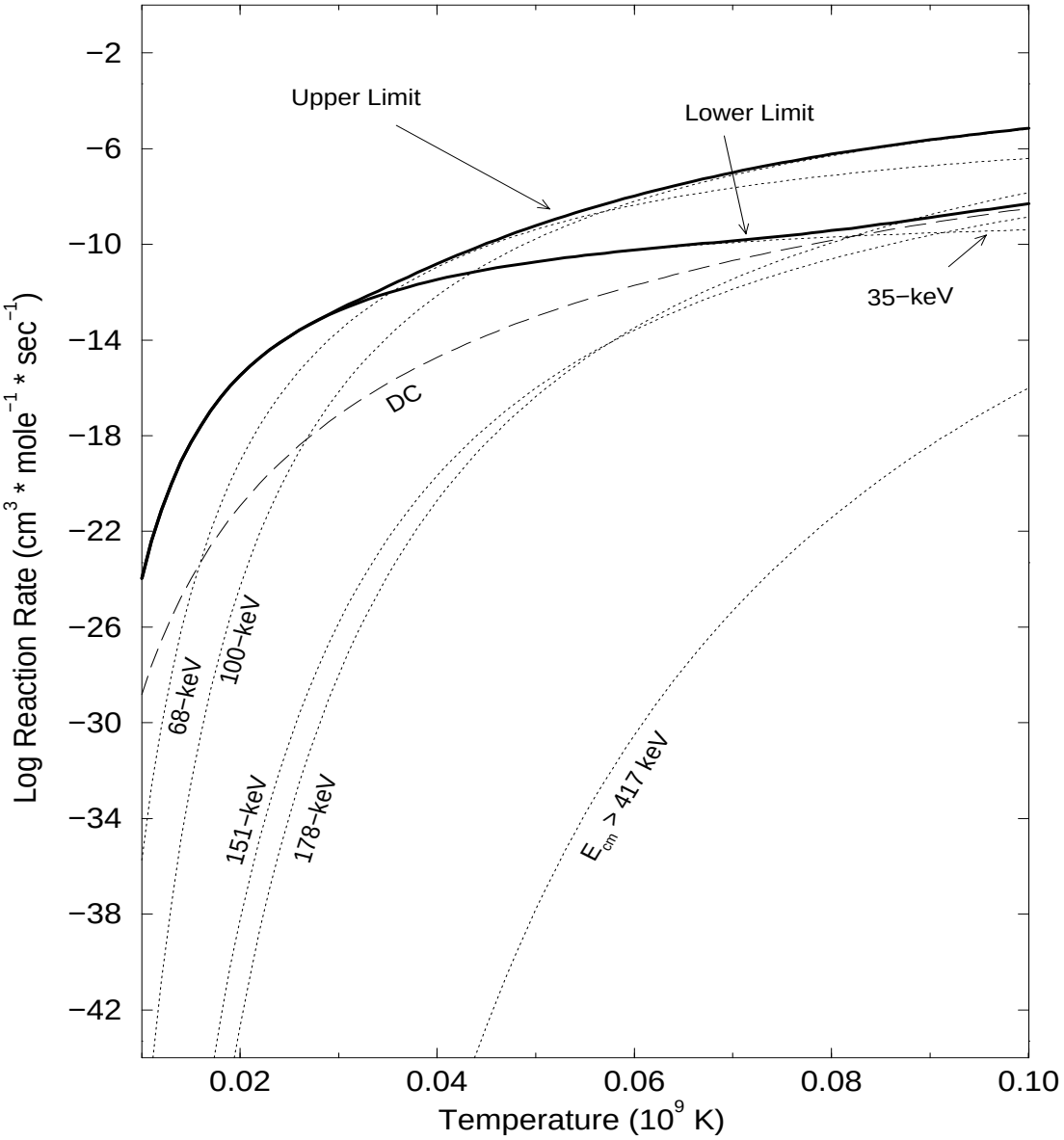

Figure 7.1: New reaction rate for ^{22}Ne$(p,\gamma)^{23}$Na. Individual contributions are labelled by their CM resonance energies.

The change in the reaction rate from the EEC95 compilation is shown in Figure 7.2. With the reduction in the strengths of the 68- and 100-keV resonances, the upper limit has dropped between a factor of 1.5 and a factor of 8 across the temperature region of interest. The revision of the contribution from the 151-keV resonance reduces the lower limit a factor of 1.3-1.5 across the temperature region of interest, and up to a factor of 5 at $T_9 = 0.1$. The present upper limit on the reaction rate is compared to the previous upper limit in Figure 7.3.

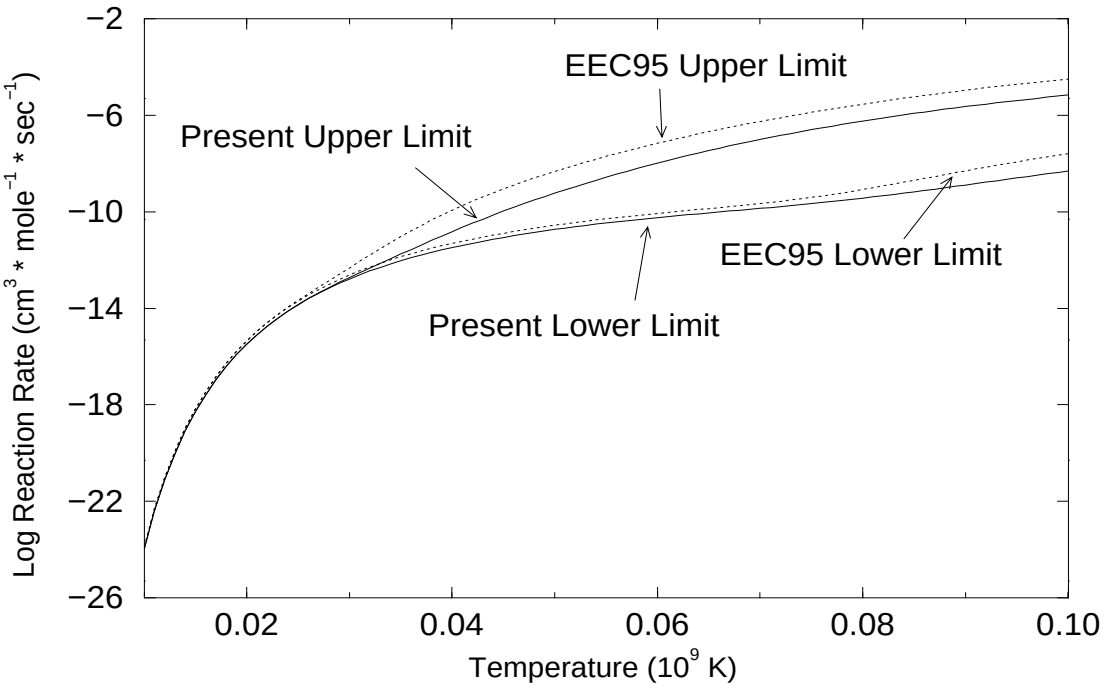

Figure 7.2: Comparison of $^{22}\mathrm{Ne}(p,\gamma)^{23}\mathrm{Na}$ reaction rate to EEC95. The individual upper and lower limits are indicated.

7.1.2 $^{23}\mathrm{Na}(p,\gamma)^{24}\mathrm{Mg}$

The only resonance strength that has changed significantly since the compilation of EEC95 is that of the 138-keV resonance. However the change is very dramatic. The resonance strength now is limited between the values of 8.8×10^{-6} eV and 1.5×10^{-8} eV. The value as given in EEC95 is 1.4×10^{-9} eV. The resonance energies have changed slightly because of the change in mass val-

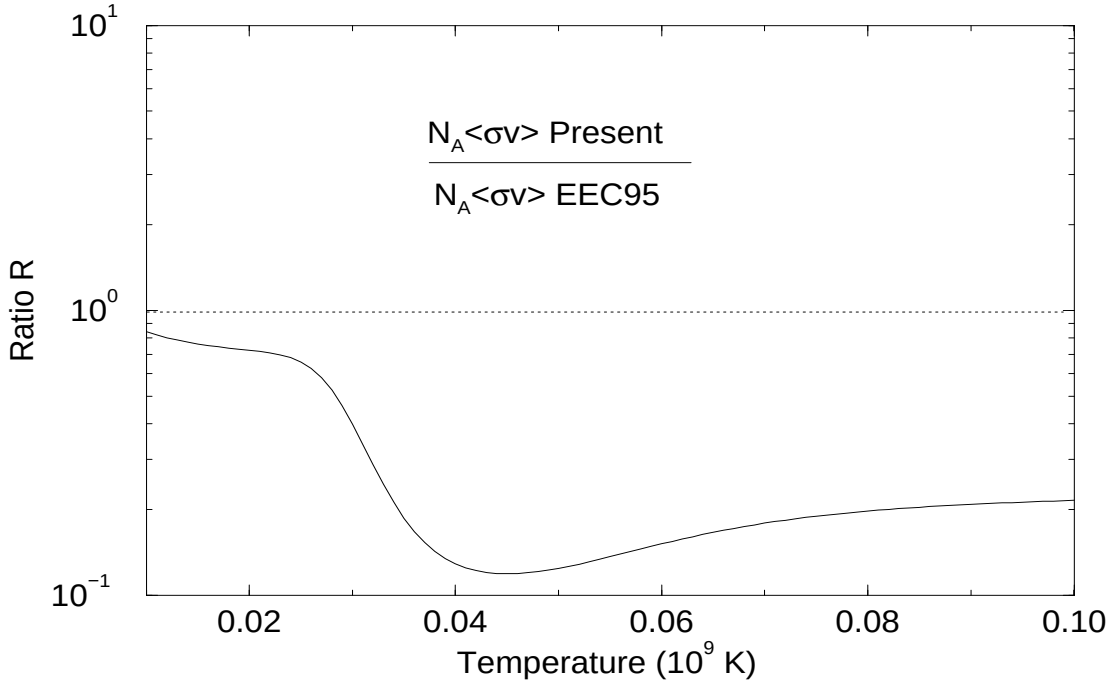

Figure 7.3: Ratio of present upper limit to EEC95 upper limit for ^{22}Ne$(p,\gamma)^{23}$Na.

ues. There is a slight increase in the resonance strength upper limit for the 37-keV resonance over the EEC95 value because of the changes in Q-value and the excitation energy. The ratio of the present resonance strength upper limit to that of EEC95 is 2, within the error of the current method. The direct capture contribution has been adopted from EEC95.

The present reaction rate for $T_9 = 0.01$ - 0.10 is given by

$$\begin{aligned} N_A \langle \sigma v \rangle \;=\; & 2.47 \times 10^9 {T_9}^{-2/3} \exp(-20.758/{T_9}^{1/3}) \\ & + [0-1]\, 7.06 \times 10^{-18}\, {T_9}^{-3/2} \exp(-0.429/T_9) \\ & + [1-585]\, 0.00246\, {T_9}^{-3/2} \exp(-1.601/T_9) \\ & + 87.0\, {T_9}^{-3/2} \exp(-2.797/T_9) \\ & + 1.97 \times 10^4\, {T_9}^{-3/2} \exp(-3.423/T_9) \\ & + 3.44 \times 10^4\, {T_9}^{0.323} \exp(-5.219/T_9) \\ & \text{cm}^3 \text{ mole}^{-1} \text{ sec}^{-1}. \end{aligned} \tag{7.2}$$

The first term represents the direct capture contribution. The next four are

the contributions from the 37-, 138-, 241-, and 295-keV resonances respectively. The last term describes the contribution from resonances above E_{cm} = 296 keV, as computed in EEC95. Resonance tails do not contribute significantly to the reaction rate, again because of the preponderance of resonances in the region of interest.

The overall reaction rate and the individual contributions are shown in Figure 7.4. The 138-keV resonance dominates the uncertainty in $N_A \langle \sigma v \rangle$ for temperatures from $T_9 = 0.04$ to above the region of interest for red giant hydrogen burning shells. The uncertainty of this resonance strength is roughly a factor of 600 based on the analysis described in Section 6.5.1. At the upper limit, a direct (p, γ) measurement of this particular resonance seems feasible and would reduce the present uncertainty. The effect of this resonance strength uncertainty grows from a factor of 2 at $T_9 = 0.036$ to a factor of 518 by $T_9 = 0.07$, at the upper end of the current region of interest.

The change in the reaction rate from the EEC95 compilation is shown in Figure 7.5. The present reaction rate upper limit is compared to the previous upper limit in Figure 7.6.

7.1.3 ^{23}Na$(p, \alpha)^{20}$Ne

As was the case for the ^{23}Na$(p, \gamma)^{24}$Mg reaction, the only changes that we recommend for the resonance strengths for the ^{23}Na$(p, \alpha)^{20}$Ne reaction are for the 37- and 138-keV resonances. The upper limit of the 37-keV resonance strength is a factor of 2 higher than that in EEC95. For the 138-keV resonance, since Vermeer *et al.* found a ratio of $\Gamma_\gamma/\Gamma = 0.95 \pm 0.04$, an upper limit (at the 61% confidence level) on the branching ratio of the alpha emission can be set at $\Gamma_\alpha/\Gamma = 0.09$. The branching ratio for proton emission is negligible. With the current upper limit of $(2J_f + 1)\Gamma_p = 7.4 \times 10^{-5}$ eV, the (p, α) resonance strength has an upper limit of 8.3×10^{-7} eV. Using our measurement for Γ_p, the lower limit for $(\omega\gamma)_{(p,\alpha)}$ is 1.4×10^{-9} eV. The value presented in EEC95 was 1.4×10^{-9}

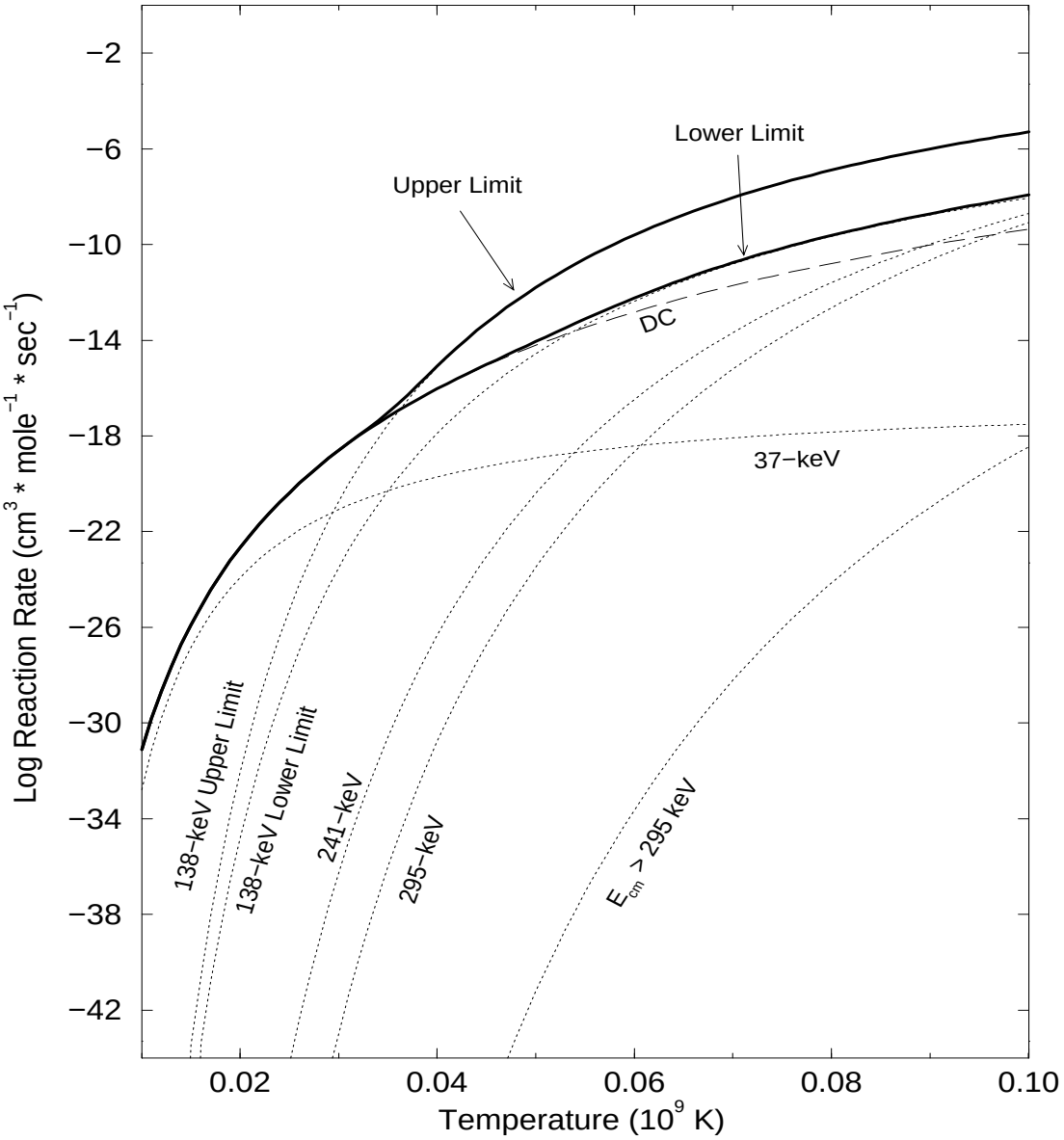

Figure 7.4: New reaction rate for ^{23}Na$(p,\gamma)^{24}$Mg. Individual contributions are labelled by their CM resonance energies.

eV. The contributions from the tails of higher energy resonances and from higher energy resonances are taken from EEC95. The current reaction rate limits are shown in Figure 7.7, along with the individual contributions. The ratio of the present reaction rate to that of EEC95 is shown in Figure 7.8.

The uncertainty in the rate is from the 37-keV resonance up to a temperature of $T_9 \approx 0.04$. Above that value, the 138-keV resonance uncertainty becomes

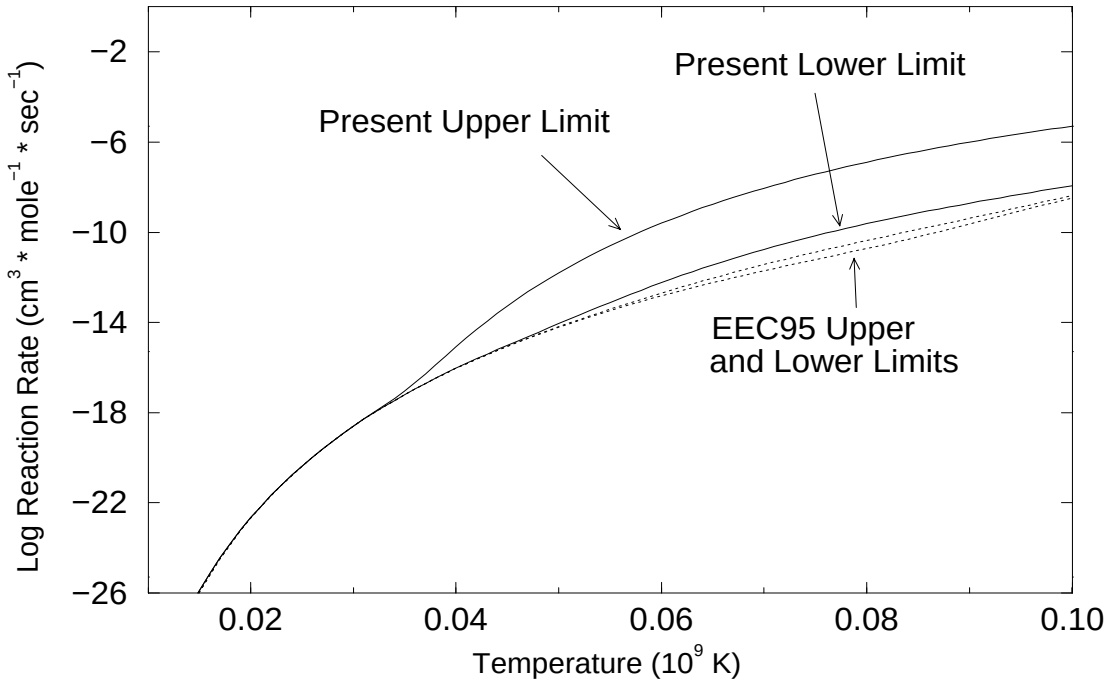

Figure 7.5: Comparison of $^{23}\mathrm{Na}(p,\gamma)^{24}\mathrm{Mg}$ reaction rate to EEC95. The limits from EEC95 are indicated.

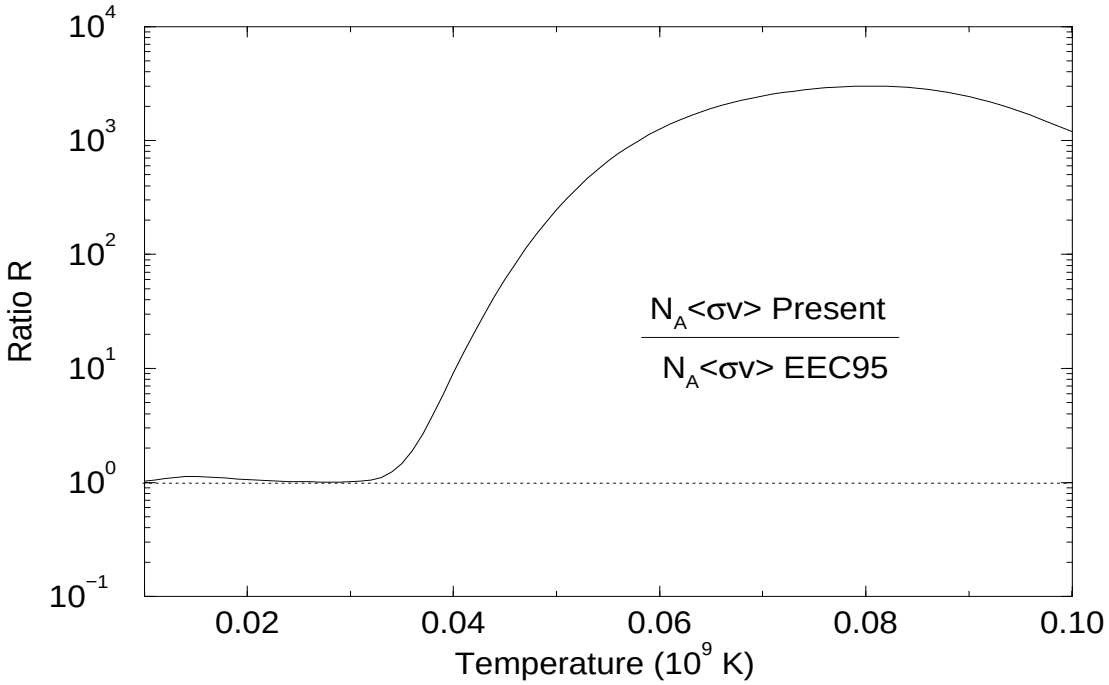

Figure 7.6: Ratio of present upper limit reaction rate to EEC95 upper limit for $^{23}\mathrm{Na}(p,\gamma)^{24}\mathrm{Mg}$.

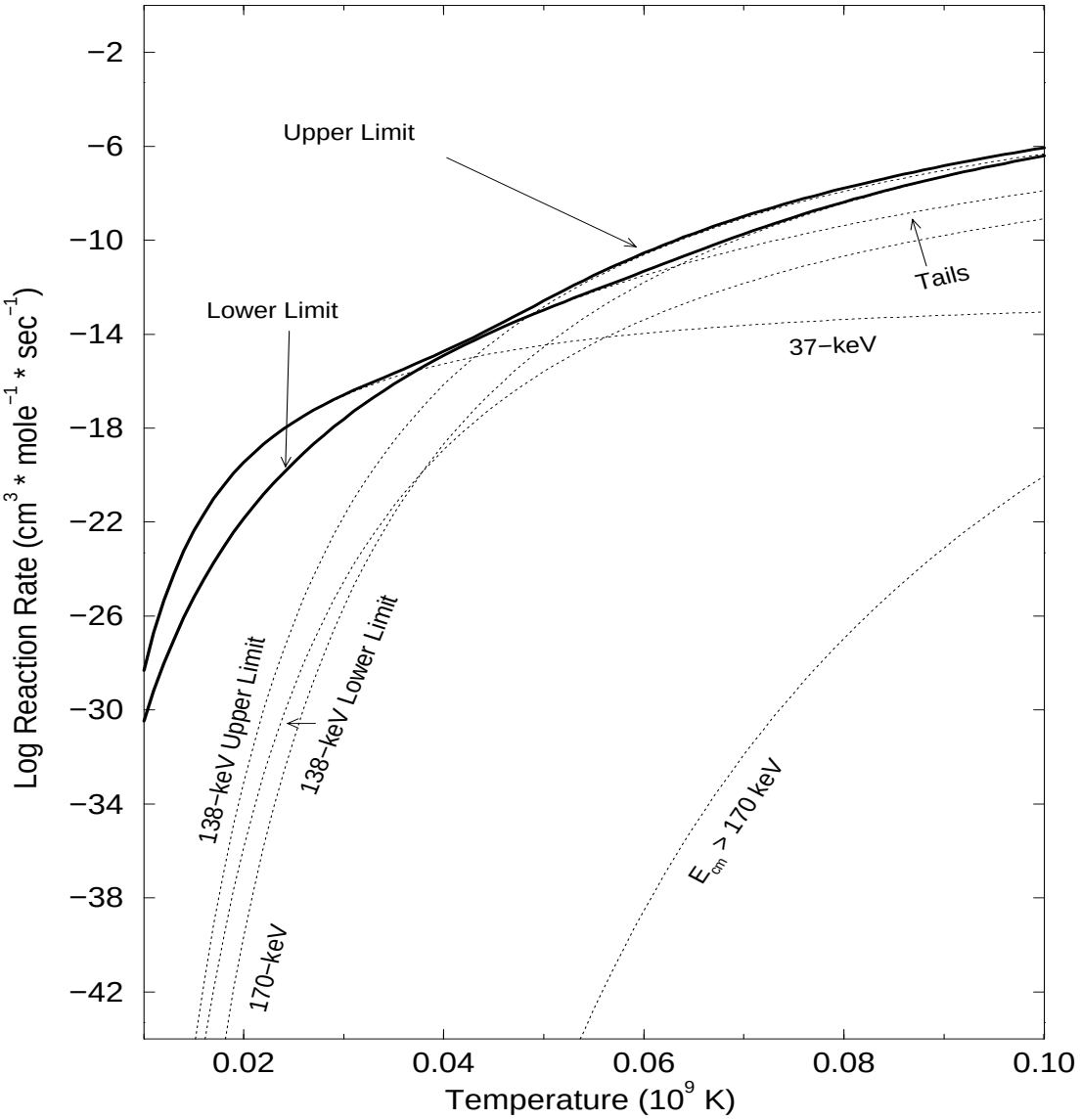

Figure 7.7: New reaction rate for ^{23}Na$(p,\alpha)^{20}$Ne. Individual contributions are labelled by their CM resonance energies.

dominant. The ratio of the current upper limit to the lower limit falls from a factor of 10 at $T_9 = 0.03$ to 1.5 around $T_9 = 0.045$, and then grows to a factor of 6 by $T_9 = 0.07$.

With the dramatic increase in the ^{23}Na$(p,\gamma)^{24}$Mg reaction rate and the moderate increase in the ^{23}Na$(p,\alpha)^{20}$Ne reaction rate (assuming our current upper limits), the temperature range over which the cycle remains closed changes quite

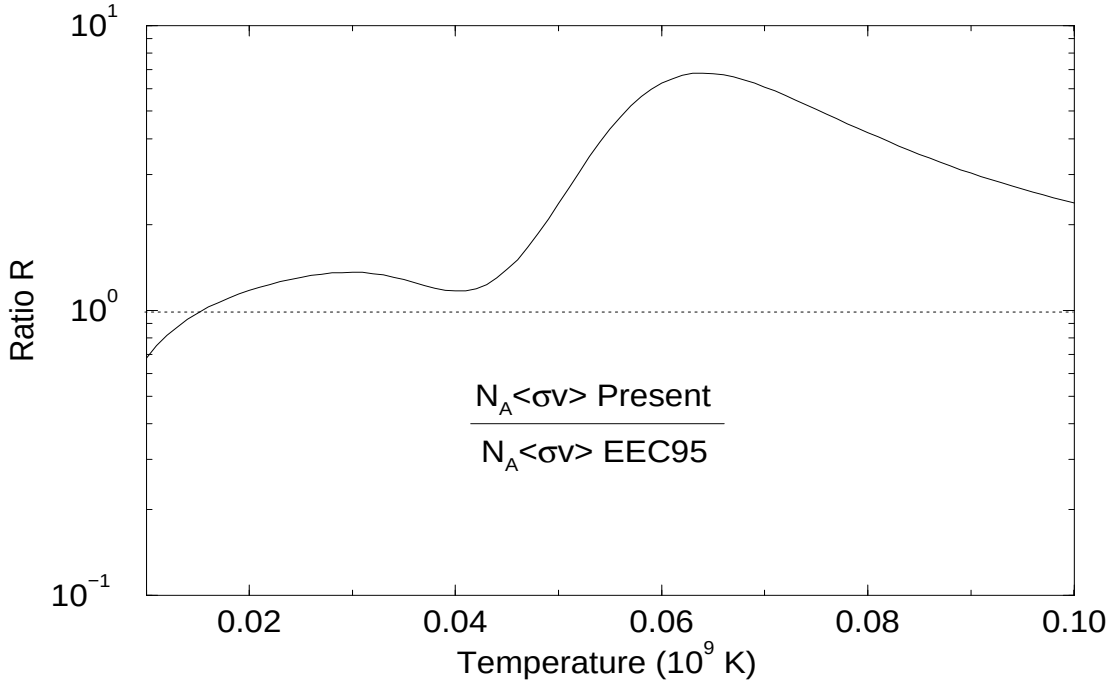

Figure 7.8: Ratio of present reaction rate upper limit to EEC95 upper limit for $^{23}\mathrm{Na}(p,\alpha)^{20}\mathrm{Ne}$.

significantly. The ratio of the leakage reaction to the cycling reaction is shown in Figure 7.9. For the upper limits, above a temperature of $\mathrm{T}_9 = 0.042$, the leakage reaction surpasses the cycling reaction, resulting in a loss of neon and sodium to the MgAl cycle at a much lower temperature than previously thought [Wal97]. The lower limits on the reaction rates still lead to a closed cycle at the temperature of interest in red giant stars.

7.2 Results of Network Calculations

The present reaction rates have been used to determine the abundances of the stable isotopes in the NeNa cycle and the most abundant isotopes in the CNO cycle in an environment characterized by a temperature of $\mathrm{T}_9 = 0.045$ and a density of 100 gm/cm^3. These values are typical of the situation experienced in the hydrogen-burning layer in red giants near the tip of the Red Giant Branch. The initial composition is for $\mathrm{Z} = 10^{-4}$ with the α-elements increased by a factor

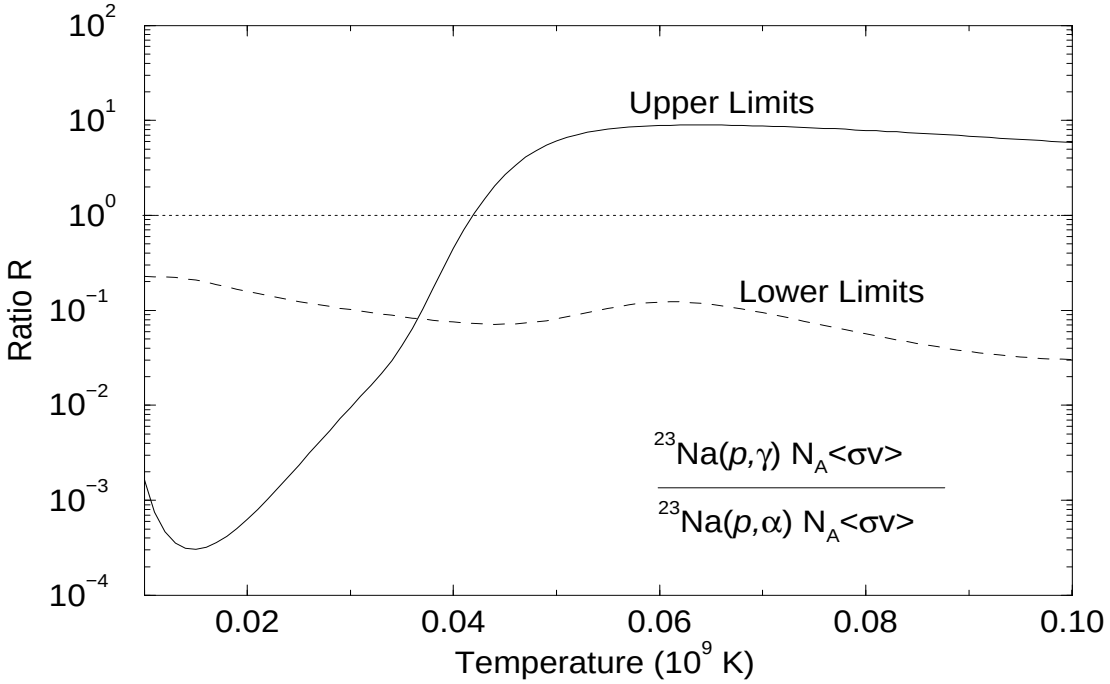

Figure 7.9: Ratio of ^{23}Na$(p,\gamma)^{24}$Mg reaction rate to ^{23}Na$(p,\alpha)^{20}$Ne reaction rate.

of 2.5, as seen in observations (see *e.g.* [Sal93, Car96, Kra98], and references therein). The metallicity chosen was arbitrary, and reflects one of the models studied by Cavallo *et al.* [Cav98] and shown in Section 1.3.

For a particular nucleus i, the total rate of change of the isotopic abundance $\mathrm{Y}_i = \mathrm{X}_i/\mathrm{A}_i$ is given by

$$\frac{dY_i}{dt} = \sum_j \lambda_j Y_j + \sum_{j,k} \rho N_A \langle \sigma v \rangle_{jk} Y_j Y_k, \tag{7.3}$$

where the sums account for all creation and destruction of nucleus i. The first term describes β-decays and photodisintegrations through the decay constant λ_j of nucleus j into nucleus i. The second term describes reactions between the nuclei j and k. Three-particle interactions are also taken into account. The network code solves the resulting coupled differential equations at integration time steps τ, chosen by the requirement that the abundances of nuclei j with $\mathrm{Y}_j \geq \mathrm{Y}_{min}$ vary by less than 25% over the interval τ. The cut-off value of Y_{min} is set at a value of 10^{-10}. The method used is that described by Wagoner [Wag69] and Prantzos *et al.* [Pra87].

The reaction network follows 394 different nuclei from hydrogen to yttrium in the region between the stable isotopes and the proton drip line using 3933 nuclear processes, involving weak interactions, and p-, α-, and γ-ray induced reactions. The reaction rates for the NeNa cycle are taken from EEC95 for ^{20}Ne$(p,\gamma)^{21}$Na and ^{21}Ne$(p,\gamma)^{22}$Na, and from the present study for the remaining reactions. The reactions of ^{23}Na + p are taken as the current upper limits. The remaining reaction rates for the CNO region of interest are from [Cau88].

The network was run until hydrogen was completely depleted. The results for the upper and lower limits on the ^{22}Ne$(p,\gamma)^{23}$Na reaction are shown in Figure 7.10. The vertical line at $\approx 5 \times 10^{11}$ seconds indicates the point at which the available hydrogen has been reduced by 5% from its initial value. This decrease in hydrogen is chosen as a crude approximation to the mixing of envelope material into the proton-capture region of a red giant and ensures that the evolution of the star is not changed significantly by mixing too much fuel into the hydrogen burning shell. The time that it takes to reach this depletion ($\approx 2 \times 10^4$ years) is short compared to the time between the start of convective mixing and the tip of the Red Giant Branch.

The mass fraction of ^{20}Ne appears to suffer almost no depletion until very late in the burning. However, its abundance is much larger than the other NeNa cycle participants, so changes that are not readily noticeable can contribute greatly to enhancements in the other NeNa isotopes. The rate of ^{20}Ne$(p,\gamma)^{21}$Na is slow at $T_9 = 0.045$. The ^{21}Ne$(p,\gamma)^{22}$Na reaction proceeds very quickly. With the slow production of ^{21}Ne, the amount of ^{21}Ne created is equal to the amount destroyed and thus its abundance remains in a steady state until material starts being removed from the cycle by ^{23}Na$(p,\gamma)^{24}$Mg at around 10^{12} seconds. This is seen as an overall drop in all of the NeNa cycle isotopes. The large enhancement in ^{23}Na comes about initially through the destruction of ^{22}Ne. The ^{22}Ne$(p,\gamma)^{23}$Na reaction proceeds quickly enough so that its uncertainties have little effect on the ^{23}Na abundance at the time of 5% hydrogen depletion. The increase in the

^{23}Na abundance is more than the loss from ^{21}Ne and ^{22}Ne, with ^{20}Ne remaining roughly constant, while the increase in the ^{14}N abundance is less than the total loss from the ^{12}C and ^{16}O abundances. This seems suggestive of leakage from the CNO cycle into the NeNa cycle, eventually feeding the ^{23}Na increase.

The effect of the new reaction rates on the sodium and oxygen abundances is shown in Figure 7.11. The vertical line again indicates the 5% depletion of hydrogen from its initial value. The effects of the ^{22}Ne$(p,\gamma)^{23}$Na reaction rate uncertainties are seen to occur mostly before the primary decrease in oxygen content. Decreasing oxygen abundances occur with increasing sodium abundances almost regardless of the existence of the two possible resonances at 8862 and 8894 keV in ^{23}Na, because the rate of burning ^{22}Ne into ^{23}Na is relatively rapid compared to the reactions that destroy sodium. The production of sodium is seen to precede the destruction of oxygen, which is consistent with the observational results shown in Figure 1.2.

Observations of the sum of the CNO abundances could verify that there is a physical link between the oxygen that is depleted and the sodium that is created. At present there is not clear observational evidence for or against this proposition, with some observations supporting a constant C+N+O value and others with star to star variations (see [Sne92] and references therein). The formation of molecules containing carbon, nitrogen, and oxygen at low temperatures makes the precise determination of the individual abundances difficult. To find the source of the sodium enhancement, it would also be useful to determine the abundance of neon. Unfortunately, this is complicated by the lack of neon spectral lines in the optical region [Car96].

The qualitative results of the network calculations indicate the need to combine the new reaction rates with a more realistic simulation. This would couple the nucleosynthesis network to the hydrodynamics of the stellar environment, and thus more fully explore the effects of the different rates.

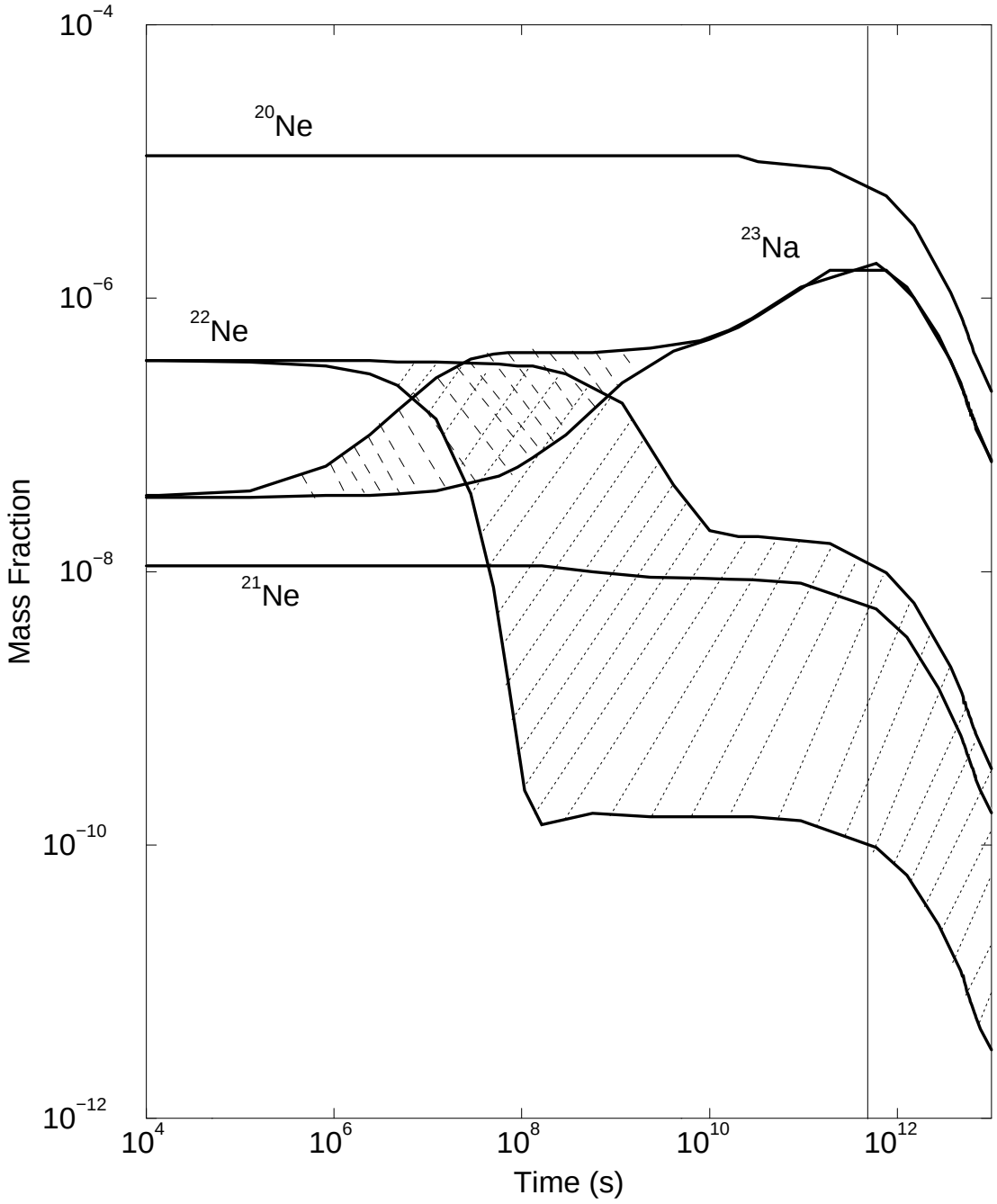

Figure 7.10: Time evolution of mass fractions for stable neon and sodium isotopes for $T_9 = 0.045$ and $\rho = 100$ gm/cm^3. Hatched areas indicate the range of values allowed by the current upper and lower limits on the $^{22}\mathrm{Ne}(p,\gamma)^{23}\mathrm{Na}$ reaction rate. The vertical bar indicates the point at which hydrogen is depleted by 5% from its initial value. The slight kinks in the sodium abundance around 5×10^{11} seconds are artifacts of the steps set by the code for output.

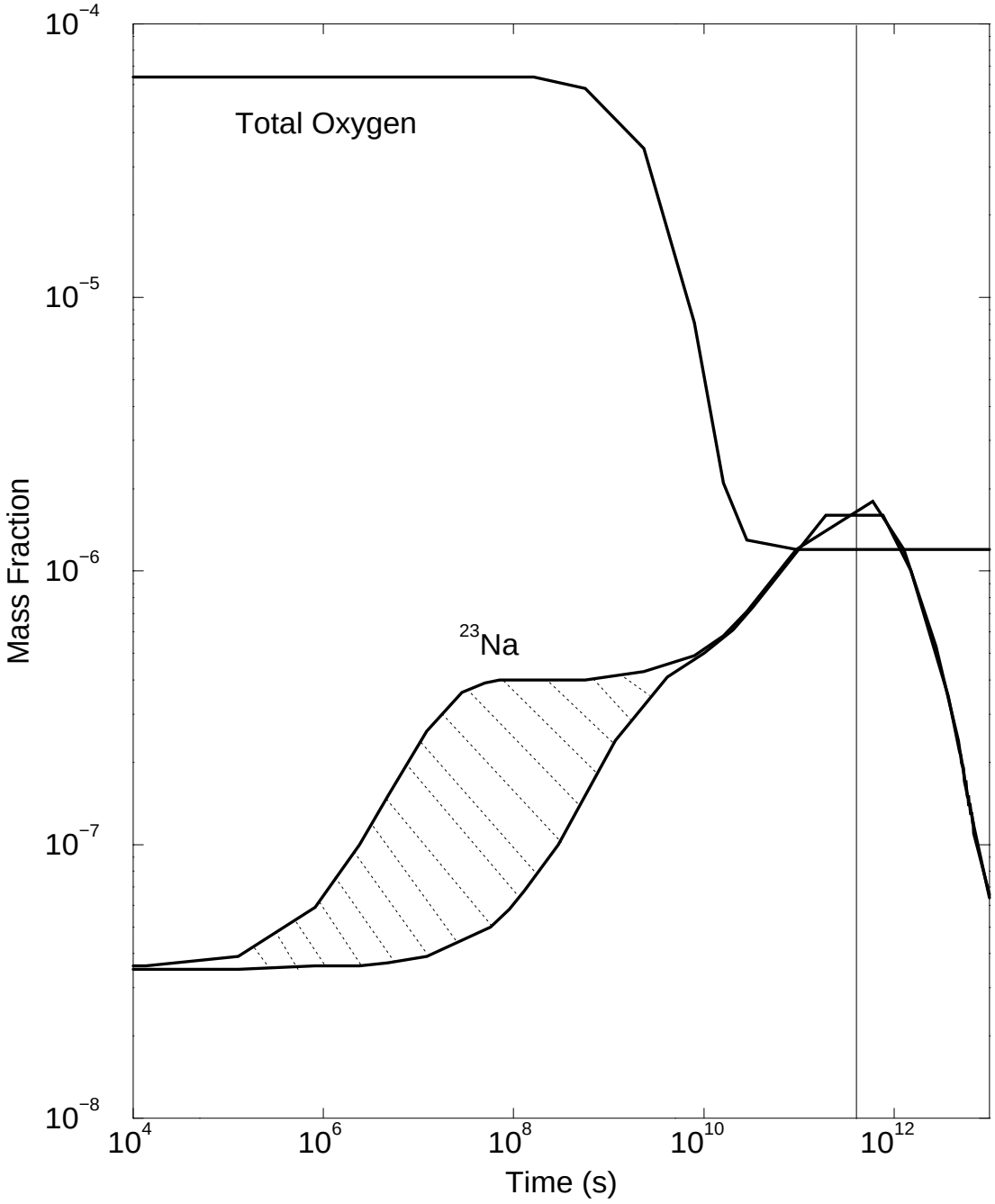

Figure 7.11: Evolution of sodium and oxygen mass fractions using the new reaction rates and the same physical situation as described in Figure 7.10. The hatched area indicates the effects of the current uncertainty in the $^{22}\mathrm{Ne}(p,\gamma)^{23}\mathrm{Na}$ reaction rate. The vertical line indicates the point at which hydrogen is depleted by 5% from its initial value. The slight kinks in the sodium abundance around 5×10^{11} seconds are artifacts of the steps set by the code for output.

7.3 Conclusions

The proton-stripping reaction (^{3}He, d) on ^{22}Ne and ^{23}Na to states of astrophysical interest has been measured. From the comparison of the measured angular distributions to DWBA predictions, reliable spectroscopic factors have been determined for a range of l-values, and single-particle proton widths have been simultaneously calculated.

The uncertainties in the ^{22}Ne$(p,\gamma)^{23}$Na reaction rate have been lowered compared to the previous work. The influence of the two possible low-energy resonances has been reduced, though not eliminated completely. Their tentative existence is still the primary contributor to the uncertainty in the reaction rate. However, the results of the network calculations illustrate that this uncertainty has little bearing on the anti-correlation of sodium and oxygen. The anti-correlation seen in Figure 7.11 between t = 1×10^9 seconds and 5×10^{11} seconds shows that the observational results can be matched if mixing beyond the standard stellar model occurs to a temperature depth on the order of $T_9 = 0.045$.

In addition, our results for the ^{23}Na$(p,\gamma)^{24}$Mg reaction rate imply that it may be significantly higher than the previous rate in the upper regions of the temperature range of interest for red giants. The uncertainty from the resonance at $E_{cm} = 138$ keV results from the unknown J^π value. If this were determined, the l-transfer could be limited and a more accurate Γ_p could be extracted from the present data. Using the current upper limit, we predict loss of material from the NeNa cycle at lower temperatures than thought previously. Direct (p,γ) measurements of this resonance may also be possible, and they would provide either a value for $\omega\gamma$ or a more stringent limit.

REFERENCES

[Ash98] K. M. Ashman and S. E. Zepf, *Globular Cluster Systems*, Cambridge University Press, Cambridge, 1998.

[Aud95] G. Audi and A. H. Wapstra, Nuclear Physics **A595**, 409 (1995).

[Bac76] B. B. Back, R. R. Betts, C. Gaarde, and H. Oeschler, Physical Review **C 13**, 875 (1976).

[Bak89] E. L. Bakkum and C. Van der Leun, Nuclear Physics **A500**, 1 (1989).

[Bar89] R. J. Barlow, *Statistics: A Guide to the Use of Statistical Methods in the Physical Sciences*, John Wiley & Sons, Chichester, England, 1989.

[Bas66] R. H. Bassel, Physical Review **149**, 791 (1966).

[Bec71] F. D. Becchetti and G. W. Greenlees, "A General Set of ^{3}He and Triton Optical-Model Potentials for A>40, E<40 MeV", in *Polarization Phenomena in Nuclear Reactions*, page 682, University of Wisconsin Press, Madison, WI, 1971.

[Ber98] P. F. Bertone, 1998, private communication.

[Bev92] P. R. Bevington and D. K. Robinson, *Data Reduction and Error Analysis for the Physical Sciences*, McGraw-Hill Inc., New York, NY, 1992.

[Bra72] D. Branford, M. J. Spooner, and I. F. Wright, Particles and Nuclei **4**, 231 (1972).

[Car96] B. W. Carney, Publications of the Astronomical Society of the Pacific **108**, 900 (1996).

[Cas80] V. Castellani, in *Globular Clusters*, edited by D. Hanes and B. Madore, page 65, Cambridge, 1980, Cambridge University Press.

[Cau88] G. R. Caughlan and W. A. Fowler, Atomic Data and Nuclear Data Tables **40**, 283 (1988).

[Cav98] R. M. Cavallo, A. V. Sweigart, and R. A. Bell, Astrophysical Journal **492**, 575 (1998).

[Cha86] A. E. Champagne, M. L. Pitt, P. H. Zhang, J. L. L. Lee, and M. J. Levine, Nuclear Physics **A459**, 239 (1986).

[Cha89] A. E. Champagne, A. J. Howard, M. S. Smith, P. V. Magnus, and P. D. Parker, Nuclear Physics **A505**, 384 (1989).

[Cha97] A. E. Champagne, 1997, private communication.

[Cha98] A. E. Champagne, 1998, private communication.

[Cha99] A. E. Champagne, 1999, private communication.

[Chi73] W. A. Childs, R. C. Ritter, B. D. Murphy, and R. M. Strang, Nuclear Physics **A203**, 133 (1973).

[Cla83] D. D. Clayton, *Principles of Stellar Evolution and Nucleosynthesis*, University of Chicago Press, Chicago, 1983.

[Cow98] G. Cowan, *Statistical Data Analysis*, Clarendon Press, Oxford, 1998.

[Dae80] W. W. Daehnick, J. D. Childs, and Z. Vrcelj, Physical Review **C 21**, 2253 (1980).

[Den90] P. A. Denisenkov and S. N. Denisenkova, Soviet Astronomy Letters **16**, 275 (1990).

[Dur93] P. R. Durrell and W. E. Harris, Astronomical Journal **105**, 1420 (1993).

[EEC95] M. F. E. Eid and A. E. Champagne, Astrophysical Journal **451**, 298 (1995).

[End77] P. M. Endt, Atomic Data and Nuclear Data Tables **19**, 23 (1977).

[End90a] P. M. Endt, Nuclear Physics **A521**, 1 (1990).

[End90b] P. M. Endt, C. Alderliesten, F. Zijderhand, A. A. Wolters, and A. G. M. V. Hess, Nuclear Physics **A510**, 209 (1990).

[Fif78] L. K. Fifield, M. J. Hurst, T. J. M. Symons, F. Watt, C. H. Zimmerman, and K. W. Allen, Nuclear Physics **A309**, 77 (1978).

[Fif90] L. K. Fifield and N. A. Orr, Nuclear Instruments & Methods **A 288**, 360 (1990).

[For95] H. T. Fortune, J. R. Powers, and L. Bargeron, Physical Review **C 51**, 1154 (1995).

[Gar78] J. D. Garrett, H. T. Fortune, R. Middleton, and W. Scholz, Physical Review **C 18**, 2032 (1978).

[Gle75] N. K. Glendenning, "One- And Two-Nucleon Transfer Reactions", in *Nuclear Spectroscopy and Reactions*, volume D, page 319, Academic Press, New York, 1975.

[Gle83] N. K. Glendenning, *Direct Nuclear Reactions*, Academic Press, New York, 1983.

[Gör82] J. Görres, C. Rolfs, P. Schmalbrock, H. P. Trautvetter, and J. Keinonen, Nuclear Physics **A385**, 57 (1982).

[Gör83] J. Görres, H. W. Becker, L. Buchmann, C. Rolfs, P. Schmalbrock, H. P. Trautvetter, A. Vlieks, J. W. Hammer, and T. R. Donoghue, Nuclear Physics **A408**, 372 (1983).

[Gör89] J. Görres, M. Wiescher, and C. Rolfs, Astrophysical Journal **343**, 365 (1989).

[Gra95] G. Graw, 1995, private communication.

[Gre75] P. W. Green, G. D. Jones, D. T. Kelly, J. A. Kuehner, and D. T. Petty, Physical Review **C 12**, 887 (1975).

[Han99] M. D. Hannam and W. J. Thompson, to be published in Nuclear Instruments & Methods **A** (1999).

[Ibe80] I. Iben, in *Globular Clusters*, edited by D. Hanes and B. Madore, page 125, Cambridge, 1980, Cambridge University Press.

[Ibe84] I. Iben and A. Renzini, Physics Reports **105**, 329 (1984).

[Ili94] C. Iliadis, J. Görres, J. G. Ross, K. W. Scheller, M. Wiescher, R. E. Azuma, G. Roters, H. P. Trautvetter, and H. C. Evans, Nuclear Physics **A571**, 132 (1994).

[Ili96] C. Iliadis, L. Buchmann, P. M. Endt, H. Herndl, and M. Wiescher, Physical Review C **53**, 475 (1996).

[Ili97] C. Iliadis, Nuclear Physics **A618**, 166 (1997).

[Ili99] C. Iliadis, P. M. Endt, N. Prantzos, and W. J. Thompson, Astrophysics Journal, in print (1999).

[KeK77] G. J. KeKelis, A. H. Lumpkin, K. W. Kemper, and J. D. Fox, Physical Review **C 15**, 664 (1977).

[Key68] G. A. Keyworth, P. Wilhjelm, G. C. Kyker, Jr., H. W. Newson, and E. G. Bilpuch, Physical Review **176**, 1302 (1968).

[Kra71] E. Kramer, G. Mairle, and G. Kaschl, Nuclear Physics **A165**, 353 (1971).

[Kra93] R. P. Kraft, C. Sneden, G. E. Langer, and M. D. Shetrone, Astronomical Journal **106**, 1490 (1993).

[Kra98] R. P. Kraft, C. Sneden, G. H. Smith, M. D. Shetrone, and J. Fulbright, Astronomical Journal **115**, 1500 (1998).

[Kun] Program DWUCK4, P.D. Kunz (unpublished); extended version of J.R. Comfort (unpublished).

[Lan93] G. E. Langer, R. Hoffman, and C. Sneden, Publications of the Astronomical Society of the Pacific **105**, 301 (1993).

[Mac75] M. H. Macfarlane and J. P. Schiffer, "Transfer Reactions", in *Nuclear Spectroscopy and Reactions*, volume D, page 169, Academic Press, New York, 1975.

[Mar57] J. B. Marion and W. A. Fowler, Astrophysical Journal **125**, 221 (1957).

[Mar75] R. G. Markham and R. G. H. Robertson, Nuclear Instruments & Methods **129**, 131 (1975).

[Mey73] M. A. Meyer and J. J. A. Smit, Nuclear Physics **A205**, 177 (1973).

[Mos76] C. E. Moss, Nuclear Physics **A269**, 429 (1976).

[Muk92] K. Mukherjee et al., Publications of the Astronomical Society of the Pacific **104**, 561 (1992).

[Nan92] H. Nann, Nuclear Physics **A376**, 61 (1992).

[Nor80] J. Norris, in *Globular Clusters*, edited by D. Hanes and B. Madore, page 113, Cambridge, 1980, Cambridge University Press.

[Par92] Physical Review **D 45**, III.32 (1992), Particle Data Group.

[Per76] C. M. Perey and F. G. Perey, Atomic Data and Nuclear Data Tables **17**, 1 (1976).

[Pow71] J. R. Powers, H. T. Fortune, R. Middleton, and O. Hansen, Physical Review **C 4**, 2030 (1971).

[Pra87] N. Prantzos, M. Arnould, and J. P. Arcoragi, Astrophysical Journal **315**, 209 (1987).

[Rol73] C. Rolfs, Nuclear Physics **A217**, 29 (1973).

[Rol75] C. Rolfs, W. S. Rodney, M. H. Shapiro, and H. Winkler, Nuclear Physics **A241**, 460 (1975).

[Rol88] C. Rolfs and W. S. Rodney, *Cauldrons in the Cosmos*, University of Chicago Press, Chicago, 1988.

[Sal93] M. Salaris, A. Chieffi, and O. Straniero, Astrophysical Journal **414**, 580 (1993).

[Sat64] G. R. Satchler, Nuclear Physics **55**, 1 (1964).

[Sat83] G. R. Satchler, *Direct Nuclear Reactions*, Oxford University Press, Oxford, 1983.

[Sch63] J. P. Schiffer, Nuclear Physics **46**, 246 (1963).

[Sch83] P. Schmalbrock, H. W. Becker, L. Buchmann, J. Görres, K. U. Kettner, W. E. Kieser, H. Kräwinkel, C. Rolfs, H. P. Trautvetter, J. W. Hammer, and R. E. Azuma, Nuclear Physics **A398**, 279 (1983).

[Smi90] M. S. Smith, *Onset & Breakout of Stellar HCNO Cycle*, Ph.D. thesis, Yale University, 1990.

[Sne92] C. Sneden, R. P. Kraft, C. F. Prosser, and G. E. Langer, Astronomical Journal **104**, 2121 (1992).

[Spe67] J. E. Spencer and H. A. Enge, Nuclear Instruments & Methods **49**, 181 (1967).

[Ste93] P. B. Stetson, in *The Globular Cluster-Galaxy Connection, APS Conference Series, Vol. 48*, edited by G. H. Smith and J. P. Brodie, page 14, San Francisco, 1993.

[Sun93] N. Suntzeff, in *The Globular Cluster-Galaxy Connection, APS Conference Series, Vol. 48*, edited by G. H. Smith and J. P. Brodie, page 167, San Francisco, 1993.

[Swe79] A. V. Sweigart and J. G. Mengel, Astrophysical Journal **229**, 624 (1979).

[Tho99] W. J. Thompson and C. Iliadis, Nuclear Physics A, in print (1999).

[Uhr85] M. Uhrmacher, Nuclear Instruments & Methods **B 9**, 234 (1985).

[Van87] J. R. Vanhoy, E. G. Bilpuch, C. R. Westerfeldt, and G. E. Mitchell, Physical Review C **36**, 920 (1987).

[Ver88] W. J. Vermeer, D. M. Pringle, and I. F. Wright, Nuclear Physics **A485**, 380 (1988).

[Vin70] C. M. Vincent and H. T. Fortune, Physical Review C **2**, 782 (1970).

[Vin73] C. M. Vincent and H. T. Fortune, Physical Review C **7**, 865 (1973).

[Wag69] R. V. Wagoner, Astrophysical Journal **162**, 247 (1969).

[Wal97] G. Wallerstein et al., Reviews of Modern Physics **69**, 995 (1997).

[Wie97] M. Wiescher, 1997, private communication.

[Zie92] J. F. Ziegler, 1992, program TRIM, unpublished.

[Zys81] J. Zyskind, M. Rios, and C. Rolfs, Astrophysical Journal **243**, L53 (1981).